UNIVERSITY OF CALIFORNIA

Los Angeles

Spectroscopic Studies of Mixed Valence Compounds and Confined Fluorophores

A dissertation submitted in partial satisfaction of the requirements

for the degree Doctor of Philosophy in Chemistry

by

Yen-Ting Chen

2014

ABSTRACT OF THE DISSERTATION

Spectroscopic Studies of Mixed Valence Compounds and Confined Fluorophores

by

Yen-Ting Chen

Doctor of Philosophy in Chemistry

University of California, Los Angeles, 2014

Professor Jeffrey I. Zink, Chair

The work presented in this dissertation encompasses spectroscopic research in two different areas. The first part involves spectroscopic studies of mixed valence systems. Mixed valence compounds have two or more equivalent charge bearing sites that are coupled, and can occur in both the ground and excited state. An intervalence charge transfer band can be observed for the former, while the latter can have two transitions whose intensities depend on selection rules.

The first chapter in this dissertation presents an introduction to the fundamental concepts of mixed valence, and the spectroscopic and theoretical methods that can be utilized to study mixed valence systems. The following chapter analyzes the excited state mixed valence of cis and trans di-(4-acetylpyridine)-tetraamineruthenium complexes using absorption and resonance Raman spectroscopies, the time-dependent theory of spectroscopy, and neighboring orbital models. The intricacy of the importance of dipole orientation averaging is also discussed. The next chapter presents an expansion of the three state model used for transition dipole moment analysis that has been previously used. The expanded model is discussed for both the ruthenium complex and a diisopropyl ditolylhydrazine compound. Chapter four investigates another mixed valence system, a cyclophane diradical dication compound that has ground state mixed valence. This system has an unusual form of coupling, mediated through π-π interaction between two stacking phenyl rings.

The second part of this dissertation and the last chapter investigate the physical characteristics of a fluorophore confined in the pores of azobenzene-functionalized mesoporous silica nanoparticles. Two spectroscopic methods are utilized: time-resolved fluorescence anisotropy and rigidochromic studies. These studies help elucidate the microenvironment inside of the mesopores.

The dissertation of Yen-Ting Chen is approved.

Peter M. Felker

Michael A. Jura

Jeffrey I. Zink, Committee Chair

University of California, Los Angeles

2014

This dissertation is dedicated to my loving parents, Ching-San Chen and Cindy Wei, my dear brother Eric Chen, and my husband Ben-Yue Chang.

TABLE OF CONTENTS

ACKNOWLEDGEMENTS

First and foremost, I would like to acknowledge and thank my advisor, Dr. Jeffrey I. Zink, for giving me the opportunity to join his research group and being a great mentor. During my years in this group, I have learnt many things from Dr. Zink. Not only have I gained knowledge in our field of molecular spectroscopy, I have also learned from him skills in experimental design, writing scientific findings, proposing new ideas and writing proposals and much more. My five years here has been a great learning experience as a scientist. I would also like to thank my committee members, Professors Peter M. Felker, Yves F. Rubin and Michael A. Jura for their time and advice. Additionally, I would like to thank Professor Stephen F. Nelsen and his students for the collaboration and providing the interesting molecule for the cyclophane study, and Dr. Edward Plummer for synthesizing the compounds and preliminary studies for the Ru complex research.

Second are my mentors in the Zink group: Dr. Matthew Kiesz in particular, who taught me the basics of spectroscopy and working in the laser lab. We have had many an interesting discussion about our research, and I would not be where I am today if not for his guidance. He has also been the big brother to me in lab, sometimes being mean but always there to support me. Thanks also to Dr. Ryan Hoekstra and Dr. Bryana Henderson, who, as senior members in our spectroscopy group, were also there to provide me with guidance. I would also like to thank Dr. Min Xue, who was always patient for discussing and answering my questions, even after he graduated.

I am also grateful for my other fellow labmates, especially Juyao Dong and Angela Hwang. As fellow graduate students in the same year, we have shared many ups and downs together in our time as a grad student. I am also grateful for the companionship of all the past and present Zink

lab members, including Dr. Yuen Lau, Dr. Courtney Thomas, Dr. Travis Pecorelli, Dr. Daniel Ferris, Dr. Sanaz Gardner, Dr. Marcelle Dibrell, Dr. Zongxi Li, Dr. Derrick Tarn, Dr. Tania Guardardo, Dr. Melissa Russell, Dr. Eunshil Choi, Dr. Philippe Saint-Cricq Riviere, Dr. Bastian Ruehle, Dr. Wen-Yen Huang, Zilu Li, Chia-Jung Yu, Lingyu Zhang, Daniel Pazo, and Ruining Wang. The friendships of all of these fellow labmates have made our group a warm and friendly place to be, and I would like to thank them all.

Last but not least, I would like to thank all of my friends who have provided friendship, comfort, advice and happy times in general, to help me through the tough times of a graduate student. Most important of all, I would like to thank my mother and father, Cindy Wei and Ching-San Chen, for providing for me, caring for me, loving me unconditionally, and making me the person I am today, and my little brother Eric Chen, whose love for me has made me strive to be a better person. And to my husband, Ben-Yue Chang, for always being there for me, with patience and love and always a warm and supporting hug. Thank you all.

VITA

2009	B.S. Chemistry National Taiwan University, Taiwan
2009-2014	Teaching Assistant Department of Chemistry and Biochemistry University of California, Los Angeles Los Angeles, California
2010-2014	Research Assistant Department of Chemistry and Biochemistry University of California, Los Angeles Los Angeles, California

PUBLICATIONS

1. Hoekstra, Ryan M.; Chen, Yen-Ting; Kiesz, Matthew D.; Telo, João P.; Stephenson, Rachel M.; Nelsen, Stephen F.; Zink, Jeffrey I., Resonance Raman Spectroscopic Study of Solvent-Dependent Coexistence of Localized and Delocalized Dinitroaromatic Radical Anions. *Canadian Journal of Chemistry* **2014**, *92*, 940-947
2. Kiesz, Matthew D.; Hoekstra, Ryan M.; Chen, Yen-Ting; Telo, João P.; Nelsen, Stephen F.; Zink, Jeffrey I., Coupled States in Dinitrofluorene: Relationships between Ground State and Excited State Mixed Valence. *Journal of Physical Chemistry, A* **2014**, *Just Accepted*

Chapter 1

Fundamentals of Excited State Mixed Valence

1.1 INTRODUCTION

Compounds that exhibit mixed valence contain elements or moieties that can exist in more than one oxidation state.[1,2] These can be a variety of compounds, including metal-ligand organometallic complexes or organic molecules.[3,4] One of the best known compounds is the Creutz-Taube complex,[5] where there are two equivalent ruthenium metal centers with +2 or +3 oxidation states. Charge transfer can occur between these charge bearing units (CBU) when there is electronic communication, and this results in mixed valence. A typical mixed valence compound can be represented by M^+-B-M and M-B-M^+, where the M's are the charge bearing sites, and B is the connecting bridge. As this mixed valence occurs in the ground state, such a system is defined to have ground state mixed valence (GSMV). M^+-B-M and M-B-M^+ are representations in the diabatic basis, and their potential energy curves are shown as solid lines in Figure 1-1a. These potential curves couple to form the adiabatic potential curves, shown as dotted lines, and the degree of coupling determines the energy splitting between the two adiabats. A single electronic transition can occur, and is the intervalence charge transfer band observed in GSMV absorption spectra.

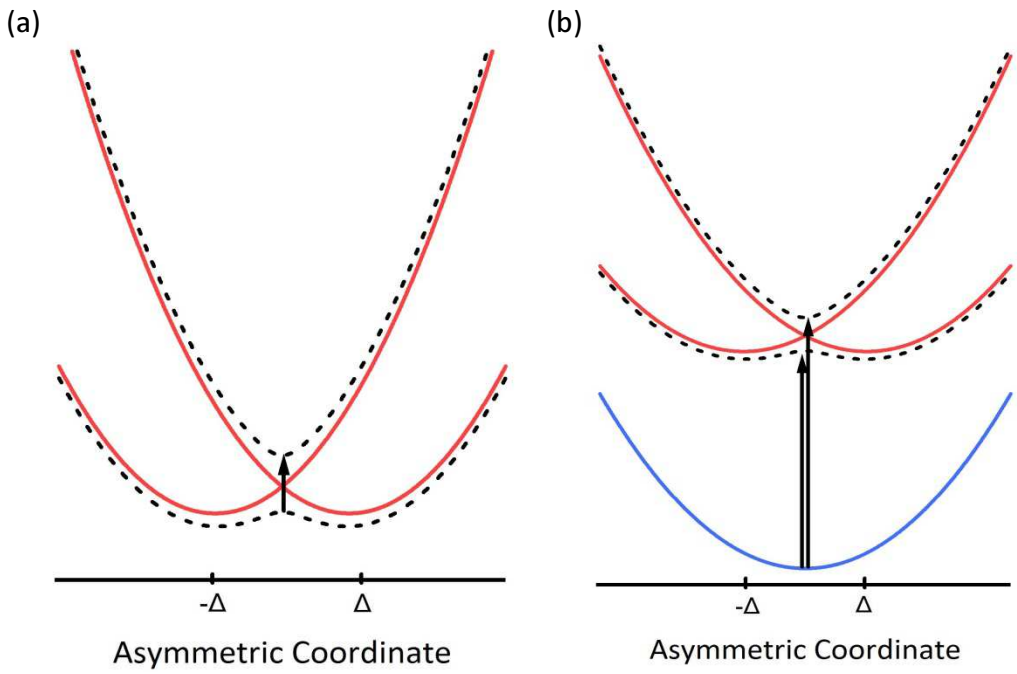

Figure 1-1. Diabatic (solid lines) and adiabatic (dashed lines) potentials for (a) ground state mixed valence and (b) excited state mixed valence. Electronic transitions are shown with single arrow.

This same phenomenon can occur in the excited state, where the ground state has a symmetric distribution of charge, and when excited, the charge is transferred to either CBU. Such a system is defined to have excited state mixed valence (ESMV).[6-9] An example would be M-B^+-M in the ground state, and M^+-B-M and M-B-M^+ in the excited state, and the respective diabats and the coupled adiabats are shown in Figure 1-1b. The greatest difference between ESMV and GSMV is that with ESMV, two electronic transitions are possible, from the ground state to either adiabat. The energy splitting of the excited state adiabats again depends on the magnitude of coupling, but in contrast to GSMV, the sign of the coupling also plays an important role. The sign of the coupling, along with the transition dipole moments, determines which of the transitions is allowed and which is forbidden, and will be further discussed in detail in a later section.

1.2 ADIABATIC TRANSFORMATION

Before discussing how each parameter of coupling will affect the mixed valence, we must first introduce the matrix representations of the coupling process. For an ESMV system, the energies of the orbitals involved can be represented in a matrix by the potential energy operators V_G, V_L and V_R, the ground state, and two diabatic, localized excited states respectively:

$$V = \begin{pmatrix} V_G & 0 & 0 \\ 0 & V_L & H_{ab} \\ 0 & H_{ab} & V_R \end{pmatrix} \tag{1}$$

The most important element for mixed valence in this matrix is the off-diagonal element H_{ab}. This is the coupling term that effectively mixes the two interacting potentials. This matrix represents the diabatic basis, and can be transformed to the adiabatic basis with the unitary transformation matrix

$$U^{-1} = \begin{pmatrix} 1 & 0 & 0 \\ 0 & \cos\theta & \sin\theta \\ 0 & -\sin\theta & \cos\theta \end{pmatrix} \tag{2}$$

where

$$\tan 2\theta = \frac{2H_{ab}}{V_1(Q) - V_2(Q)} \tag{3}$$

Similarly, the wave functions that are propagated on these potentials in the time-dependent theory of spectroscopy[10,11] must also be transformed to the adiabatic basis forming an in-phase $\psi^+ = \psi_L \cos\theta + \psi_R \sin\theta$ and out-of-phase $\psi^- = \psi_R \cos\theta - \psi_L \sin\theta$ wave function. The energy ordering of these adiabatic wave functions and which adiabatic potential they correspond to depend on the sign of the coupling element H_{ab}.

1.3 EXCITED STATE MIXED VALENCE PARAMETERS

There are several aspects of the coupling that will affect the outcome of mixed valence. In this section, we will discuss how the sign of the coupling, the magnitude of coupling, the distortion and frequency of the excited state potentials, and the transition dipole moments all play a role in determining the overall absorption spectrum of an ESMV system.

1.3.1 Sign of Coupling

As earlier mentioned, the sign of the coupling is one of the important differences between ESMV and GSMV. For the simplest case of electronic communication, bonding between two atoms, there is through-space direct overlap of their orbitals and the in-phase combination (bonding) is always stabilized and lower in energy than the out-of-phase combination (antibonding). The coupling is inherently negative. However, when the coupling is mediated through bonds via a bridge, the sign of the coupling depends on the interaction of the CBU orbitals with the bridge orbitals, and could be either positive or negative.[12,13] For positive coupling, the out-of-phase combination will instead be lower in energy.

This phenomenon can occur in both the ground and excited states, but for GSMV, as there is only a single possible electronic transition, the identity of the lower and upper adiabat is not important. However, for ESMV, depending also on the transition dipole moments, different selection rules will arise for each adiabatic wave function, and their energy ordering will determine if a lower or higher energy band is the allowed and most intense band in absorption spectra.

1.3.2 Magnitude of Coupling

The magnitude of coupling reflects how strong the electronic communication is between the two CBUs; the stronger the interaction, the larger the magnitude of coupling. Mixed valence compounds can be categorized into three groups according to the degree of coupling, with the Robin-Day classification.[14] Class I compounds are compounds that have virtually no electronic communication, and the charge is localized on one site or the other. The diabats essentially remain the same, with little to no coupling. Class III compounds are the other extreme where there is strong electronic interaction and the charge is completely delocalized across the sites. For these compounds, the diabats couple to form adiabats that both have single energy minima. The resulting energy splitting between the lower and upper adiabats is equal to twice the magnitude of coupling, $2H_{ab}$, and is large. This can be observed in ESMV electronic spectra with a large separation between the two absorption bands. Class II compounds are intermediate in their degree of coupling. There is some localization of charge, but the energy to convert between the two sites is low and the charge readily moves between the sites. This can be understood from the lower energy adiabat which forms a double well potential, while the upper potential remains a single energy minimum potential.[15]

Potential energy curves for each of the three classes are shown in Figure 1-2 to demonstrate the effect of the magnitude of coupling. Their corresponding two absorption bands are also shown, with the energy splitting between the two bands increasing with magnitude of coupling.

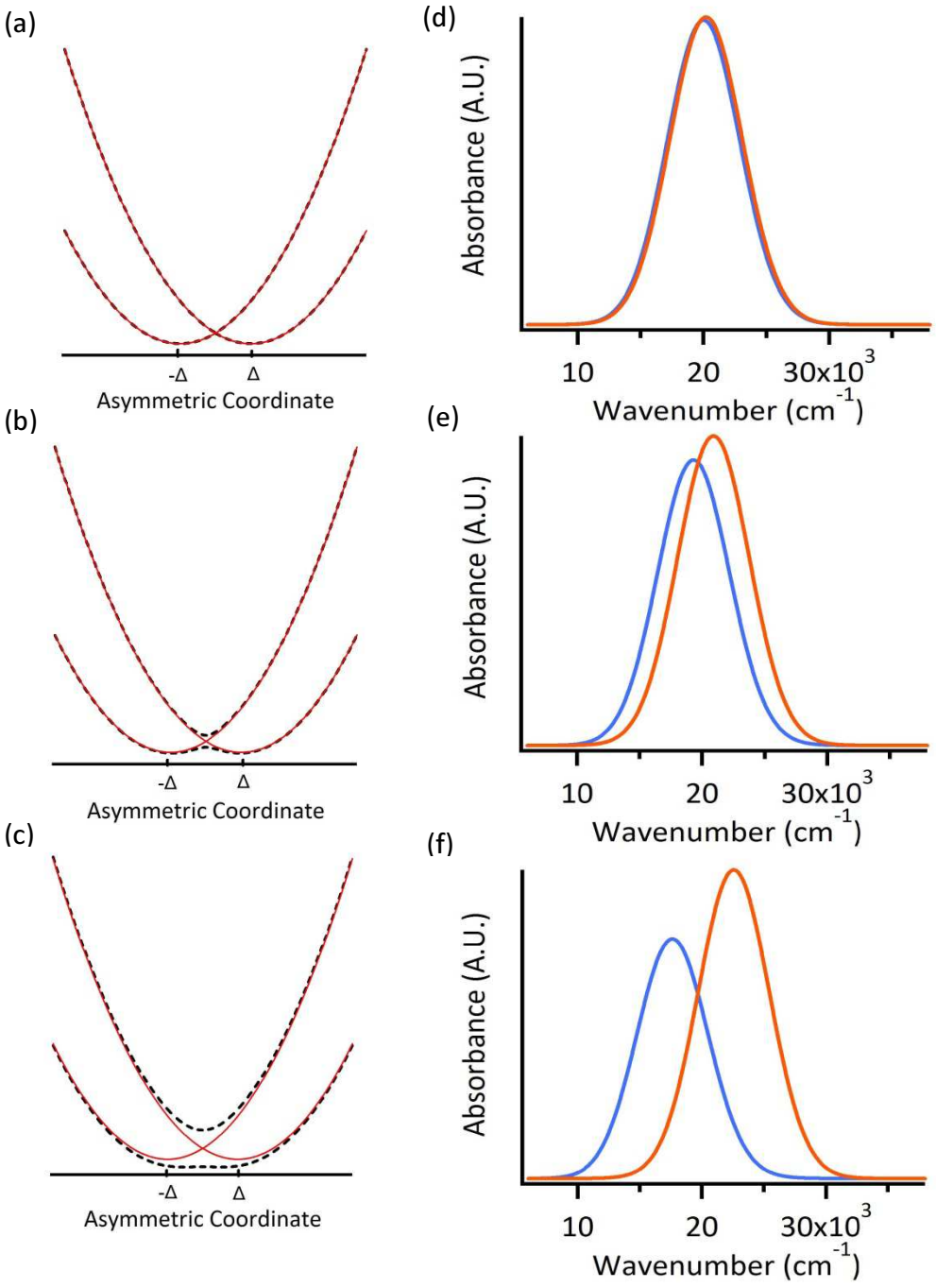

Figure 1-2. Left panel: Diabatic (red solid lines) and adiabatic (black dashed lines) potentials of the coupled excited state for (a) Class I (b) Class II and (c) Class III systems. Right panel: Absorption bands demonstrating the energy splitting with different coupling. Blue and orange bands depict individual absorption bands to each ESMV adiabatic state. Each absorption spectrum corresponds to (d) Class I (e) Class II and (f) Class III systems. Energy splitting between the two bands increase with increasing coupling.

1.3.3 Distortion

Along the asymmetric coordinate Q, the charge localized diabats are displaced relative to the ground state potential by a displacement of Δ in either direction. From a time-dependent theory perspective, the more the excited wave packet is displaced from its initial position, the more vibronic recurrences occur and the corresponding absorption spectrum is broadened and will also appear more shifted towards higher energy. Figure 1-3 demonstrates the difference in absorption spectra with different distortion values.

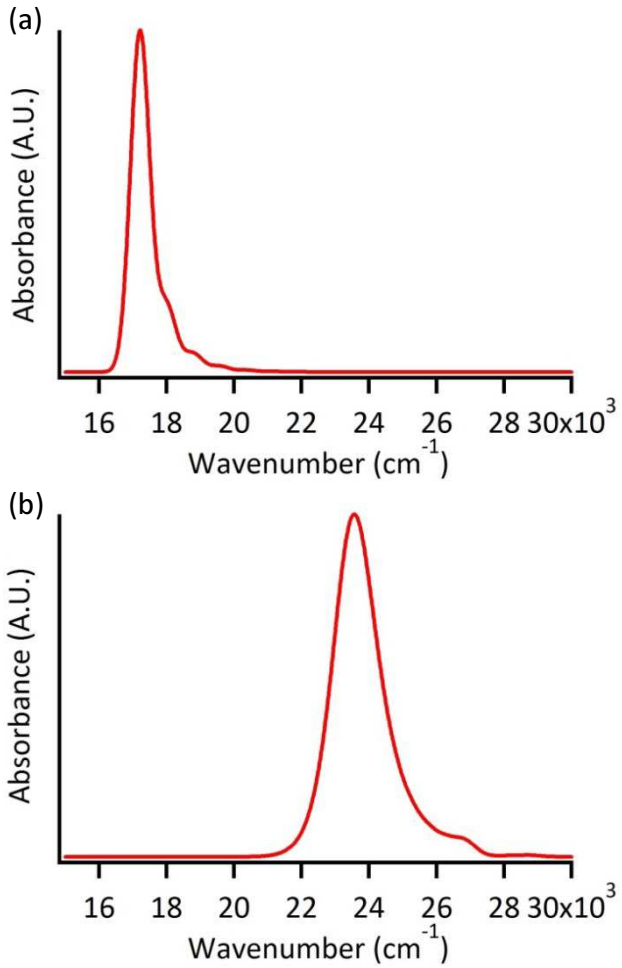

Figure 1-3. Comparison of absorption spectra for different displacements of excited state potentials. For both spectra, only the lower energy ESMV transition is shown. (a) Small distortion values: narrower absorption band. (b) Larger distortion values: broadened absorption band shifted to higher energy.

1.3.4 Frequency

The frequency of the normal modes involved is represented by the curvature of the parabolic potential energy curves. A large frequency forms a much narrower potential curve with large vibrational spacings, and this is reflected in the absorption spectra. For absorption spectra with low damping where vibronic structure is observable, the spacings between each vibronic peak are larger for larger frequency modes; for large damping, this effectively broadens the entire band. These effects are shown in Figure 1-4 with different frequency values.

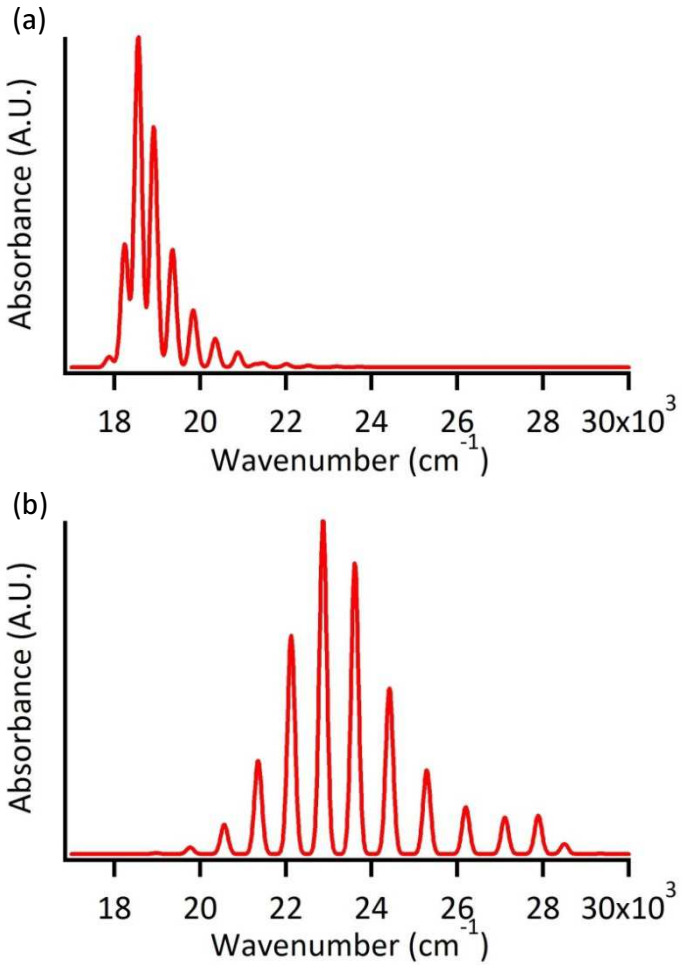

Figure 1-4. Comparison of absorption spectra (at low damping) for different frequencies. (a) Lower frequency at 400 cm^{-1} (b) Higher frequency at 800 cm^{-1}. Spacing between vibronic structure becomes larger with higher frequency.

1.3.5 Transition Dipole Moment

Electric dipole operators essentially promote the ground state wave function to the final excited state surface. The square of the transition dipole moment determines the intensity of the absorption bands. In excited state mixed valence, two transition dipole moments must be considered, one to each CBU, and as there is electronic communication present, we must also consider how these two dipole moments couple. The resulting adiabatic transition dipole moments will help determine the selection rules to each ESMV state.[16]

The matrix representation of the diabatic transition dipole moments can be written as

$$\mu_{diabat} = \begin{pmatrix} 0 & \pm\mu_1 & \mu_2 \\ \pm\mu_1 & 0 & 0 \\ \mu_2 & 0 & 0 \end{pmatrix} \tag{4}$$

The signs indicate the relative orientation between the two transition dipoles. The positive sign applies when CBUs are positioned on the same side and there is 0^o separation between the dipoles (parallel), while the negative sign applies for a separation of 180^o (antiparallel). After adiabatic transformation, the transition dipole matrix is

$$\mu_{adiabat} = \begin{pmatrix} 0 & \pm\mu_1 \cos\theta + \mu_2 \sin\theta & \mp\mu_1 \sin\theta + \mu_2 \cos\theta \\ \pm\mu_1 \cos\theta + \mu_2 \sin\theta & 0 & 0 \\ \mp\mu_1 \sin\theta + \mu_2 \cos\theta & 0 & 0 \end{pmatrix} \tag{5}$$

The detailed explanations for the values of these adiabatic transition dipoles are presented in Chapter 3. Here, we show a summary of the resulting selection rules of parallel and antiparallel dipole situations in Table 1-1.

	Transition to state	Dipole	Dipole value along Q	Selection rule
Parallel	Ψ^+	$\mu_1\cos\theta + \mu_2\sin\theta$	non-zero everywhere	Electric dipole allowed*
	Ψ^-	$-\mu_1\sin\theta + \mu_2\cos\theta$	zero at Q = 0 positive when Q > 0 negative when Q < 0	Dipole forbidden, but vibronically allowed
Antiparallel	Ψ^+	$-\mu_1\cos\theta + \mu_2\sin\theta$	zero at Q = 0 negative when Q > 0 positive when Q < 0	Dipole forbidden, but vibronically allowed
	Ψ^-	$\mu_1\sin\theta + \mu_2\cos\theta$	non-zero everywhere	Electric dipole allowed*

Table 1-1. Adiabatic transition dipole moments and selection rules for parallel and antiparallel dipoles.
* In the adiabatic limit where $H_{ab} \gg V_1(Q) - V_2(Q)$

For example, an ESMV system with CBUs oriented 180° apart will have antiparallel dipoles, and the electronic transition from the ground state to the out-of-phase adiabat will be dipole allowed. However, the transition to the in-phase adiabat will be dipole forbidden, but as the wave function moves along the coordinate Q away from the initial position, it will become vibronically allowed. Therefore, it will exhibit only a weak band in the absorption spectrum. Which of these corresponds to lower or higher energy is determined by the sign of the coupling as discussed earlier.

This derivation demonstrates the selection rules for the extreme cases of the transition dipole moment relative orientations being parallel and antiparallel to each other. But the orientation angle β can be any angle in between 0° and 180° for a molecule. All orientations can be

considered to be a superposition of the parallel and antiparallel components, as can be shown with a trigonometric projection in Figure 1-5.

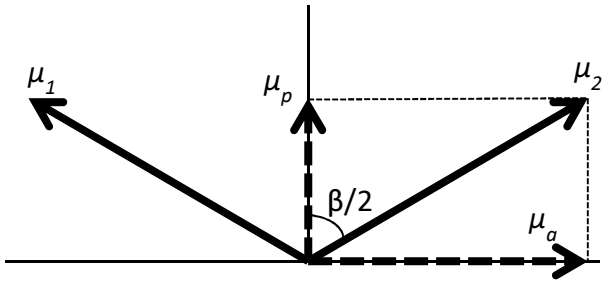

Figure 1-5. Depiction of transition dipoles μ_1 and μ_2 with vector components projected onto the orthogonal parallel and antiparallel components.

For two transition dipole moments μ_1 and μ_2, both have vector projections onto the axis bisecting them. These projections are parallel to each other and correspond to the parallel dipole component μ_p. On the other hand, their projections on the orthogonal axis are in opposite directions and correspond to the antiparallel dipole component μ_a. There exists a trigonometric relationship between these vectors, and can be written as:

$$\frac{\mu_a}{\mu_p} = \frac{\mu \sin\frac{\beta}{2}}{\mu \cos\frac{\beta}{2}} = \tan\frac{\beta}{2} \tag{6}$$

The ratio of intensities of antiparallel band to the parallel band can also be derived, since oscillator strength is proportional to the square of the transition dipole:

$$\frac{f_a}{f_p} = \frac{\mu_a^2}{\mu_p^2} = \tan^2\frac{\beta}{2} \tag{7}$$

Therefore, the total absorption spectrum of any molecule with dipole orientation at angle β can be calculated as the weighted sum of the parallel and antiparallel components according to the

relationship in Equation 7.[8] In the purely antiparallel or parallel dipole compound, the absorption spectrum will contain almost entirely of one transition band while the other dipole forbidden but vibronically allowed band will be extremely weak. Figure 1-6 demonstrates the effect on the absorption spectrum as the angle β changes.

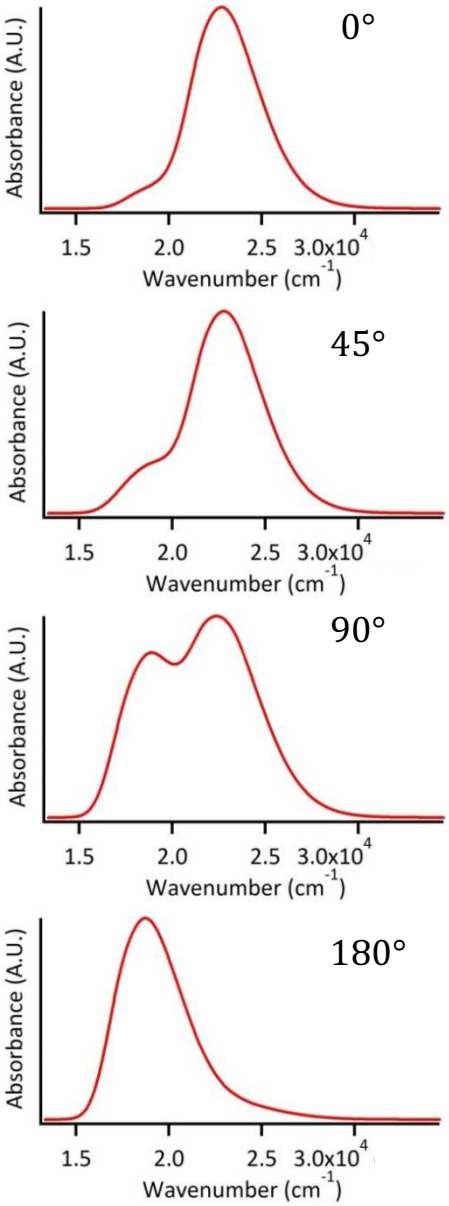

Figure 1-6. Intensity ratio change of antiparallel to parallel bands at different angles of orientation between the two transition dipole moments.

This same relationship can be derived by considering orientational averaging in the time-dependent theory of spectroscopy. The intensity of absorption is given by the equation[10]

$$I(\omega) = C\omega \int_{-\infty}^{\infty} \mathrm{e}^{\mathrm{i}\omega t} \left\{ \langle \Phi | \Phi(t) \rangle \exp\left(-\Gamma^2 t^2 + \frac{iE_{00}}{h} t \right) \right\} \mathrm{d}t \tag{8}$$

where the most important component is the autocorrelation function $\langle \Phi | \Phi(t) \rangle$, which represents the overlap between the initial wave packet and the time-evolving wave packet $\Phi(t)$ on the excited surface. Considering the wave packet along a single normal coordinate, the overlap function is given by

$$\langle \phi | \phi(t) \rangle = \sum_{i=1}^{2} \sum_{j=1}^{2} (\vec{\mu}_j \cdot \vec{e}_I)(\vec{\mu}_i \cdot \vec{e}_I) \langle \chi_0 | C_i^* e^{-iH_e t} C_j \, | \chi_0 \rangle \tag{9}$$

where $\vec{e}_I$ is the excitation light polarization vector, and $\vec{\mu}_i$ and C_i are the direction and magnitude of the transition dipole moments. For randomly oriented molecules with respect to the excitation light, the dipole orientation must be averaged over all angles:[17]

$$\langle (\vec{\mu}_j \cdot \vec{e}_I)(\vec{\mu}_i \cdot \vec{e}_I) \rangle = \begin{cases} \frac{1}{3} & \text{when } i = j \\ \frac{1}{3}\cos\beta & \text{when } i \neq j \end{cases} \tag{10}$$

So for the absorption intensities of the parallel and antiparallel scenarios can be written as

$$I_0(\omega) = \frac{1}{3} C\omega \int_{-\infty}^{\infty} \mathrm{e}^{\mathrm{i}(\omega + E_0)t} \sum_{i=1}^{2} \sum_{j=1}^{2} \langle \chi_0 | C_i^* e^{-iH_e t} C_j \, | \chi_0 \rangle \, \mathrm{d}t \tag{11}$$

$$I_{180}(\omega) = \frac{1}{3} C\omega \int_{-\infty}^{\infty} \mathrm{e}^{\mathrm{i}(\omega+E_0)t} \sum_{i=1}^{2}\sum_{j=1}^{2} (-1)^{i+j} \langle \chi_0 | C_i^* e^{-iH_e t} C_j \, | \chi_0 \rangle \, \mathrm{d}t \tag{12}$$

while

$$I_{90} = \frac{1}{2}[I_0 + I_{180}] \tag{13}$$

The relationship between the intensity of any angle β and the parallel and antiparallel intensities can thus be derived:

$$I_\beta = I_{90} + [I_0 - I_{90}] \cos\beta = \frac{1}{2} I_0 [1 + \cos\beta] + \frac{1}{2} I_{180} [1 - \cos\beta] \tag{14}$$

Therefore, the ratio between the antiparallel and parallel components is

$$\frac{I_{180}}{I_0} = \frac{1 - \cos\beta}{1 + \cos\beta} = \tan^2 \frac{\beta}{2} \tag{15}$$

1.4 CALCULATING SPECTRA

With these basic parameters in mind, we now have the tools needed to calculate fits to experimental absorption data. A reasonable set of these parameters must be determined through a combination of experimental absorption spectroscopy, Raman spectroscopy, IR spectroscopy and theoretical calculations using Gaussian.

The magnitude of coupling can be determined directly from the experimental absorption spectrum. As previously discussed, the energy splitting between the lower and upper adiabat in ESMV, and thus the splitting between the two ESMV bands in absorption spectrum, is twice the

magnitude of coupling. The sign of the coupling is more involved and can be determined through the construction of a neighboring orbital model, as will be outlined for an example in the next section.

The frequencies and distortions of the symmetric normal modes can be observed in resonance Raman spectra. During electronic transition to the excited state, the electron density and bonding/antibonding character across the molecule changes. The normal modes with geometric distortions that correspond to these changes will be most distorted and intense in the resonance Raman spectrum. Distortion values can be calculated by measuring the intensities of normal mode Raman peaks and using Savin's formula[18,19]

$$\frac{I_k}{I_{k'}} = \frac{\Delta_k^2 \omega_k^2}{\Delta_{k'}^2 \omega_{k'}^2} \tag{16}$$

where I is the intensity of the mode, Δ is the distortion and ω is the frequency, all measured relative to a reference peak. While symmetric modes add to the overall breadth and structure of the absorption spectrum, the asymmetric modes determine the selection rules and overall intensity of the ESMV bands. However, only symmetric normal modes are enhanced in resonance Raman spectroscopy, and the asymmetric modes must either be obtained from non-resonance Raman or IR spectroscopy or by estimating them relative to their corresponding symmetric mode components.

Here, we will present a brief analysis of a studied compound, 2,3-diphenyl-2,3-diazabicyclo[2,2,2]octane (**1**$^+$, Scheme 1-1), to demonstrate the process of calculating excited state mixed valence spectra.[8]

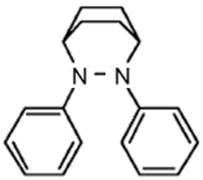

1

Scheme 1-1. Molecular structure of compound **1**.

1.4.1 Neighboring Orbital Model

The neighboring orbital model[20] was designed to aid with determining the sign of the coupling, which can then be used to calculate transition dipole selection rules. This relationship can also be corroborated with group theory derived selection rules.

As discussed in an earlier section, direct bonding where the in-phase combination is stabilized and is lower in energy inherently has negative coupling. By constructing the neighboring orbital and observing if the in-phase or out-of-phase combination is stabilized, the sign of the coupling can be determined. The molecular orbitals are generated from Gaussian calculations, and the transitions between these molecular orbitals are also assigned to absorption bands. Shown in Figure 1-7 is the neighboring orbital model constructed for compound $\mathbf{1}^{+}$.

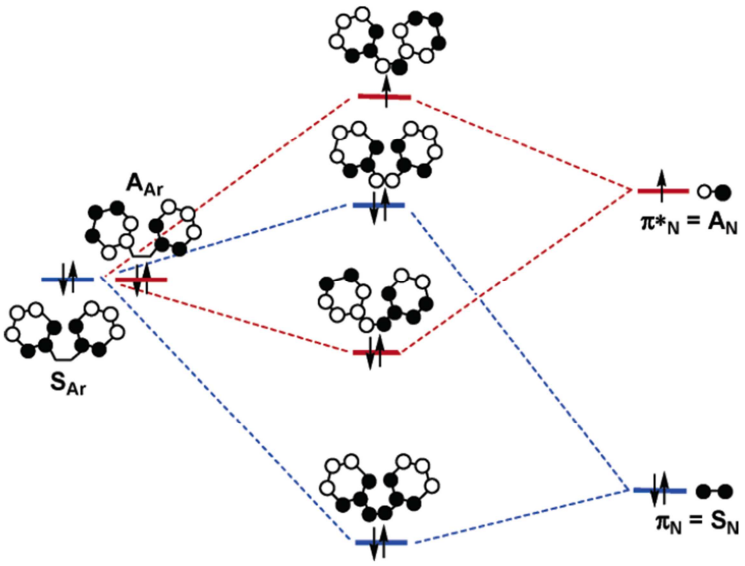

Figure 1-7. Neighboring orbital model for $\mathbf{1}^+$. In-phase and out-of-phase combinations of phenyl π orbitals (as yet uncoupled) on left; π and π* N=N bridge orbitals on right. Coupled orbitals after mixing shown in the center.

Construction of the neighboring orbital model involves identifying the charge bearing units and the bridge. The former, being the phenyl groups, are shown on the left of the figure, while the mediating hydrazine bridge is shown on the right. The molecular orbitals of matching symmetry of each of these units couple to form the adiabatic orbitals in the center. The most significant of these are the orbitals with the most CBU (phenyl group) character, in other words, the orbitals that are closest in energy to the phenyl orbitals, namely, the middle two orbitals. Upon comparing these two, it can be noted that the out-of-phase combination of phenyl orbitals is lower in energy than the in-phase combination. Thus, the coupling for this molecule is positive.

1.4.2 Experimental Data and Calculated Fit

The absorption spectrum of $\mathbf{1}^+$ shown in Figure 1-8 clearly displays two peaks at 17900 cm^{-1} and 25900 cm^{-1}. After optimizing the calculated spectra, the coupling magnitude can be found to be around half of this energy splitting, at 3750 cm^{-1}.

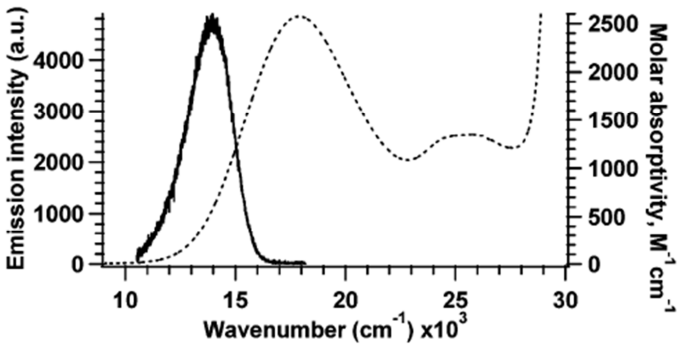

Figure 1-8. Absorption spectrum (dotted line) and emission spectrum (solid line) of $\mathbf{1}^+$.

Frequencies and distortions are determined from the resonance Raman spectra. Shown in Table 1-2 is a brief list of the most intense modes, their frequencies, intensities, distortions and mode assignment (the full table can be seen in the reference).[8]

Frequency (cm^{-1})	Intensity	Δ	Assignment
423	0.5274	0.91	CNNC twist
1273	0.9351	0.40	NN stretch
1413	1.0333	0.48	NN stretch
1489	1.6606	0.31	Ph CC stretch
1586	0.7532	0.38	Ph CC stretch

Table 1-2. Experimental data for the five most intense Raman modes.

Of the many modes observed, the low frequency CNNC twist modes undergo the biggest distortions. Therefore, a 542 cm^{-1} mode observed in experimental IR data was chosen to represent the asymmetric coordinate, and a Δ value of 0.8 comparable to the values of similar symmetric modes observed in Raman. Including this asymmetric mode and the symmetric modes listed in the full table, an absorption spectrum can thus be calculated using the time-dependent theory of spectroscopy briefly described previously. However, one last important parameter remains to be determined, the orientation of the dipoles.

Observation of the molecule and its ground state geometry, the nitrogens have sp^2 hybridization and the angle (β) between the transition dipole moments should be about 120^o. Using Equation 7 and after optimization, the β angle is calculated to be 119^o. The final calculated absorption spectrum (including a damping factor of 1500 cm^{-1}) is shown in Figure 1-9.

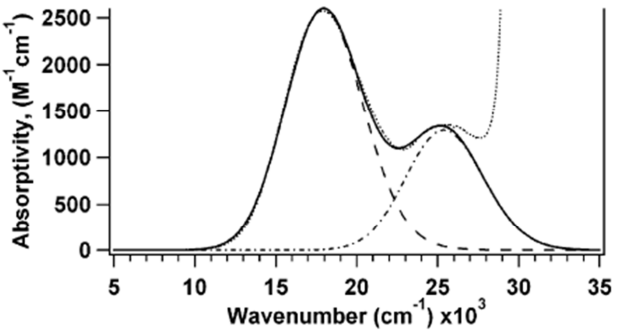

Figure 1-9. Calculated absorption fit (solid line) which is a superposition of the parallel (dot-dashed line) and antiparallel dipole (dashed line) components, shown together with the experimental absorption spectrum (dotted line).

1.5 SUMMARY

In this chapter, we have provided an introduction to the fundamentals of mixed valence, and in particular, excited state mixed valence. We have outlined the parameters that determine the

extent of the coupling and define the excited state mixed valence system. Determining the charge bearing units and constructing a neighboring orbital model aids in understanding how the electronic interactions affect the geometric distortions. From experimental absorption and Raman spectra, the various parameters can be established, and along with the time-dependent theory of spectroscopy, calculated absorption spectra can be fit to the ESMV bands. These analytical methods will be the basis of our studies presented in the following two chapters.

1.6 REFERENCES

(1) Hush, N. S. *Prog. Inorg. Chem.* **1967**, *8*, 391.

(2) Day, P.; Hush, N. S.; Clark, R. J. H. *Phil. Trans. R. Soc. A* **2008**, *366*, 5.

(3) Bailey, S. E.; Zink, J. I.; Nelsen, S. F. *J. Am. Chem. Soc.* **2003**, *125*, 5939.

(4) Hankache, J.; Wenger, O. S. *Chem. Rev.* **2011**, *111*, 5138.

(5) Creutz, C.; Taube, H. *J. Am. Chem. Soc.* **1973**, *95*, 1086.

(6) Hoekstra, R. M.; Dibrell, M. M.; Weaver, M. N.; Nelsen, S. F.; Zink, J. I. *J. Phys. Chem. A* **2009**, *113*, 456.

(7) Lockard, J. V.; Zink, J. I.; Konradsson, A. E.; Weaver, M. N.; Nelsen, S. F. *J. Am. Chem. Soc.* **2003**, *125*, 13471.

(8) Lockard, J. V.; Zink, J. I.; Trieber II, D. A.; Konradsson, A. E.; Weaver, M. N.; Nelsen, S. F. *J. Phys. Chem. A* **2005**, *109*, 1205.

(9) Lockard, J. V.; Zink, J. I.; Luo, Y.; Weaver, M. N.; Konradsson, A. E.; Fowble, J. W.; Nelsen, S. F. *J. Am. Chem. Soc.* **2006**, *128*, 16524.

(10) Zink, J. I.; Shin, K.-S. K. In *Advances in Photochemistry*; Wiley: New York; Vol. 16, pp. 119–214.

(11) Simoni, E.; Reber, C.; Talaga, D. S.; Zink, J. I. *J. Phys. Chem.* **1993**, *97*, 12678.

(12) Hoffmann, R. *Acc. Chem. Res.* **1971**, *4*, 1.

(13) Whangbo, M.-H.; Hoffmann, R. *J. Chem. Phys.* **1978**, *68*, 5498.

(14) Robin, M. B.; Day, P. *Adv. Inorg. Chem. Radiochem.* **1968**, *10*, 247.

(15) Brunschwig, B. S.; Creutz, C.; Sutin, N. *Chem. Soc. Rev.* **2002**, *31*, 168.

(16) Talaga, D. S.; Zink, J. I. *J. Phys. Chem.* **1996**, *100*, 8712.

(17) Lockard, J. V.; Valverde, G.; Neuhauser, D.; Zink, J. I.; Luo, Y.; Weaver, M. N.; Nelsen, S. F. *J. Phys. Chem. A* **2006**, *110*, 57.

(18) Tang, J.; Albrecht, A. C. In *Raman Spectroscopy*; Szynanski, H., Ed.; Plenum Press: New York, 1970; Vol. 2, pp. 33–68.

(19) Warshel, A.; Dauber, P. *J. Chem. Phys.* **1977**, *66*, 5477.

(20) Nelsen, S. F.; Weaver, M. N.; Luo, Y.; Lockard, J. V.; Zink, J. I. *Chem. Phys.* **2006**, *324*, 195.

Chapter 2

Excited State Mixed Valence in Ru Complexes:

Unusual Raman Profiles and Selection Rules

2.1 INTRODUCTION

For molecules with two or more equivalent charge bearing sites, an unpaired electron can reside on either site, and ground state mixed valence can occur because of the presence of electronic communication between the sites. Mixed valence can also occur in the excited state, when the formal charge can reside in either site in the excited state after an electronic transition occurs.[1,2] Mixed valence systems are typically represented by M-B-M, where there are two equivalent charge bearing sites M, with a bridging unit B connecting them. For ground state mixed valence (GSMV), the two mixed valence configurations are [M$^{\bullet}$-B-M] are [M-B-M$^{\bullet}$]. An example of excited state mixed valence could be a system with symmetric charge distribution in the ground state [M-B^{2+}-M], while electronic transition leads to two possible and equivalent excited states [M^{-}-B^{3+}-M] and [M-B^{3+}-M^{-}]. In GSMV, only a single band, the intervalence band, is observed in absorption spectroscopy.[3] In contrast, ESMV consists of two transitions that may have different intensities due to selection rules and are separated by twice the effective coupling of the electronic communication between the sites.

Both GSMV and ESMV have been studied by utilizing the time-dependent theory of absorption[4], resonance Raman[5-9], and emission spectroscopies. Distortions of vibrational normal modes, while difficult to acquire with unresolved absorption spectra, can be measured with resonance Raman spectra excited at the transition of interest. These relative distortion values can then be utilized to interpret and analyze the mixed valence systems and coupled states.[10-15]

In this study, we examine two related ESMV complexes, *trans*- and *cis*-di-(4-acetylpyridine)-tetraamineruthenium (II) hexafluorophosphate (**RuT** and **RuC**), and as a comparison of their absorption spectra, the mono ligand version of these complexes (**RuM**).[16] The structure of these

three complexes are shown in Scheme 2-1. The ruthenium metal center has a +2 oxidation state in the ground state, and when excited, metal-to-ligand charge transfer (MLCT) to the 4-acetylpyridine ligand occurs.[17-20] In the case of **RuT** and **RuC**, two equivalent ligands are possible for MLCT, and thus ESMV is observed. However, **RuM**, having only one ligand available for MLCT, will not have mixed valence occurring and only one absorption band is found.

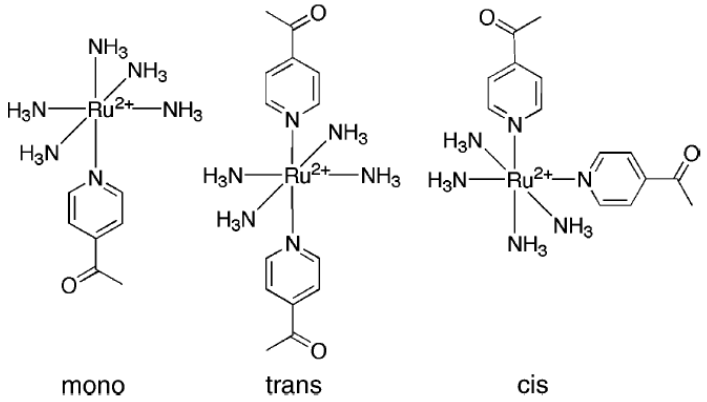

Scheme 2-1. The three ruthenium (II) complexes investigated in this study.

The two ESMV systems are almost identical, except for their relative orientations of the two charge bearing ligands. **RuT** has the ligands at 180^{o} away from each other, while in **RuC**, the ligands are roughly 90^{o} apart. This presents a good comparison of how selection rules differ with different orientation of the same ligand, and this is evident in the absorption spectra where both complexes display two EMSV bands but their relative intensities of the two bands are extremely different. Further examination of their resonance Raman profiles also reveals a second interesting phenomenon. While typical Raman profiles are expected to follow the contour of the absorption spectrum, this is only observed for **RuT** and not **RuC**. In this chapter, we will discuss

how the difference in dipole orientational averaging between absorption and Raman spectroscopies will result in this observation.

2.2 EXPERIMENTAL SECTION

2.2.1 Synthesis

Trans-di-(4-acetylpyridine)-tetraammineruthenium (II) hexafluorophosphate

The compound was synthesized using several procedures in literature.[21-24] A 30 mL aqueous solution containing 3.0 g of $[Ru^{III}(NH_3)_6]Cl_3$ was mixed with 30 mL of concentrated hydrochloric acid and refluxed for 3 hours. It was then filtered and washed with dilute HCl then methanol, and dried to acquire the bright yellow solid $[Ru^{III}(NH_3)_5Cl]Cl_2$. 2.71 g of $[Ru^{III}(NH_3)_5Cl]Cl_2$ was then dissolved in 108 mL of water, 3.82 g of $NaHSO_3$ added, heated at 75 ℃ and bubbled with SO_2 gas for an hour. The solution was allowed to cool to room temperature, then filtered, washed with water then methanol, and dried to acquire 1.68 g of beige $Ru^{II}(NH_3)_4(HSO_3)_2$. This was then heated in 194 mL of HCl to dissolve, filtered and left to recrystallize to deep brown red needle crystals $[Ru(NH_3)_4(SO_2)Cl]Cl$. 200 mg of this compound was added to 0.47 mL of 4-acetylpyridine and 12 mL of water and stirred for five minutes at room temperature. 10 mL of 3 M CF_3SO_3H was then added, the solution cooled in a fridge to form orange precipitate. This was then filtered and washed with ethanol and diethyl ether, and dried to form the orange solid $[Ru(NH_3)_4(SO_2)(acpy)](CF_3SO_3)_2$. This was then dissolved in 6 mL of 1 M HCl forming a deep orange clear solution, 30% H_2O_2 was added dropwise until solution becomes pale yellow, then 6 mL of concentrated HCl and 30 mL acetone were added.

The solution was cooled to form pale beige precipitate, which was then filtered and washed with ethanol and diethyl ether, recrystallized twice, to form $[Ru(NH_3)_4(SO_4)(acpy)]Cl$. 94 mg of this compound was dissolved in 1.5 mL water, and large excess of 4-acetylpyridine was added. The solution was bubbled with Ar gas for 15 minutes, then 1 drop of trifluoroacetic acid and zinc amalgam were added. The reaction was bubbled with Ar gas continuously for two hours in the dark. Finally, 3 mL of freshly prepared, deaerated, saturated KPF_6 aqueous solution was added. The solution was cooled to precipitate, and the product filtered to acquire the brown solid final product $[Ru(NH_3)_4(acpy)_2]PF_6$.

***Cis*- and *mono*-di-(4-acetylpyridine)-tetraamineruthenium (II) hexafluorophosphate**

The cis and mono complexes were synthesized by former group member Edward Plummer according to known procedures.[25]

2.2.2 Absorption Spectroscopy

Absorption spectra were taken of samples in acetonitrile solutions at room temperature. Spectra were obtained using a CARY 5000 UV-vis-nIR spectrophotometer.

2.2.3 Resonance Raman Spectroscopy

Samples were in the form of pressed pellets mixed with sodium sulfate as a standard. Raman spectra were collected with a triple monochromator equipped with a Princeton Instruments LN-CCD. Spectra were excited with multiple visible lines of a Coherent Krypton ion laser and Argon ion laser. Powers were kept at 20 mW or less with the pellet continuously spinning to minimize degradation. However, minimal degradation was still present, and each spectrum was taken at different spots on the homogeneous pellet to avoid degrading intensity measurements. Several

pellets were required to achieve this, and intensities between different pellets were normalized with a common excitation wavelength and Raman peak.

2.2.4 DFT Calculations

Molecular orbitals were calculated in Gaussian 09[26] using the B3LYP/LANL2DZ method and results imaged with GaussView 5. Calculated normal mode frequencies were also obtained, and experimental modes were assigned with the aid of Gaussian calculations.

2.3 THEORETICAL AND NUMERICAL METHODS

The time-dependent theory of molecular spectroscopy[4,10] is utilized to understand and calculate the electronic absorption spectra and Raman profiles in this study. Coupled electronic states can also be interpreted with the time-dependent approach.[27] A brief presentation of this theory is given here.

2.3.1 Absorption Spectroscopy

In time-dependent theory, the fundamental equation in the frequency domain describing absorption spectra is

$$I(\omega) = C\omega \int_{-\infty}^{\infty} \mathrm{e}^{\mathrm{i}\omega t} \left\{ \langle \Phi | \Phi(t) \rangle \exp\left(-\Gamma^2 t^2 + \frac{iE_{00}}{h} t \right) \right\} \mathrm{d}t \qquad (1)$$

where $I(\omega)$ is the absorbance intensity at frequency ω, E_{00} is the electronic origin transition energy, and Γ is a phenomenological damping factor, which accounts for other modes and the bath that cause broadening of the absorption band. An initial wavepacket Φ makes a vertical

transition to the excited state potential surface. As the excited state surface is generally displaced relative to the ground state, the wavepacket will not be stationary and will propagate on the excited state surface. The overlap between the initial wavepacket and this time-evolving wavepacket $\Phi(t)$ is the autocorrelation function $\langle\Phi|\Phi(t)\rangle$.

In the usual case of multiple normal coordinates, but neglecting coupling between them, the total overlap function is given as

$$\langle\Phi|\Phi(t)\rangle = \prod_k \langle\phi^k|\phi^k(t)\rangle \tag{2}$$

where ϕ^k is the wave packet evolving along the k^{th} normal coordinate.

The evolving wave packet is given by the time-dependent Schrödinger equation. When there are two coupled excited states (excited state mixed valence), both time-evolving wavepackets must be calculated:

$$i\frac{\partial}{\partial t}\begin{pmatrix}\phi_1\\ \phi_2\end{pmatrix} = \begin{pmatrix}H_1 & H_{12}\\ H_{21} & H_2\end{pmatrix}\begin{pmatrix}\phi_1\\ \phi_2\end{pmatrix} \tag{3}$$

The off-diagonal H_{ij}'s are the coupling between the two diabatic potentials and transfer wavepacket amplitude between the states. The Hamiltonians H_i are given by

$$H_i = -\frac{1}{2M}\nabla^2 + V_i(Q) \tag{4}$$

Where the first term is the nuclear kinetic energy operator and the second is the potential energy operator, often modeled for simplicity as harmonic potential curves $V_i(Q) = \frac{1}{2}k_i(Q \pm \Delta Q)^2$. The

force constant is $k_i = 4\pi^2 M(\hbar\omega_i)^2$ where ω_i is the frequency along the particular normal coordinate Q. The total Hamiltonian serves to propagate the wavepacket along the potential.

For two coupled electronic states, the autocorrelation function is written as

$$\langle\phi|\phi(t)\rangle = \sum_{i=1}^{2}\sum_{j=1}^{2}(\vec{\mu}_j \cdot \vec{e}_I)(\vec{\mu}_i \cdot \vec{e}_I)\langle e_i|\langle\chi_0|C_i^* e^{-iH_e t} C_j\,|\chi_0\rangle|e_j\rangle \quad (5)$$

where $|\chi_0\rangle$ is the initial wave function from the electronic ground state. It is transitioned to the two excited states $|e_i\rangle$ where $i = 1,2$ with the dipole operator, given by $\vec{\mu}_i$ and C_i, the dipole direction and magnitude respectively. The polarization vector of the excitation light is $\vec{e}_I$.

For the ESMV systems studied here, the transition dipoles are equal in magnitude, and the relative orientation between them is defined by the angle β. As molecules are randomly oriented with respect to $\vec{e}_I$, the dipole orientation must be averaged over all angles to account for this:

$$\langle(\vec{\mu}_j \cdot \vec{e}_I)(\vec{\mu}_i \cdot \vec{e}_I)\rangle = \begin{cases} \frac{1}{3} & \text{when } i = j \\ \frac{1}{3}\cos\beta & \text{when } i \neq j \end{cases} \quad (6)$$

The autocorrelation function can thus be simplified to:

$$\langle\phi|\phi(t)\rangle = \frac{1}{3}[\langle\phi_1|\phi_1(t)\rangle + \cos\beta\,\langle\phi_1|\phi_2(t)\rangle + \cos\beta\,\langle\phi_2|\phi_1(t)\rangle + \langle\phi_2|\phi_2(t)\rangle] \quad (7)$$

2.3.2 Raman Spectroscopy

Raman intensities, instead of being directly proportional to the overlap like absorption intensities, are proportional to the square of the polarizability α. The intensities are given by the equation

$$I_R(\omega) = \omega_I \omega_s^3 |\alpha|^2 \tag{8}$$

while the polarizability for a two-state coupled system is

$$\alpha(\omega) = \int_0^\infty e^{i\omega_I t - \Gamma t} \sum_i^2 \sum_j^2 (\vec{\mu}_i \cdot \vec{e}_s)(\vec{\mu}_j \cdot \vec{e}_I) \langle \phi_f | \phi(t) \rangle_{ij} \, \mathrm{d}t \tag{9}$$

In addition to the polarization vector of the excitation light $\vec{e}_I$, Raman scattering is a two photon process, so the polarization vector of the scattered light $\vec{e}_s$ must also be considered. With the presence of the second light vector and as the Raman intensity is proportional to the square of the polarizability, angle averaging is a far more complicated calculation, and can be calculated to be

$$\langle |\alpha|^2 \rangle = \sum_{n=1}^{3} f_n(\theta) g_n(\beta, \omega_I) \tag{10}$$

where θ is the angle between $\vec{e}_I$ and $\vec{e}_s$, and

$$\begin{cases} f_1(\theta) = (2\cos^2\theta + 1)/15 \\ f_2(\theta) = (3\cos^2\theta - 1)/15 \\ f_3(\theta) = (\sin^2\theta + 1)/15 \end{cases} \tag{11}$$

$$\begin{cases} g_1(\beta,\omega_I) = \sum_{i=1}^{2}|\alpha_{ii}|^2 + (\cos^2\beta)\{|\alpha_{12}|^2 + |\alpha_{21}|^2\} + 2\cos\beta\, p + 2\cos^2\beta\, q \\ g_2(\beta,\omega_I) = \sin^2\beta\, p \\ g_3(\beta,\omega_I) = \sin^2\beta\,\{|\alpha_{12}|^2 + |\alpha_{21}|^2\} \end{cases} \quad (12)$$

and

$$\begin{cases} p = \alpha_{11}^*\alpha_{12} + \alpha_{11}^*\alpha_{21} + \alpha_{12}^*\alpha_{11} + \alpha_{12}^*\alpha_{22} + \alpha_{21}^*\alpha_{11} + \alpha_{21}^*\alpha_{22} + \alpha_{22}^*\alpha_{12} + \alpha_{22}^*\alpha_{21} \\ q = \alpha_{11}^*\alpha_{22} + \alpha_{21}^*\alpha_{12} \end{cases} \quad (13)$$

When the excitation light source is a laser beam, the incident light is polarized in one direction only. However, scattered light will have components in all three axes. When $\vec{e}_s$ is along the same axis as $\vec{e}_I$, the angle θ is equal to 0; along the other two axes, $\theta = 90°$. Summing all three axes and letting $\alpha_{11} = \alpha_{22}$, $\alpha_{12} = \alpha_{21}$ for ESMV systems with equivalent charge bearing sites,

$$\langle|\alpha|^2\rangle = 2[(2 + \cos 2\beta)(|\alpha_{11}|^2 + |\alpha_{12}|^2) + 4\cos\beta\,(\alpha_{11}^*\alpha_{12} + \alpha_{12}^*\alpha_{11})] \quad (14)$$

2.4 RESULTS

2.4.1 Absorption spectra

Absorption spectra of the complexes **RuM**, **RuT**, and **RuC** in acetonitrile solution are shown in Figure 2-1. **RuM** displays a single transition band at 19213 cm^{-1}, while **RuC** exhibits two bands with similar intensities at 19080 cm^{-1} and 22775 cm^{-1}. **RuT** has a strong absorption band at 18754 cm^{-1} and a very weak shoulder at higher energies, in the region where **RuC** has its higher band.

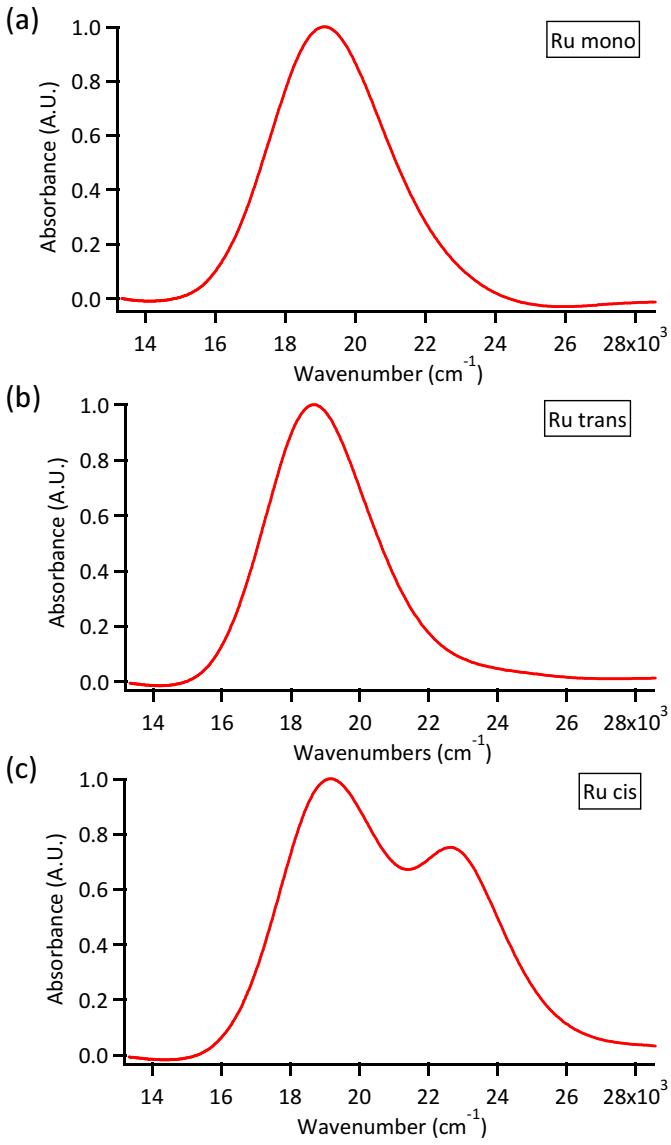

Figure 2-1. Absorption spectra of (a) **RuM** (b) **RuT** and (c) **RuC** in acetonitrile.

2.4.2 Resonance Raman spectra

Resonance Raman spectra were collected using thirteen excitation wavelengths. The full resonance Raman spectra of **RuT** and **RuC** are shown in Figure 2-2. The most intense peaks are in the 1000-1600 cm^{-1} region which is typical of 4-acetylpyridine vibrational modes.

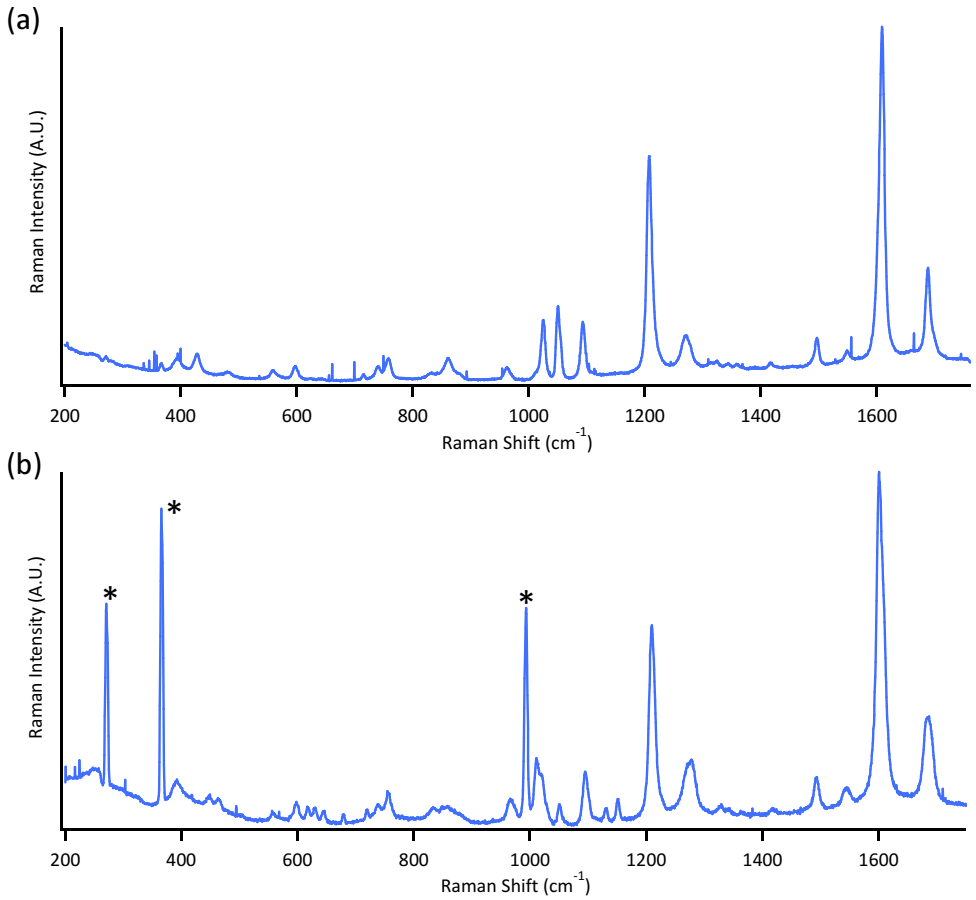

Figure 2-2. Resonance Raman spectra of (a) **RuT** and (b) **RuC**, excited at 457 nm. Peaks marked with * in (b) are laser plasma lines and Na_2SO_4 standard peak at 991 cm^{-1}.

Peak intensities were integrated and normalized to Na_2SO_4 standard peaks. Peak intensities obtained from 465.8 nm excitation are presented in Table 2-1 (**RuT**) and 2-2 (**RuC**), along with the experimental and calculated frequencies and mode assignments. Intense modes for **RuC** and **RuT** are similar with slight shifts in frequencies, as they are modes with motion in the 4-acetylpyridine ligands which are identical for the two complexes.

Exp. ω (cm^{-1})	Calc. ω (cm^{-1})	Relative intensity	Δ	Assignment
394	383	0.16	1.02	Ru-N(NH_3) stretch
429	425	0.09	0.68	Py ring out of plane wag (N(py) stationary)
754	761	0.28	0.70	Py ring out of plane wag
1024	1019	0.87	0.90	Ru-N(py) stretch & py ring breathing
1053	1074	0.47	0.64	In plane alternating C_2-C_3-C_4 & C_1-N-C_5 bend
1093	1127	0.80	0.81	$N_{(py)}$-Ru-$N_{(py)}$ see-saw, ring in plane distortion
1207	1248	4.22	1.69	C_3-$C_{(carb)}$, C_1-C_2, C_4-C_5 stretch, C-H in plane wag
1272	1297	0.95	0.76	$N_{(py)}$-Ru-$N_{(py)}$ see-saw, ring dist., C_3-$C_{(carb)}$ stretch
1608	1583	9.71	1.92	$N_{(py)}$-Ru-$N_{(py)}$ see-saw, ring dist., N-C stretch
1692	1709	1.41	0.69	Amines CW & CCW rock in a plane around Ru

Table 2-1. **RuT** experimental and calculated Raman frequencies, intensities, dimensionless distortions and mode assignments at 465.8 nm excitation. Intensities are relative to the 991 cm^{-1} peak of standard Na_2SO_4. Relative distortions are calculated using Savin's formula.

Exp. ω (cm^{-1})	Calc. ω (cm^{-1})	Relative intensity	Δ	Assignment
393	384	0.17	1.05	Ru-N(NH_3) stretch
449	430	0.13	0.79	Py ring out of plane wag (N(py) stationary)
756	763	0.24	0.64	Py ring out of plane wag
1019	1018	0.43	0.64	Ru-N(py) stretch & py ring breathing
1051	1074	0.10	0.29	In plane alternating C_2-C_3-C_4 & C_1-N-C_5 bend
1095	1133	0.40	0.57	$N_{(py)}$-Ru-$N_{(py)}$ see-saw, ring in plane distortion
1210	1254	1.48	0.99	C_3-$C_{(carb)}$, C_1-C_2, C_4-C_5 stretch, C-H in plane wag
1278	1299	0.92	0.75	$N_{(py)}$-Ru-$N_{(py)}$ see-saw, ring dist., C_3-$C_{(carb)}$ stretch
1602	1583	3.27	1.12	$N_{(py)}$-Ru-$N_{(py)}$ see-saw, ring dist., N-C stretch
1685	1720	1.07	0.61	Amines CW & CCW rock in a plane around Ru

Table 2-2. **RuC** experimental and calculated Raman frequencies, intensities, dimensionless distortions and mode assignments at 465.8 nm excitation. Intensities are relative to the 991 cm^{-1} peak of standard Na_2SO_4. Relative distortions are calculated using Savin's formula.

Raman profiles were plotted with the intensities calculated from the resonance Raman spectra over thirteen excitation wavelengths. The profiles of four of the most intense modes are shown in Figure 2-3 compared to the absorption spectra. For **RuT**, Raman profiles follow the general contour of the absorbance as expected. However, **RuC** profiles for all modes lack intensity in the region of the higher absorption band.

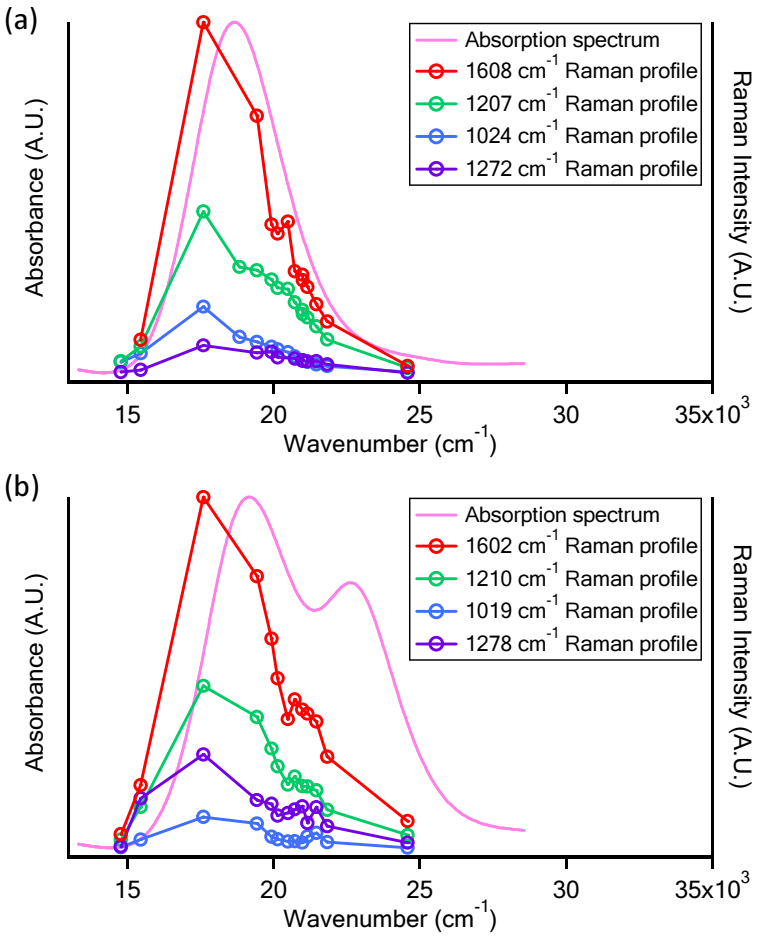

Figure 2-3. Resonance Raman profiles for four of the most intense modes compared to absorption spectra for (a) **RuT** and (b) **RuC**.

2.5 DISCUSSION

2.5.1 Excited State Mixed Valence

The excited state mixed valence for the trans and cis complexes can be represented by two coupled potential energy surfaces along an asymmetric normal coordinate, as shown in Figure 2-4. In the ground state, represented by a single harmonic potential energy surface with its minimum at zero along the coordinate (Q = 0), charge is localized on the Ru metal center. As the Ru complex absorbs a photon, metal-to-ligand charge transfer to one of the 4-acetylpyridine

ligands occurs. In the uncoupled diabatic basis, the excited state charge distribution is asymmetric, and two identical excited state surfaces represent the electron density localized on either ligand. These surfaces are equal in energy at Q = 0, and are displaced by –Δ and +Δ along the asymmetric coordinate.

When the diabatic surfaces couple, two non-degenerate adiabatic surfaces arise with an energy splitting of $2H_{eff}$, both with zero slope at Q = 0 (shown by the dotted line in Figure 2-4). This energy difference corresponds to the energy difference observed between the two absorption bands in the cis complex. In the trans complex, the higher band is present only as a small shoulder, and can be understood by selection rules which will be discussed later.

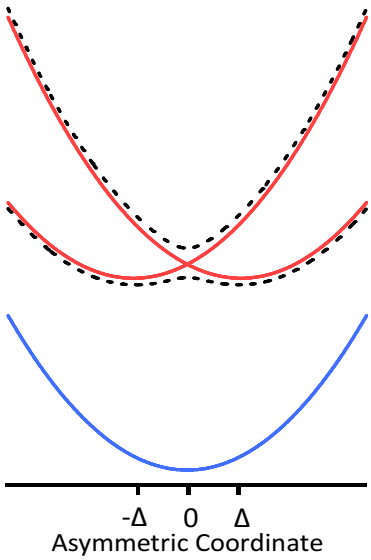

Figure 2-4. Potential energy surfaces of an ESMV system. Blue solid line: ground electronic state. Red solid line: excited state uncoupled degenerate diabats. Black dotted line: excited state coupled adiabats, energy splitting of twice the effective coupling.

2.5.2 Neighboring Orbital Model (NOM)

A simple neighboring orbital model (Figure 2-5) is used to depict how the ligand and metal orbitals interact. The NOM assists in evaluating how charge bearing units couple and the sign of the coupling.[28-31] The uncoupled ligand π orbitals can be represented by either of the ligand localized orbitals π_{1a} and π_{1b} (also the higher energy π_{2a} and π_{2b}), or by their linear combinations: the in-phase $\pi_{1a} + \pi_{1b}$ and out-of-phase $\pi_{1a} - \pi_{1b}$. In the diabatic basis without coupling, these are degenerate in energy, and are shown on the right hand side of the NOM, while the metal d orbital is shown on the left. Coupling between the ligand orbitals is mediated through the metal, and occurs when the ligand π orbital linear combinations mix with the symmetry appropriate metal d orbital. The energy degeneracy is removed when coupling is present. This adiabatic picture is shown in the center of the NOM.

For the Ru trans complex with D_{2h} point group, in-phase $\pi_{1a} + \pi_{1b}$ (and $\pi_{2a} + \pi_{2b}$) has B_{2u} symmetry while the out-of-phase combinations are of B_{3g} symmetry. The in-phase combinations can thus couple with the Ru metal d_{yz} orbital of the same symmetry. As there are three sets of orbitals of the same symmetry, all three will interact together, forming the HOMO-8, HOMO and LUMO+1 orbitals of **RuT**. HOMO-8, being closest in energy to the ligand $\pi_{1a} + \pi_{1b}$ combination, is predominantly $\pi_{1a} + \pi_{1b}$ character, bonding with d_{yz}. The LUMO+1, being closest to the $\pi_{2a} + \pi_{2b}$ combination, is predominantly $\pi_{2a} + \pi_{2b}$ character, but anti-bonding with d_{yz}. The HOMO on the other hand, is a mixture of the two linear combinations, with nodal patterns that are similar to both, and forming anti-bonding between the ligand orbitals and metal d_{yz}. The out-of-phase linear combinations do not have the correct symmetry to interact with metal d orbitals and thus remain non-bonding, forming the HOMO-7 and LUMO of **RuT**.

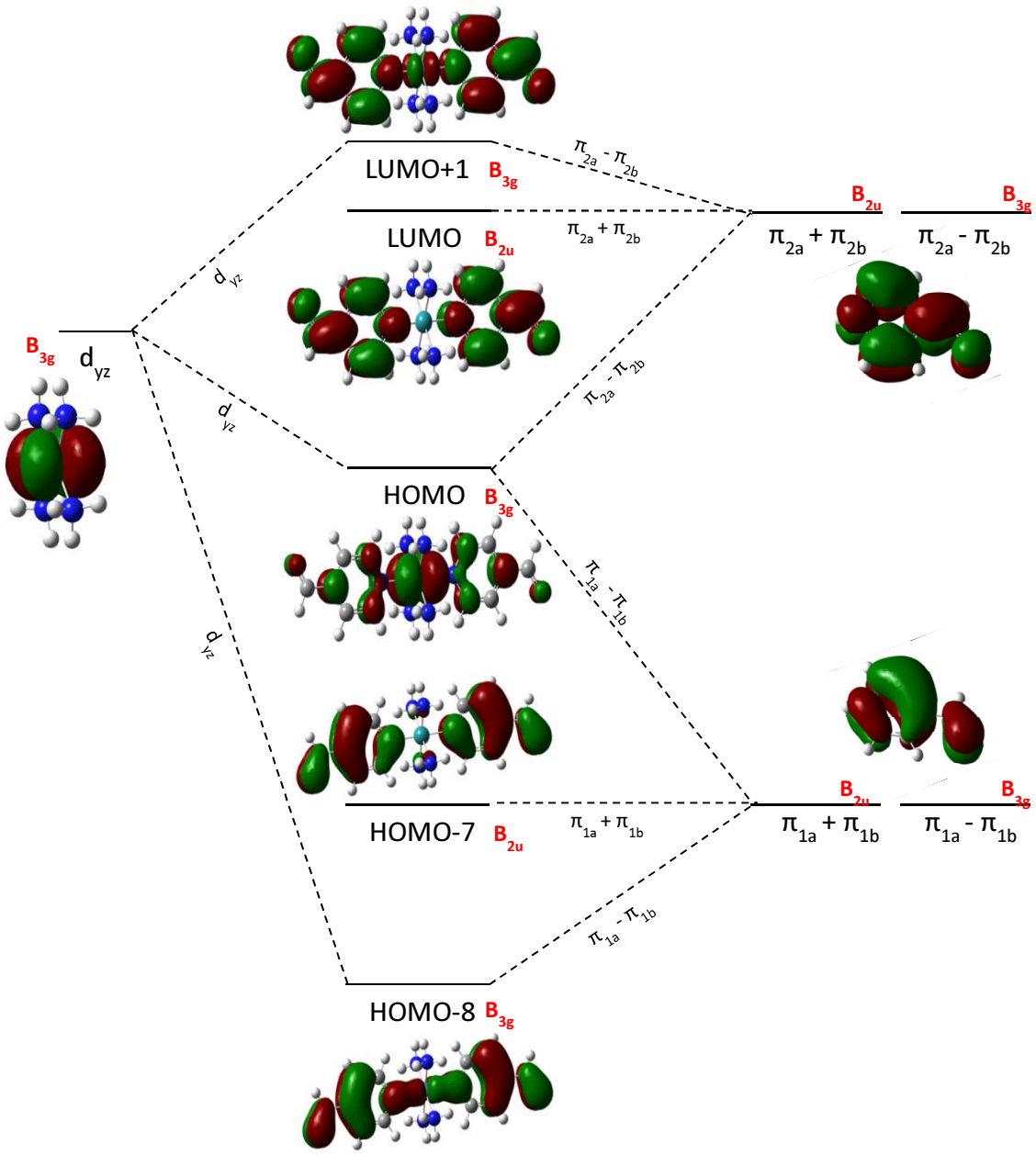

Figure 2-5. Neighboring orbital model for **RuT**. Metal center d orbital shown in left column, linear combinations of the uncoupled ligand orbitals shown in right column. Coupling is mediated through metal center to give adiabatic molecular orbitals in center column. Symmetry assigned in D_{2h} point group: HOMO → LUMO transition is allowed, while HOMO → LUMO+1 is forbidden due to symmetry selection rules.

The ligand π_{2a} and π_{2b} orbitals that are coupled through the metal d_{yz} form the LUMO and LUMO+1, and these correspond to the two non-degenerate adiabatic surfaces as described for Figure 2-4. As the in-phase combination of the mixed valence system is lower in energy, the sign of the coupling is determined to be negative.

An analogous depiction of the NOM can be given for **RuC** in the C_2 point group (Figure 2-6). The two 4-acetylpyridine ligands in a cis configuration are tilted from each other as is shown in the Gaussian calculations. The in-phase ligand orbital combinations are of A symmetry and couple with the metal d orbitals. They are allowed to interact with a combination of the three metal d orbitals of the correct A symmetry (d_{xy}, d_{z^2}, $d_{x^2-y^2}$), forming a mixture of the metal center orbital in the adiabatic MO. In the NOM shown here, only the d_{xy} is represented for simplicity. On the other hand, the out-of-phase combinations, although being of the same B symmetry as the d_{xz} and d_{yz} orbitals, have poor overlap due to the tilted ligands, and are almost non-interacting. Similar to **RuT**, the LUMO and LUMO+1 are the coupled π_{2a} and π_{2b} orbital combinations, with the in-phase combination being lower in energy, and thus have negative coupling.

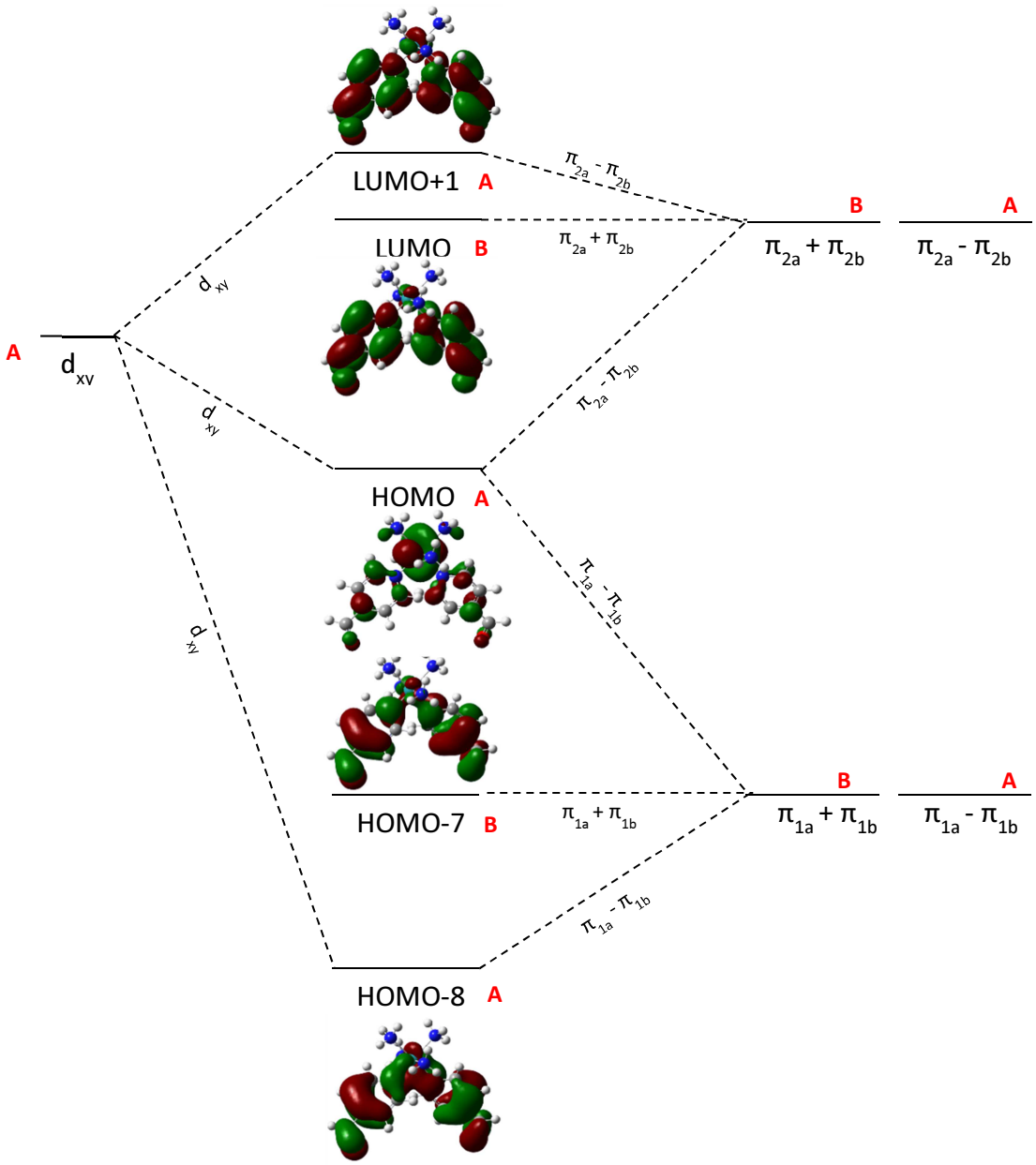

Figure 2-6. Neighboring orbital model for **RuC**, analogous to NOM for **RuT**. Symmetry assigned in C_2 point group; both HOMO → LUMO and HOMO → LUMO+1 transitions are allowed due to symmetry selection rules.

2.5.3 Selection Rules and Absorption Band Assignment

Two absorption bands can be observed for **RuC**, whereas only one band is present in the mono-ligand complex (Figure 2-1). The two bands are due to the excited state mixed valence observed when two ligand orbitals are coupled. However, in **RuT**, there is only a slight shoulder at the higher energy band, and the absorption spectrum is composed of predominantly the lower energy band. The assignment of these mixed valence bands can be achieved by considering selection rules in group theory.

As discussed earlier, the HOMO and LUMO+1 orbitals of **RuT** are of B_{3g} symmetry in the D_{2h} point group, while the LUMO is B_{2u} symmetry. According to selection rules, an electronic transition from HOMO to LUMO is allowed while HOMO to LUMO+1 is forbidden. This corresponds to the high intensity band observed at lower energy (HOMO → LUMO). The small shoulder at higher energy is caused by the dipole forbidden transition (HOMO → LUMO+1).

The relative intensities of the two mixed valence bands can also be explained by examining the transition dipole moments. This method has been described in previous papers;[28,30,31] however, that method involved the assumption of a symmetric ground state and is not suitable for analyzing these Ru complexes (asymmetric HOMO). An expanded model has been developed, giving a correct analysis of the lower energy band being allowed, and will be discussed in greater detail in Chapter 3.

For **RuC**, both HOMO and LUMO+1 are of A symmetry while LUMO is of B symmetry in the C_2 point group. Electronic transitions from HOMO to both LUMO and LUMO+1 are allowed according to selection rules, and this is observed in the two intense bands observed in the absorption spectrum.

2.5.4 Resonance Raman Analysis

Resonance Raman peaks contain information about the electronic transition with which it is in resonance. Both the transitions of HOMO → LUMO and HOMO → LUMO+1 involve a large change in the nodal pattern of electron density on the ligands. Therefore, vibrational modes involving motion across the ligand will be greatly enhanced in the Raman spectrum taken in resonance with these two bands. As presented in Tables 2-1 and 2-2, the majority of the intense peaks are in the 1000-1700 cm^{-1} region, and are assigned to 4-acetylpyridine vibrational modes with the aid of Gaussian calculations and comparison to literature.[16,32] In particular, the two modes at 1608 and 1207 cm^{-1} are considerably more enhanced than the rest. These modes involve C=C and C=N stretches that are expected to undergo a large displacement when an electron is excited into the ligand π orbital that cause large changes in bonding/anti-bonding character across those bonds. In addition, a highly enhanced mode at 394 cm^{-1} corresponds to the symmetric stretch of the Ru-N(amine) bonds. As the ruthenium metal is formally oxidized in MLCT, the greatest bond length change will be the bonds to the ligands with greatest electrostatic nature, namely the amines. This is consistent with that observed in literature.[33]

These most intense Raman symmetric modes provide overall width to the absorption spectrum. From the experimentally acquired relative intensities of each mode, their relative dimensionless distortions can be calculated using Savin's formula,[34,35] and are shown in Tables 2-1 and 2-2.

2.5.5 Absorption Spectrum Calculated Fit

By using the dimensionless distortions obtained from the resonance Raman spectrum, the absorption spectrum can be fit using Equation 1. The distortions are found relative to the standard and the total bandwidth of the absorption band is used to determine the absolute values

from the set of relative distortion values. Asymmetric modes are important as they make the dipole forbidden transition vibronically allowed. However, only symmetric modes are enhanced in the resonance Raman spectra. Therefore, we include only the most representative asymmetric mode by considering the most intense symmetric mode (the 1608 cm^{-1} mode) present in the Raman spectra. Asymmetric modes should have symmetric counterparts at very similar Raman shifts. In our calculations, we use an asymmetric mode of 1600 cm^{-1} and distortion of 0.995. The four most intense symmetric modes with largest distortions are included in the calculations. For **RuT**, these modes are 1608 cm^{-1} (Δ = 0.995), 1207 cm^{-1} (Δ = 0.873), 1024 cm^{-1} (Δ = 0.468) and 1272 cm^{-1} (Δ = 0.384), while for **RuC**, they are 1602 cm^{-1} (Δ = 0.995), 1210 cm^{-1} (Δ = 0.887), 1019 cm^{-1} (Δ = 0.567) and 1278 cm^{-1} (Δ = 0.664).

The experimental absorption spectra do not display resolved vibronic structure, therefore, a large phenomenological damping factor of $\Gamma = 600\ cm^{-1}$ is applied to match the smooth bands. The damping factor accounts for the loss of the wavepacket to the bath. As earlier discussed, the energy splitting between the two ESMV bands is equivalent to two times the coupling magnitude. A coupling magnitude of 1800 cm^{-1} is used in our calculations. To produce the calculated absorption spectra, the E_{00} of 17800 cm^{-1} is also included.

RuT has its two equivalent ligands at 180^o from each other. In other words, its transition dipoles to the two ligands are arranged in an antiparallel orientation; they are equal in magnitude but opposite in sign. Therefore, we only need to calculate the spectrum resulting from antiparallel dipoles, and this transition corresponds to the lower energy allowed band observed for **RuT**. The calculated fit is shown in Figure 2-7a.

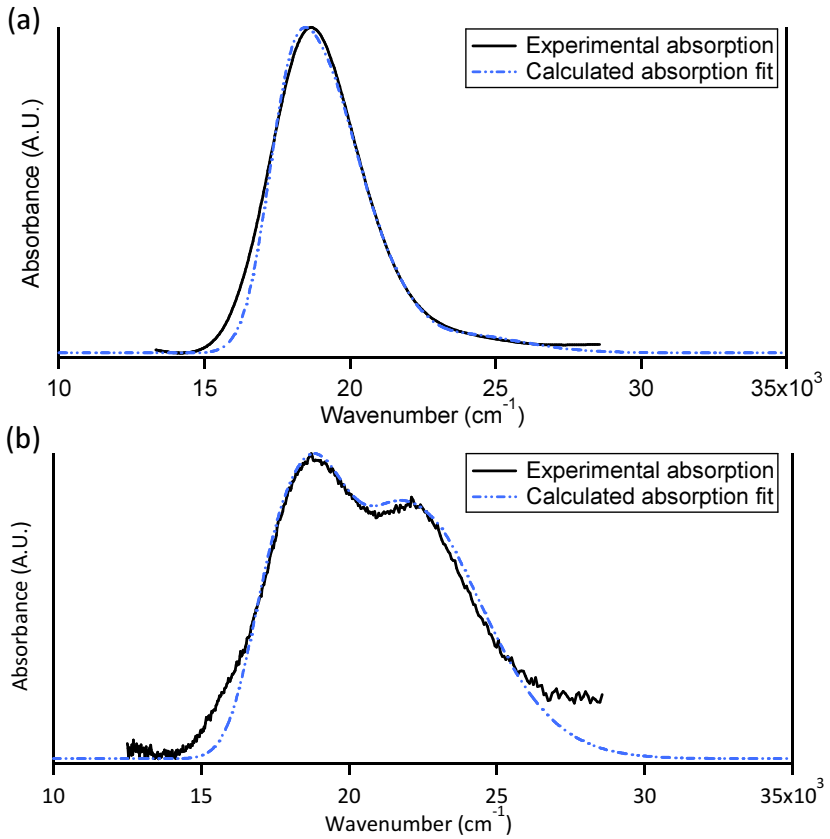

Figure 2-7. Calculated and experimental absorption spectra of (a) **RuT** and (b) **RuC**.

For **RuC** however, the ligands are arranged roughly 90° apart. This angle of relative orientation between the dipoles is defined as angle β. When β equals 180°, dipoles are antiparallel and opposite in sign. When β equals 0°, dipoles are parallel and have the same sign. Parallel and antiparallel dipoles result in different selection rules that determine, along with the sign of the coupling, which of the ESMV bands is allowed. These selection rules will be further discussed in Chapter 3.

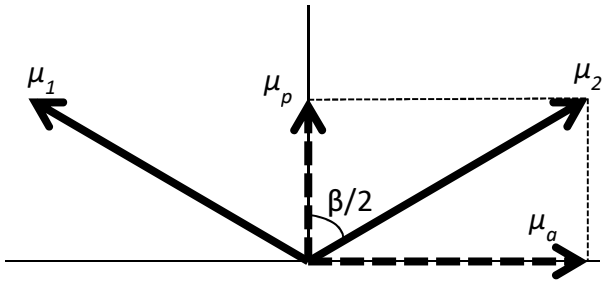

Figure 2-8. Depiction of transition dipoles μ_1 and μ_2 with vector components projected onto the orthogonal parallel and antiparallel components.

Transition dipole moments can be considered to have vector components in two orthogonal directions, as depicted in Figure 2-8. As shown in the diagram, dipoles μ_1 and μ_2 both have projections in the same direction along the axis bisecting them, corresponding to the parallel dipole component μ_p. Along the axis perpendicular to the bisecting axis, their projections will be in opposite directions, corresponding to the antiparallel dipole component μ_a. Because oscillator strength is proportional to the square of the transition dipole, the intensity ratio of the two ESMV bands can be related to the trigonometric relationship between the dipoles:

$$\frac{f_a}{f_p} = \frac{\mu_a^2}{\mu_p^2} = \frac{\mu^2 \sin^2 \frac{\beta}{2}}{\mu^2 \cos^2 \frac{\beta}{2}} = \tan^2 \frac{\beta}{2} \qquad (15)$$

When β is at an angle between 0^o and 180^o, the resulting spectrum can be calculated as a weighted sum of the parallel and antiparallel components using Equation 15. The β angle used to achieve a good absorption fit for **RuC** is 105^o. Although this angle may seem fairly different from the assumed 90^o in an octahedral complex, it is in fact only 7^o from the octahedral axes for each ligand. This difference can be understood from two factors. First of all, the steric repulsion between the bulky 4-acetylpyridine ligands compared to the other amine ligands naturally results in a larger angle separating them. Secondly, as shown from Gaussian calculations, the 4-

acetylpyridine ligand planes are not perpendicular to each other, but instead, are offset at an angle, making interpretation of the dipole moment orientation and coupling less straightforward. The weighted absorption fit for **RuC** is shown in Figure 2-7b.

2.5.6 Raman Profiles Calculated Fit

Typically, resonance Raman profiles are expected to follow the general contour of the absorption spectrum. However, as seen in Figure 2-3, this is not always the case. **RuT** experimental profiles show only one band as expected; on the other hand, **RuC** profiles match the lower energy band but at the higher energy band wavenumbers, Raman intensity is significantly missing for all of the intense modes.

This discrepancy is a result of the difference in orientational averaging between absorption spectroscopy and Raman spectroscopy.[6,36] In absorption spectroscopy, the total absorption spectrum is a simple weighted sum of the parallel and antiparallel components. This is because absorption intensity is directly proportional to the square of the dipoles, whereas resonance Raman intensity is proportional to the square of the polarizability tensor, α, as shown in Equation 8. Another aspect in which Raman spectroscopy is different, is that Raman scattering is a two photon process instead of the one photon process of absorption. Angle averaging for absorption only includes orientation of the dipoles with respect to the incident light polarization ($\vec{e}_I$), whereas both the incident light and scattered light polarization ($\vec{e}_s$) vectors must be considered for Raman scattering. We can simplify calculations by including only one incident light polarization when the excitation source is a laser beam, but for a randomly oriented sample, scattered light polarization can occur in x, y and z directions and all three must be considered in

the calculations. These differences between the two spectroscopies result in the much more complicated equation shown in Equation 14.

In particular, $\vec{\mu}_i$ and $\vec{\mu}_j$ have the same sign when they are parallel (dipole orientation angle 0^o), and opposite signs when they are antiparallel (180^o), therefore intensities are proportional as such:

$$\begin{cases} I_0 \propto (|\alpha_{11}|^2 + |\alpha_{12}|^2) + (\alpha_{11}^* \alpha_{12} + \alpha_{12}^* \alpha_{11}) \\ I_{180} \propto (|\alpha_{11}|^2 + |\alpha_{12}|^2) - (\alpha_{11}^* \alpha_{12} + \alpha_{12}^* \alpha_{11}) \end{cases} \tag{16}$$

For any angle β, the intensity will be a superposition of the parallel and antiparallel intensity components:

$$I_\beta = aI_0 + bI_{180} = (a+b)(|\alpha_{11}|^2 + |\alpha_{12}|^2) + (a-b)(\alpha_{11}^* \alpha_{12} + \alpha_{12}^* \alpha_{11}) \tag{17}$$

Comparing to Equation 14, *a* and *b* can be solved to give an operational equation that can be used to calculate Raman spectra for any angle β as a weighted sum of the parallel and antiparallel spectra:

$$I_\beta = \left(1 + \frac{1}{2}\cos 2\beta + 2\cos\beta\right) I_0 + \left(1 + \frac{1}{2}\cos 2\beta - 2\cos\beta\right) I_{180} \tag{18}$$

With this equation, we can calculate the resonance Raman profiles and these are shown in Figure 2-9 for the most intense mode for **RuT** and **RuC**. The same β angle as used in absorption calculations is utilized here. The calculated Raman profiles correctly illustrate the missing higher energy band in **RuC**.

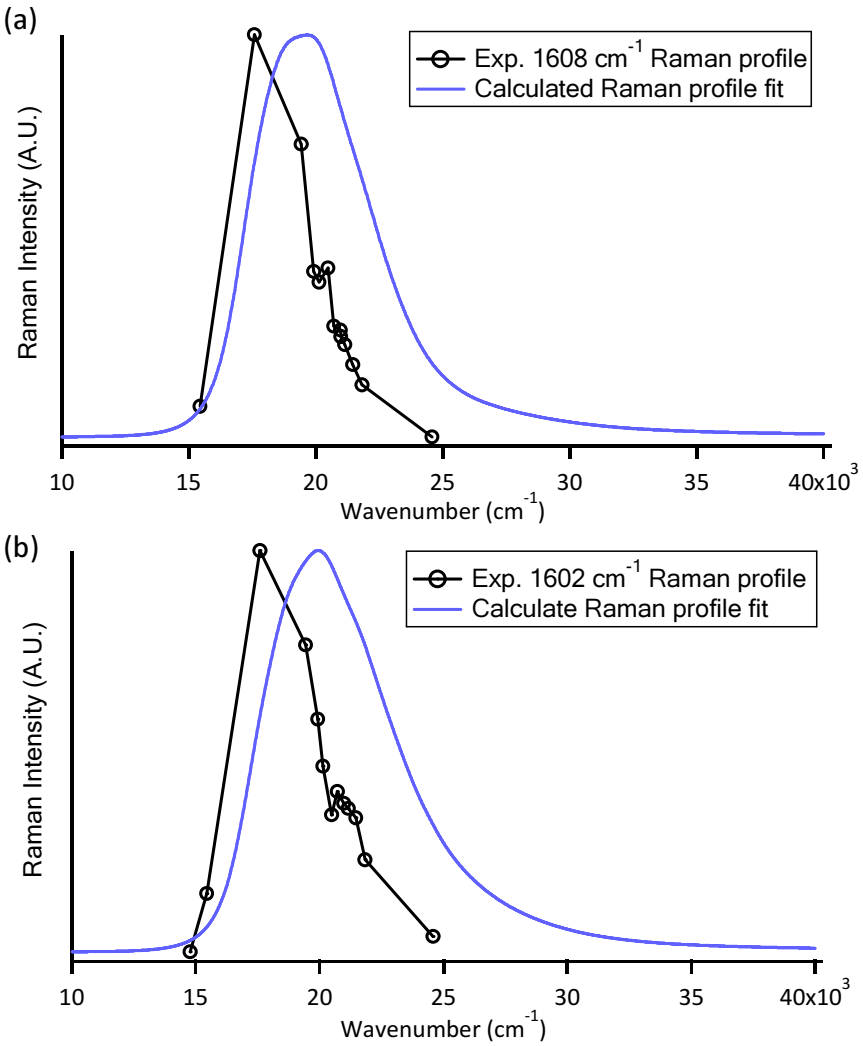

Figure 2-9. Experimental Raman profiles with calculated Raman profile fits of the most intense mode for (a) **RuT** (b) **RuC**

2.6 SUMMARY

Absorption spectra of ruthenium (II) complexes **RuT** and **RuC** display two absorption bands characteristic of excited state mixed valence, whereas the mono ligand **RuM** contains only one electronic transition. Due to the difference in orientation between the two charge bearing

4-acetylpyridine ligands, the ratio in intensity of the two ESMV bands for **RuT** and **RuC** are drastically different.

Construction of neighboring orbital models for the two complexes demonstrate that the in-phase combination of ligand π orbitals (LUMO) is lower in energy than the out-of-phase combination (LUMO+1), thus the coupling is determined to be negative. Examination of group theory explains the selection rules involved for each transition: only the lower energy transition is allowed for **RuT**, while both transitions are allowed for **RuC**.

Raman spectra in resonance with the ESMV bands provide distortion information of the vibrational modes. The most intense modes are typical of vibrational modes of the 4-acetylpyridine ligand, corresponding to the changes in electron density across the ligand during the transition. This information allows a calculated fit of the absorption spectra of **RuT** and **RuC**, which, combined with dipole orientational averaging, give good fits that display the differences between the two spectra.

Resonance Raman profiles of **RuC** do not follow the general contour of the absorption spectrum. This phenomenon can be explained by the inherent difference in orientational averaging between absorption spectroscopy and Raman spectroscopy. The formulae are derived and utilized to calculate a good fit and explain the lack of Raman intensity in the higher energy band region.

2.7 REFERENCES

(1) Brunschwig, B. S.; Creutz, C.; Sutin, N. *Chem. Soc. Rev.* **2002**, *31*, 168.

(2) Day, P.; Hush, N. S.; Clark, R. J. H. *Phil. Trans. R. Soc. A* **2008**, *366*, 5.

(3) Hush, N. S. *Prog. Inorg. Chem.* **1967**, *8*, 391.

(4) Heller, E. J. *Acc. Chem. Res.* **1981**, *14*, 368.

(5) Lee, S.-Y.; Heller, E. J. *J. Chem. Phys.* **1979**, *71*, 4777.

(6) Heather, R.; Metiu, H. *J. Chem. Phys.* **1989**, *90*, 6903.

(7) Tannor, D. J.; Heller, E. J. *J. Chem. Phys.* **1982**, *77*, 202.

(8) Heller, E. J.; Sundberg, R. L.; Tannor, D. J. *J. Phys. Chem.* **1982**, *86*, 1822.

(9) Shin, K.-S. K.; Zink, J. I. *Inorg. Chem.* **1989**, *28*, 4358.

(10) Zink, J. I.; Shin, K.-S. K. In *Advances in Photochemistry*; Wiley: New York; Vol. 16, pp. 119–214.

(11) Simoni, E.; Reber, C.; Talaga, D. S.; Zink, J. I. *J. Phys. Chem.* **1993**, *97*, 12678.

(12) Wexler, D.; Zink, J. I.; Reber, C. In *Electronic and Vibronic Spectra of Transition Metal Complexes I*; Yersin, H., Ed.; Berlin, Heidelberg: Springer-Verlag, 1994; Vol. 171, pp. 173–203.

(13) Myers, A. B. *Chem. Rev.* **1996**, *96*, 911.

(14) Reber, C.; Zink, J. I. *Comments Inorg. Chem.* **1992**, *13*, 177.

(15) Myers, A. B. *Laser Techinques in Chemistry*; Wiley: New York, 1995; Vol. 23, p. 325.

(16) Plummer, E. A.; Zink, J. I. *Inorg. Chem.* **2006**, *45*, 6556.

(17) Zwickel, A. M.; Creutz, C. *Inorg. Chem.* **1971**, *10*, 2395.

(18) Malouf, G.; Ford, P. C. *J. Am. Chem. Soc.* **1977**, *99*, 7213.

(19) Ford, P. C.; Rudd, D. F. P.; Gaunder, R.; Taube, H. *J. Am. Chem. Soc.* **1968**, *90*, 1187.

(20) Bento, M. L.; Tfouni, E. *Inorg. Chem.* **1988**, *27*, 3410.

(21) Vogt, L. H.; Katz, J. L.; Wiberley, S. E. *Inorg. Chem.* **1965**, *4*, 1157.

(22) Isied, S. S.; Taube, H. *Inorg. Chem.* **1974**, *13*, 1545.

(23) Isied, S. S.; Taube, H. *Inorg. Chem.* **1976**, *15*, 3070.

(24) Tfouni, E.; Ford, P. C. *Inorg. Chem.* **1980**, *19*, 72.

(25) Pavanin, L. A.; da Rocha, Z. N.; Giesbrecht, E.; Tfouni, E. *Inorg. Chem.* **1991**, *30*, 2185.

(26) Frisch, M. J.; Trucks, G. W.; Schlegel, H. B.; Scuseria, G. E.; Robb, M. A.; Cheeseman, J. R.; Scalmani, G.; Barone, V.; Mennucci, B.; Petersson, G. A.; Nakatsuji, H.; Caricato, M.; Li, X.; Hratchian, H. P.; Izmaylov, A. F.; Bloino, J.; Zheng, G.; Sonnenb, D. J. Gaussian 09, 2009.

(27) Talaga, D. S.; Zink, J. I. *J. Phys. Chem.* **1996**, *100*, 8712.

(28) Lockard, J. V.; Zink, J. I.; Trieber II, D. A.; Konradsson, A. E.; Weaver, M. N.; Nelsen, S. F. *J. Phys. Chem. A* **2005**, *109*, 1205.

(29) Nelsen, S. F.; Weaver, M. N.; Luo, Y.; Lockard, J. V.; Zink, J. I. *Chem. Phys.* **2006**, *324*, 195.

(30) Lockard, J. V.; Zink, J. I.; Konradsson, A. E.; Weaver, M. N.; Nelsen, S. F. *J. Am. Chem. Soc.* **2003**, *125*, 13471.

(31) Lockard, J. V.; Zink, J. I.; Luo, Y.; Weaver, M. N.; Konradsson, A. E.; Fowble, J. W.; Nelsen, S. F. *J. Am. Chem. Soc.* **2006**, *128*, 16524.

(32) Chung, Y. C.; Leventis, N.; Wagner, P. J.; Leroi, G. E. *J. Am. Chem. Soc.* **1985**, *107*, 1414.

(33) Fuerholz, U.; Joss, S.; Buergi, H. B.; Ludi, A. *Inorg. Chem.* **1985**, *24*, 943.

(34) Tang, J.; Albrecht, A. C. In *Raman Spectroscopy*; Szynanski, H., Ed.; Plenum Press: New York, 1970; Vol. 2, pp. 33–68.

(35) Warshel, A.; Dauber, P. *J. Chem. Phys.* **1977**, *66*, 5477.

(36) Lockard, J. V.; Valverde, G.; Neuhauser, D.; Zink, J. I.; Luo, Y.; Weaver, M. N.; Nelsen, S. F. *J. Phys. Chem. A* **2006**, *110*, 57.

Chapter 3

Theoretical Study on Expanding the Three-State Model:

Coupling, Transition Dipole Moments and Selection Rules

3.1 INTRODUCTION

Mixed valence may occur in molecules with two or more sites that can exist in more than one oxidation state. With electronic communication between the sites, instead of individual potentials where the charge is trapped in one location, coupling can occur and result in adiabatic (mixed valence) states. This gives rise to an intervalence transition that can be observed in electronic absorption spectra.[1-3]

When this occurs in the excited state, two or more charge transfer transitions can interact and excited state mixed valence (ESMV) takes place. This is often represented by M-B^+-M, the ground state that has a symmetric charge distribution, and coupling between M^+-B-M and M-B-M^+, the two excited states with charge localized on either charge bearing site. As in ground state mixed valence (GSMV), the two excited state potentials can couple in the presence of electronic communication, forming two adiabatic excited states. Transition can occur from the ground state to either of these adiabatic states, so two ESMV bands may be observed in an absorption spectrum.

However, more intricacies are involved in an ESMV system. Selection rules must be considered and may result in only one band being allowed and easily observable, while the other is electric dipole forbidden and weak in intensity. These selection rules can be understood by analyzing the nature of the coupling through construction of neighboring orbital models,[4,5] and by considering the relationship between the transition dipole moments to the two diabatic excited states.[6] Such analysis has typically been achieved in past literature through a three state model that establishes dipole selection rules.[5,6,7] However, during the studies of a ruthenium metal complex[8] and a diisopropyl ditolylhydrazine cation, both which exhibit ESMV, this model has been found to

have its limitations. In this chapter, we discuss what these limitations are, and present two expanded models for the two systems that derive selection rules that corroborate with experimental results and group theory.

3.2 THREE STATE MODEL

Here, we look at the three state model for an ESMV system with two equivalent excited states that can couple. The dipole selection rules in the adiabatic basis can be derived by starting in the diabatic basis and going through the adiabatic transformation. In the diabatic basis, the wave functions can be represented by the matrix

$$\psi_{diabat} = \begin{pmatrix} 1 & \psi_G & \psi_L & \psi_R \\ \psi_G & 0 & 0 & 0 \\ \psi_L & 0 & 0 & 0 \\ \psi_R & 0 & 0 & 0 \end{pmatrix} \tag{17}$$

where ψ_G is the ground state wave function, and ψ_L and ψ_R are the wave functions on the excited states of the left and right charge bearing sites. The diabats are allowed to couple by diagonalizing this matrix with the unitary transformation matrix

$$U^{-1} = \begin{pmatrix} 1 & 0 & 0 & 0 \\ 0 & 1 & 0 & 0 \\ 0 & 0 & \cos\theta & \sin\theta \\ 0 & 0 & -\sin\theta & \cos\theta \end{pmatrix} \tag{18}$$

where

$$\tan 2\theta = \frac{2H_{AB}}{V_1(Q) - V_2(Q)} \tag{19}$$

This unitary transformation matrix effectively couples or mixes the two excited states, and H_{AB} is its coupling constant while V_1 and V_2 represent the potential energies of the two states along the coordinate Q (Figure 3-1).

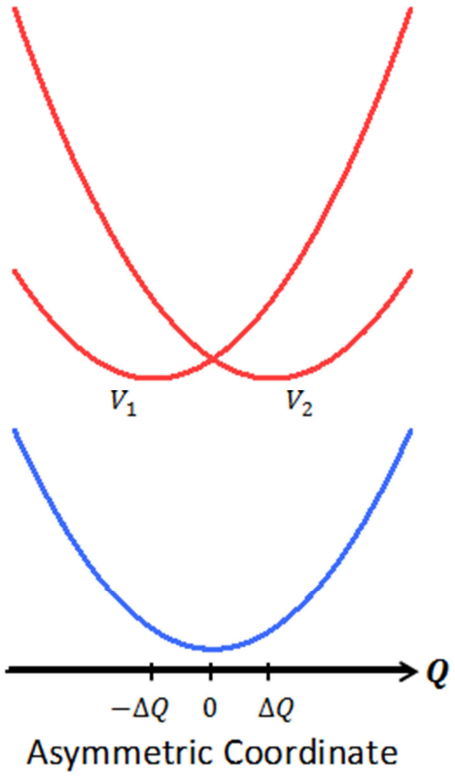

Figure 3-1. Diabatic potential energy curves V_1 and V_2 shown along the asymmetric coordinate Q.

After transformation to the adiabatic basis set with the equation $\psi_{adiabat} = U^{-1} \cdot \psi_{diabat} \cdot U$, the matrix representation of the wave functions is

$$\psi_{adiabat} = \begin{pmatrix} 1 & \psi_G & \psi_L \cos\theta + \psi_R \sin\theta & \psi_R \cos\theta - \psi_L \sin\theta \\ \psi_G & 0 & 0 & 0 \\ \psi_L \cos\theta + \psi_R \sin\theta & 0 & 0 & 0 \\ \psi_R \cos\theta - \psi_L \sin\theta & 0 & 0 & 0 \end{pmatrix} \quad (20)$$

The adiabatic wave functions can be seen to be in-phase and out-of-phase combinations of the diabatic wave functions. The degree of the coupling will depend on the coupling magnitude and the displacement of the excited state potentials. Examination of the transformation of diabatic dipoles will reveal their selection rules in the adiabatic basis. We can focus on the bottom right 3x3 block of the matrices for discussion of the dipoles, as it is block diagonalized and does not mix with the rest of the matrix. This notation is also more consistent with the notations used in past literature. The diabatic dipole matrix is

$$\mu_{diabat} = \begin{pmatrix} 0 & \pm\mu_1 & \mu_2 \\ \pm\mu_1 & 0 & 0 \\ \mu_2 & 0 & 0 \end{pmatrix} \tag{21}$$

where μ_1 and μ_2 are the transition dipole to either of the diabats for the charge bearing sites, while the signs depend on their relative orientation. When the two charge bearing sites are in the same direction, the two dipoles will be parallel and the sign is positive. When they are on opposite sides of the bridge, the dipoles are antiparallel and the sign is negative (opposite signs). Using the same unitary transformation matrix, the adiabatic dipole is

$$\mu_{adiabat} = \begin{pmatrix} 0 & \pm\mu_1\cos\theta + \mu_2\sin\theta & \mp\mu_1\sin\theta + \mu_2\cos\theta \\ \pm\mu_1\cos\theta + \mu_2\sin\theta & 0 & 0 \\ \mp\mu_1\sin\theta + \mu_2\cos\theta & 0 & 0 \end{pmatrix} \tag{22}$$

The transition dipole to the in-phase combination of the diabatic wave functions in the adiabatic basis, Ψ^+, is $\pm\mu_1\cos\theta + \mu_2\sin\theta$, and to the out-of-phase combination wave function, Ψ^-, it is $\mp\mu_1\sin\theta + \mu_2\cos\theta$. When the transition dipoles are parallel, transition to Ψ^+ has dipole of $\mu_1\cos\theta + \mu_2\sin\theta$, which is non-zero everywhere along the Q coordinate. On the other hand, the transition to Ψ^- has dipole of $-\mu_1\sin\theta + \mu_2\cos\theta$, which is zero at Q = 0, positive when Q > 0

and negative when Q < 0. This can be understood by examining the angle θ, earlier defined in Equation 3. At Q = 0, V_1 and V_2 are at the same energy and $V_1(Q) - V_2(Q) = 0$, therefore, $\tan 2\theta \rightarrow \infty$, and $\cos\theta \approx \sin\theta$. This means that a transition from the ground state to Ψ^+ is electric dipole allowed (in the adiabatic limit where $H_{AB} \gg V_1(Q) - V_2(Q)$), whereas transition to Ψ^- is dipole forbidden, but vibronically allowed as the wave function along the coordinate Q away from Q = 0.

The effect of parallel versus antiparallel transition dipoles on the function of the transition dipole to either the Ψ^+ or Ψ^- adiabatic states, its value along the coordinate Q, and the ensuing selection rule for that transition is summarized in Table 3-1.

	Transition to state	Dipole	Dipole value along Q	Selection rule
Parallel	Ψ^+	$\mu_1\cos\theta + \mu_2\sin\theta$	non-zero everywhere	Electric dipole allowed*
	Ψ^-	$-\mu_1\sin\theta + \mu_2\cos\theta$	zero at Q = 0 positive when Q > 0 negative when Q < 0	Dipole forbidden, but vibronically allowed
Antiparallel	Ψ^+	$-\mu_1\cos\theta + \mu_2\sin\theta$	zero at Q = 0 negative when Q > 0 positive when Q < 0	Dipole forbidden, but vibronically allowed
	Ψ^-	$\mu_1\sin\theta + \mu_2\cos\theta$	non-zero everywhere	Electric dipole allowed*

Table 3-1. Summary of dipole selection rules for parallel and antiparallel dipoles. * In the adiabatic limit where $H_{AB} \gg V_1(Q) - V_2(Q)$.

3.3 RUTHENIUM METAL COMPLEXES

In the previous chapter, a set of ruthenium metal complexes were investigated for their excited state mixed valence (ESMV) properties.[9-12] *Trans*-di-(4-acetylpyridine)-tetraammineruthenium (II)

(**RuT**, Scheme 3-1) hexafluorophosphate and its analogous *cis* complex (**RuC**) contain two equivalent ligands that can participate in metal to ligand charge transfer (MLCT). With electronic communication mediated through the ruthenium metal center, coupling can occur, and excited state mixed valence is observed for these two complexes. The ESMV is displayed in the absorption spectra, where two transition bands are present, in contrast to the single band observed for the mono ligand complex which does not have ESMV. Due to the difference in relative orientation of their ligands, **RuT** and **RuC** demonstrate different selection rules, evident in the difference in intensity ratio of the two ESMV bands. These selection rules and an expanded model to establish them is the focus of this section. For the purpose of developing the model, we will focus on solely the trans complex **RuT**.

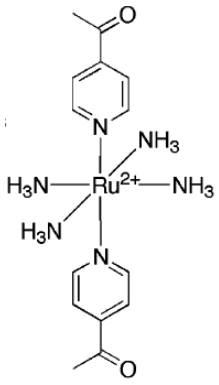

Scheme 3-1. Molecular structure of the trans ruthenium complex **RuT**.

3.3.1 Neighboring Orbital Model (NOM)

Construction of the neighboring orbital model for **RuT** was discussed in the previous chapter, and is shown in Figure 3-2. Inspection of the LUMO and LUMO+1, which involve metal-mediated coupling between the ligand π_{2a} and π_{2b} orbitals, reveal that the in-phase combination

of said orbitals is lower in energy, while the out-of-phase combination is higher in energy. Thus, the sign of the coupling is determined to be negative.

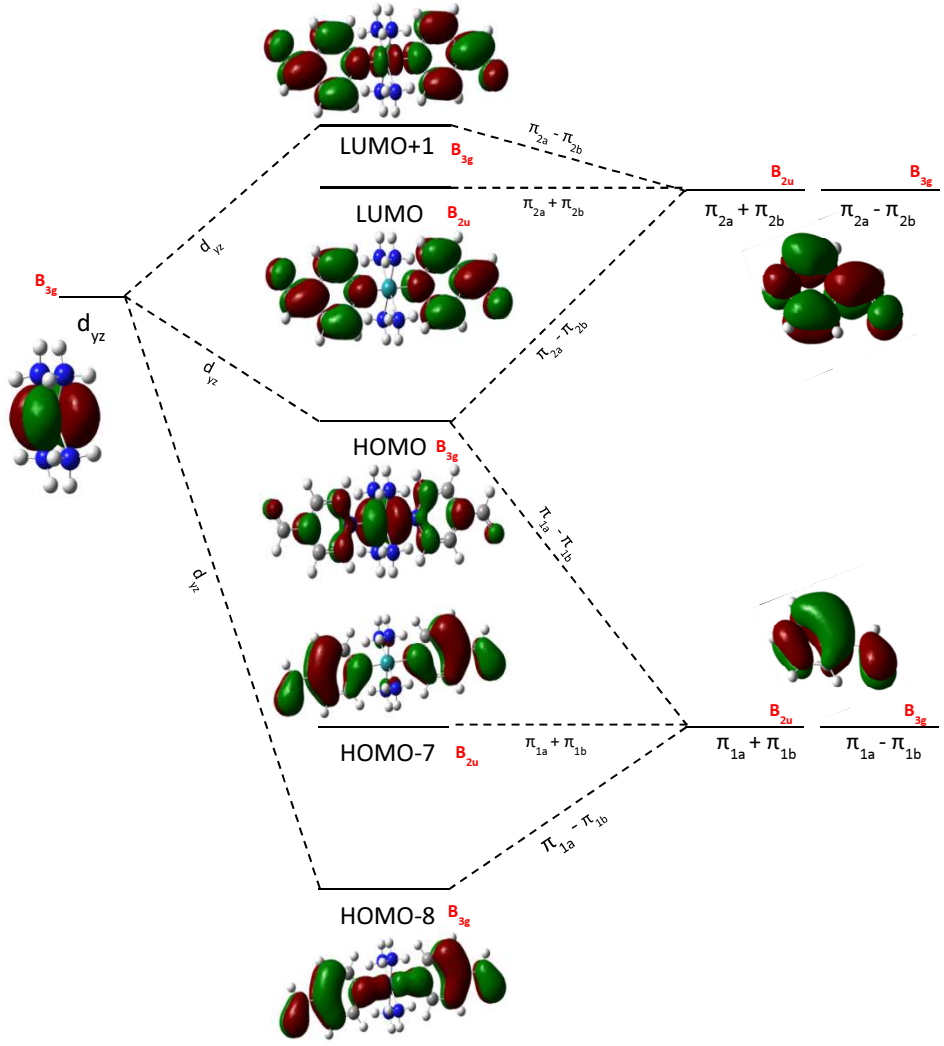

Figure 3-2. Neighboring orbital model for **RuT**. Symmetry assigned in D_{2h} point group.

The experimental absorption spectrum obtained for **RuT** is shown in Figure 3-3. The feature of importance in our discussion here is the small shoulder at around 22000 cm^{-1}. This shoulder, along with the prominent absorption band at 18754 cm^{-1}, are the two ESMV bands, albeit with far different intensities due to selection rules.

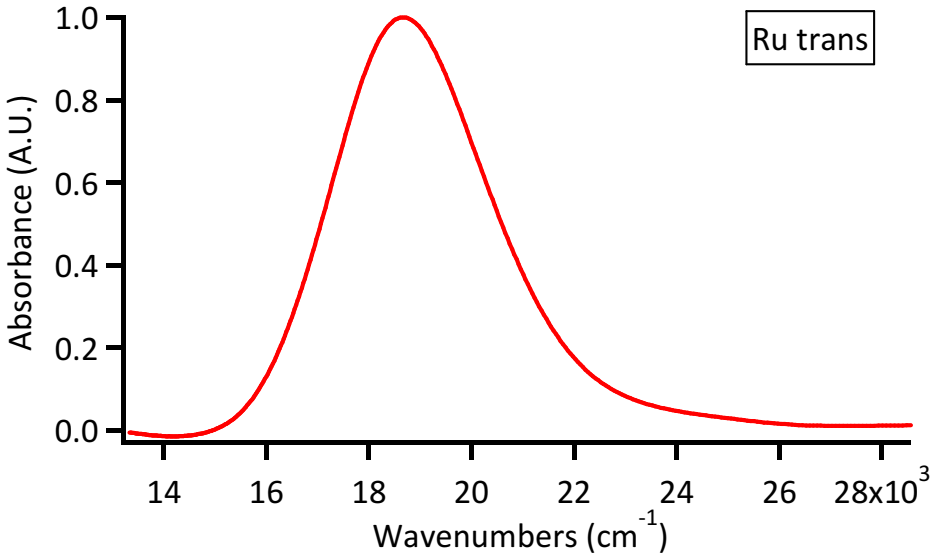

Figure 3-3. Absorption spectrum of **RuT** in acetonitrile.

From a group theory and quantum mechanics perspective, the selection rules are straightforward and can be easily deduced. For a transition to be allowed, the transition dipole moment integral

$$\int \psi_1^* \hat{\mu} \psi_2 d\tau \tag{23}$$

has to be non-zero. ψ_1 and ψ_2 are the wave functions of the two states involved, and $\hat{\mu}$ is the electric dipole operator, which in absorption spectroscopy, is the electric dipole vector of the excitation light. Only the symmetry of the integral needs to be evaluated to determine the selection rules: if the overall function contains the totally symmetric irreducible representation, then the integral will be non-zero and the transition allowed.

Considering the **RuT** complex in a D_{2h} point group, the HOMO and LUMO+1 are of B_{3g} symmetry, while the LUMO is of B_{2u} symmetry. The electric dipole vector of the excitation light

transforms as x, y and z, which correspond to B_{3u}, B_{2u} and B_{1u} respectively under the D_{2h} point group. The symmetry product of a HOMO to LUMO transition is $B_{3g} \otimes B_{2u} = B_{1u}$. For the overall transition moment integral to be non-zero, there needs to be an electric dipole vector that matches B_{1u} symmetry for the integral to be totally symmetric. The z component vector fulfills this criterion, and the HOMO → LUMO transition is allowed. For the HOMO to LUMO+1 transition, the symmetry is $B_{3g} \otimes B_{3g} = A_g$, and as there are no electric dipole components with this same symmetry, the transition moment integral is zero and the transition is forbidden. This analysis correctly interprets bands observed in the experimental absorption spectrum, where the lower energy band is allowed and the higher energy band is forbidden, resulting in only a small shoulder.

The same selection rules should result from an analysis of the transition dipole moment. As earlier derived, the three state model for antiparallel dipoles should result in a dipole forbidden (but vibronically allowed) transition to the in-phase adiabatic state, and an allowed transition to the out-of-phase state (Table 3-1). Through construction of the NOM, it was determined that the coupling is negative and that the in-phase ligand orbitals combination is lower in energy. Therefore, the transition to the lower energy should be forbidden whereas the higher energy transition should be allowed. This is obviously contrary to observations and group theory derived selection rules.

In this study, this discrepancy was found to be due to a hidden assumption that in prior studies had been a correct assumption for the systems in past studies, and therefore did not have much significance. The assumption is that the ground state from which the transition begins is completely symmetrical. This assumption is evident in the matrices set-up for the diabatic

coupling derivations. Coupling is applied to the two diabatic states ψ_L and ψ_R, but the ground state is represented as a single ψ_G which, in the rest of the coupling derivations, does not play a role of any sort and is not considered, resulting in the inherent assumption that this state is totally symmetric. Examination of the Gaussian calculated ground state molecular orbital HOMO, reveals that it is asymmetric, with its out-out-phase ligand orbital combinations and metal centered d orbital.

Here, we develop an expanded model more suited to this system, and that correctly derives selection rules that match the group theory derived and experimental observations. In the last section, we will look at another example of such a system with an asymmetric ground state.

3.3.2 Expanded Model for Asymmetric Ground State

We start with the diabatic basis set, with the diabatic matrix representing the five orbitals that couple to form the HOMO, LUMO and LUMO+1 (and two other molecular orbitals at lower energies). ψ_{LT} and ψ_{RT} represent the wave functions of the left and right higher energy ligand orbitals π_{2a} and π_{2b}, ψ_{LB} and ψ_{RB} represent the wave functions of the left and right lower energy ligand orbitals π_{1a} and π_{1b}, and ψ_D represents the ruthenium metal center d_{yz} orbital. The wave functions matrix representation is thus

$$\psi_{diabat} = \begin{pmatrix} 1 & \psi_{LT} & \psi_{RT} & \psi_D & \psi_{LB} & \psi_{RB} \\ \psi_{LT} & 0 & 0 & 0 & 0 & 0 \\ \psi_{RT} & 0 & 0 & 0 & 0 & 0 \\ \psi_D & 0 & 0 & 0 & 0 & 0 \\ \psi_{LB} & 0 & 0 & 0 & 0 & 0 \\ \psi_{RB} & 0 & 0 & 0 & 0 & 0 \end{pmatrix} \quad (24)$$

The transition dipole operator is written as

$$\hat{\mu}_{diabat} = \begin{pmatrix} 1 & 0 & 0 & 0 & 0 & 0 \\ 0 & 0 & 0 & \mu_T & 0 & \mu_B \\ 0 & 0 & 0 & -\mu_T & -\mu_B & 0 \\ 0 & \mu_T & -\mu_T & 0 & 0 & 0 \\ 0 & 0 & -\mu_B & 0 & 0 & 0 \\ 0 & \mu_B & 0 & 0 & 0 & 0 \end{pmatrix} \quad (25)$$

where the transition dipole from the metal d_{yz} orbital to the left π ligand ψ_{LT} is μ_T, to the right ligand is the same magnitude but negative, and the dipole from ψ_{LB} to ψ_{RT} is μ_B, while the other direction is negative but the same magnitude.

As the diabats are allowed to couple to form adiabats, the mathematical equivalence of the adiabatic transformation is the equation $\hat{\mu}_{adiabat} = U^{-1} \cdot \hat{\mu}_{diabat} \cdot U$, where U is the unitary transformation matrix. Here, we break this transformation up into two simpler steps, the first in which each pair of π_{1a} and π_{1b} and π_{2a} and π_{2b} forms linear combinations.

$$U_1^{-1} = \begin{pmatrix} 1 & 0 & 0 & 0 & 0 & 0 \\ 0 & \frac{1}{\sqrt{2}} & -\frac{1}{\sqrt{2}} & 0 & 0 & 0 \\ 0 & \frac{1}{\sqrt{2}} & \frac{1}{\sqrt{2}} & 0 & 0 & 0 \\ 0 & 0 & 0 & 1 & 0 & 0 \\ 0 & 0 & 0 & 0 & \frac{1}{\sqrt{2}} & \frac{1}{\sqrt{2}} \\ 0 & 0 & 0 & 0 & -\frac{1}{\sqrt{2}} & \frac{1}{\sqrt{2}} \end{pmatrix} \quad (26)$$

After this first transformation, the mixed orbitals are now

$$\psi_{mix} = \begin{pmatrix} 1 & \psi_{LT} - \psi_{RT} & \psi_{LT} + \psi_{RT} & \psi_D & \psi_{LB} + \psi_{RB} & \psi_{LB} - \psi_{RB} \\ \psi_{LT} - \psi_{RT} & 0 & 0 & 0 & 0 & 0 \\ \psi_{LT} + \psi_{RT} & 0 & 0 & 0 & 0 & 0 \\ \psi_D & 0 & 0 & 0 & 0 & 0 \\ \psi_{LB} + \psi_{RB} & 0 & 0 & 0 & 0 & 0 \\ \psi_{LB} - \psi_{RB} & 0 & 0 & 0 & 0 & 0 \end{pmatrix} \quad (27)$$

This represents the in-phase and out-of-phase combinations of the two sets of π ligand orbitals, while the d orbital remains unchanged. The next step of unitary transformation can then be performed with the second unitary transformation matrix

$$U_2^{-1} = \begin{pmatrix} 1 & 0 & 0 & 0 & 0 & 0 \\ 0 & \cos\theta & 0 & \sin\theta & 0 & 0 \\ 0 & 0 & 1 & 0 & 0 & 0 \\ 0 & -\sin\theta & 0 & \cos\theta \cdot \cos\phi & 0 & \sin\phi \\ 0 & 0 & 0 & 0 & 1 & 0 \\ 0 & 0 & 0 & -\sin\phi & 0 & \cos\phi \end{pmatrix} \quad (28)$$

which allows mixing between the two sets of out-of-phase linear combinations of the ligand π orbitals with the d_{yz} orbital. These are the three sets of orbitals that have the same symmetry and can interact. The magnitude of coupling is represented by this matrix by the equations $\tan 2\theta = \frac{2H_T}{V_D - V_T}$ and $\tan 2\phi = \frac{2H_B}{V_D - V_B}$, where V_D, V_T and V_B are the potential energy curves for ψ_D, $(\psi_{LT} - \psi_{RT})$ and $(\psi_{LB} - \psi_{RB})$ respectively, H_T is the coupling constant between ψ_D and $(\psi_{LT} - \psi_{RT})$, and H_B is the coupling constant between ψ_D and $(\psi_{LB} - \psi_{RB})$.

After the full unitary transformation of $\hat{\mu}_{adiabat} = U_2^{-1} \cdot U_1^{-1} \cdot \hat{\mu}_{diabat} \cdot U_1 \cdot U_2$, the adiabatic matrix representation is

$$\psi_{adiabat} = \begin{pmatrix} 1 & \psi_{LUMO+1} & \psi_{LUMO} & \psi_{HOMO} & \psi_{HOMO-7} & \psi_{HOMO-8} \\ \psi_{LUMO+1} & 0 & 0 & 0 & 0 & 0 \\ \psi_{LUMO} & 0 & 0 & 0 & 0 & 0 \\ \psi_{HOMO} & 0 & 0 & 0 & 0 & 0 \\ \psi_{HOMO-7} & 0 & 0 & 0 & 0 & 0 \\ \psi_{HOMO-8} & 0 & 0 & 0 & 0 & 0 \end{pmatrix} \quad (29)$$

where

$$\psi_{LUMO+1} = \frac{\psi_{LT}\cos\theta}{\sqrt{2}} - \frac{\psi_{RT}\cos\theta}{\sqrt{2}} + \psi_D \sin\theta \quad (30)$$

$$\psi_{LUMO} = \frac{\psi_{LT}}{\sqrt{2}} + \frac{\psi_{RT}}{\sqrt{2}} \quad (31)$$

$$\psi_{HOMO} = \psi_D \cos\theta\cos\phi - \frac{\psi_{LT}\sin\theta}{\sqrt{2}} + \frac{\psi_{RT}\sin\theta}{\sqrt{2}} - \frac{\psi_{LB}\sin\theta}{\sqrt{2}} + \frac{\psi_{RB}\sin\theta}{\sqrt{2}} \quad (32)$$

$$\psi_{HOMO-7} = \frac{\psi_{LB}}{\sqrt{2}} + \frac{\psi_{RB}}{\sqrt{2}} \quad (33)$$

$$\psi_{HOMO-8} = -\frac{\psi_{LB}\cos\phi}{\sqrt{2}} + \frac{\psi_{RB}\cos\phi}{\sqrt{2}} - \psi_D \sin\phi \quad (34)$$

Comparison of these adiabatic wave functions with the Gaussian calculated molecular orbitals shown in Figure 3-2 show that they accurately represent the five MOs that result from coupling. The dipole matrix that results from this same adiabatic transformation is a complicated matrix, but the elements of importance for our discussion are the two dipoles corresponding to the transitions of HOMO → LUMO (μ_{lower}) and HOMO → LUMO+1 (μ_{higher}):

$$\mu_{\text{lower}} = \alpha \sin\phi \tag{35}$$

$$\mu_{\text{higher}} = \sqrt{2}(\cos^2\theta \cos\phi - \sin^2\theta)\mu_T \tag{36}$$

Considering the equation $\tan 2\theta = \frac{2H_T}{V_D - V_T}$, at equilibrium position, V_D and V_T are similar in energy, therefore $V_D - V_T$ is small, $\tan 2\theta \to \infty$, $\theta \to 45°$ and $\cos\theta \approx \sin\theta$. For $\tan 2\phi = \frac{2H_B}{V_D - V_B}$, at equilibrium position, V_D and V_B differ greater in energy, $V_D - V_B$ is large, $\tan 2\phi \to 0$, $\phi \to 0$, and $\cos\phi \to 1$. With these relations, at equilibrium position, $\mu_{\text{lower}} \neq 0$ and is an allowed transition, but $\mu_{\text{higher}} \to 0$ and is dipole forbidden.

This expanded model now considering the asymmetric ground state correctly interprets the selection rules observed from experimental absorption spectrum and is consistent with group theory.

3.4 DIISOPROPYL DITOLYLHYDRAZINE

This project was in collaboration with fellow group member Dr. Matthew Kiesz. This study of the 1,2-ditolyl-1,2-diisopropyl hydrazine radical cation (**DHy**$^+$, Scheme 3-2) present a second example of a system with asymmetric ground state that is not suitable for using the original three state model for examining dipole selection rules.

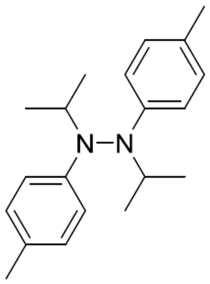

Scheme 3-2. Molecular structure of the radical cation **DHy**$^{+}$.

The absorption spectrum of **DHy**$^{+}$ (shown in Figure 3-4) displays two prominent absorption bands with maxima at 14600 cm^{-1} and 19720 cm^{-1}, the lower energy band with vibronic progression. Though not obvious, there is also a weak band at around 17500 cm^{-1}. The presence of this weak band is backed up by comparison to a similar compound in past studies.[7] The strong band at low energy and the weak band around 17500 cm^{-1} compose the ESMV bands this system displays. The strong bands at much higher energy belong to a higher energy transition that is not part of the mixed valence and will not be the focus of this discussion. In the ground state, the positive charge resides across the N-N central bridge. When it is excited, the charge transfers to either one of the tolyl groups, and with electronic communication through the bridge, this forms a coupled mixed valence excited state.

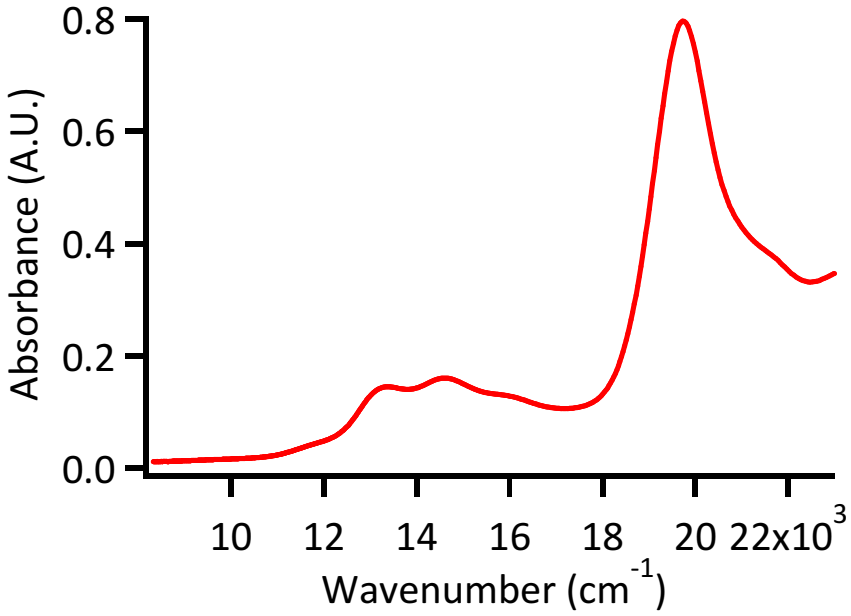

Figure 3-4. Absorption spectrum of **DHy**$^{+}$ in methylenechloride.

3.4.1 Neighboring Orbital Model (NOM)

A neighboring orbital model (NOM) is constructed and shown in Figure 3-5. Molecular orbitals were calculated in Gaussian 09[13] by DFT methods B3LYP/6-31G*. The diabatic orbitals of the phenyl π orbitals and the nitrogen bridge p orbitals are shown on the left and right, respectively. The out-of-phase phenyl π orbitals couple through the out-of-phase nitrogen bridge p orbitals, while the in-phase orbitals interact with the in-phase bridge orbitals. This generates the four adiabatic molecular orbitals shown in the center. In addition, there are two MOs that are from another set of phenyl π orbitals that do not have the correct symmetry and are non-bonding. These are the HOMO-1 and HOMO-2 and are shown in the center as well in the NOM for completeness. A more simplified NOM is shown in Figure 3-6. This simplified model focuses on where the electron density is primarily situated, which inherently neglects mixing between the bridge and phenyl groups. This simplification is justified by the much larger coupling between

the nitrogen atoms compared to the phenyls. The nitrogen atom orbitals couple strongly to produce the adiabatic ψ_N^+ (HOMO-4) and ψ_N^- (SOMO) which are separated by a larger energy difference, while the ψ_P^- (HOMO-3) and ψ_P^+ (HOMO) are predominantly phenyl orbitals.

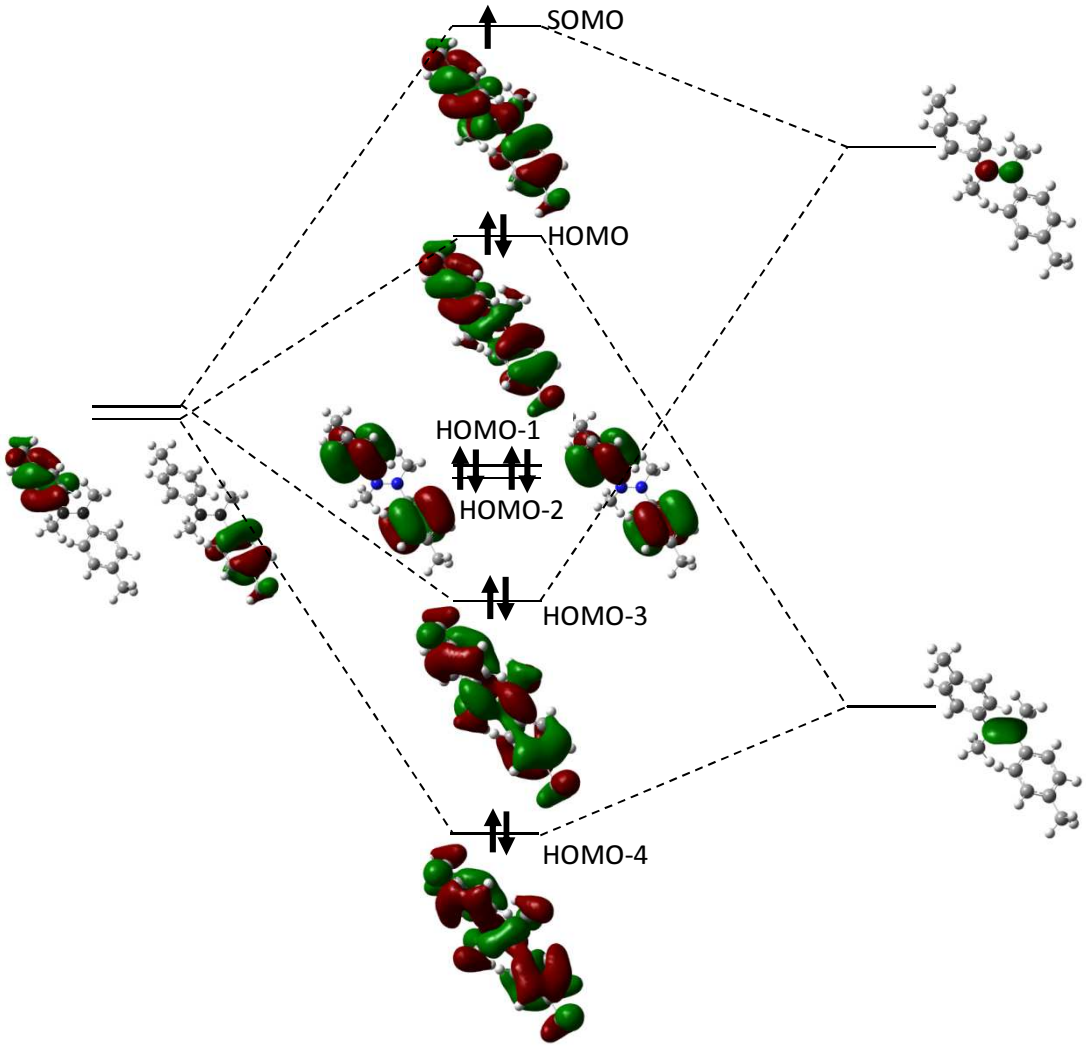

Figure 3-5. Neighboring orbital model for **DHy**$^+$.

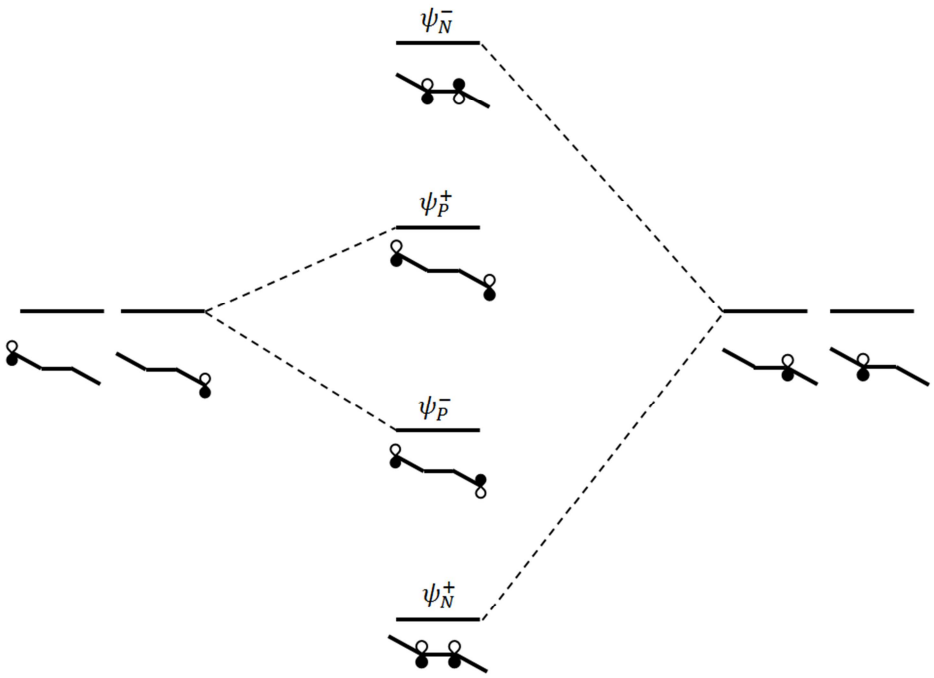

Figure 3-6. Simplified neighboring orbital model for **DHy**$^+$. Phenyl π orbitals and nitrogen bridge p orbitals are all represented by p orbitals for clarity.

Completing the molecular orbitals with the odd number of electrons, the ground state electronic configuration can thus be written as $\Psi_{\text{ground}} = (\psi_{\text{N}}^+)^2(\psi_{\text{P}}^-)^2(\psi_{\text{P}}^+)^2(\psi_{\text{N}}^-)^1$ with the charge residing on the bridge. The lowest energy transition moves the positive charge (hole) to either phenyl, or equivalently, an electron from ψ_{P}^+ to ψ_{N}^-, resulting in the electron configuration $\Psi_{\text{ex1}} = (\psi_{\text{N}}^+)^2(\psi_{\text{P}}^-)^2(\psi_{\text{P}}^+)^1(\psi_{\text{N}}^-)^2$, the lower adiabatic surface of ESMV. The next excited state is represented by the higher adiabatic surface, and has electron configuration of $\Psi_{\text{ex2}} = (\psi_{\text{N}}^+)^2(\psi_{\text{P}}^-)^1(\psi_{\text{P}}^+)^2(\psi_{\text{N}}^-)^2$. According to experimental observations, only the lower energy transition is allowed. From a group theory discussion, when considering **DHy**$^+$ to be C_{2h} (neglecting significant twisting), the ground to first excited state transition is from B_g to A_u, which is an allowed transition, while the higher energy transition is from B_g to B_g and is

forbidden. This corresponds well with experimental absorption spectrum. However, when considering the basic three state model with antiparallel dipoles, transition to the in-phase phenyl orbital combination should be dipole forbidden (the lower energy transition), while transition to the out-of-phase should be allowed (the higher energy transition). This is inconsistent with experimental findings and is again due to the asymmetric nature of the ground state, with the charge residing on the out-of-phase combination of the nitrogen orbitals bridge.

Here, we will develop the expanded model as it pertains to the **DHy**$^+$ system to derive the correct dipole selection rules.

3.4.2 Expanded Model for Asymmetric Ground State

Four states are involved in the coupling in this system. In the diabatic basis set, these are the π orbitals of the two phenyl groups (ψ_{PL} and ψ_{PR} for the left and right groups), and the π orbitals on both nitrogen atoms in the bridge (ψ_{NL} and ψ_{NR} for the left and right nitrogens). The wave functions can be represented by the matrix

$$\psi_{\text{diabat}} = \begin{pmatrix} 1 & \psi_{PL} & \psi_{PR} & \psi_{NL} & \psi_{NR} \\ \psi_{PL} & 0 & 0 & 0 & 0 \\ \psi_{PR} & 0 & 0 & 0 & 0 \\ \psi_{NL} & 0 & 0 & 0 & 0 \\ \psi_{NR} & 0 & 0 & 0 & 0 \end{pmatrix} \tag{37}$$

In the diabatic basis, the transition dipoles can be considered to be μ_a and μ_b for the transition dipole from a nitrogen to the nearest phenyl and to the further phenyl, respectively. The transition dipole matrix can thus be represented by

$$\mu_{\text{diabat}} = \begin{pmatrix} 1 & 0 & 0 & 0 & 0 \\ 0 & 0 & 0 & \mu_a & \mu_b \\ 0 & 0 & 0 & -\mu_b & -\mu_a \\ 0 & \mu_a & -\mu_b & 0 & 0 \\ 0 & \mu_b & -\mu_a & 0 & 0 \end{pmatrix} \tag{38}$$

These matrices can be transformed to the adiabatic basis with the unitary transformation matrix

$$U^{-1} = \begin{pmatrix} 1 & 0 & 0 & 0 & 0 \\ 0 & cos\ \theta & \sin\theta & 0 & 0 \\ 0 & -\sin\theta & \cos\theta & 0 & 0 \\ 0 & 0 & 0 & \cos\phi & \sin\phi \\ 0 & 0 & 0 & -\sin\phi & \cos\phi \end{pmatrix} \tag{39}$$

where $\tan 2\theta = \frac{2H_P}{V_{PL}-V_{PR}}$ and $\tan 2\phi = \frac{2H_N}{V_{NL}-V_{NR}}$, representing the coupling between each set of orbitals. Four adiabatic wave functions are produced after undergoing diagonalization with the unitary transformation matrix:

$$\psi_{\text{diabat}} = \begin{pmatrix} 1 & \psi_P^+ & \psi_P^- & \psi_N^+ & \psi_N^- \\ \psi_P^+ & 0 & 0 & 0 & 0 \\ \psi_P^- & 0 & 0 & 0 & 0 \\ \psi_N^+ & 0 & 0 & 0 & 0 \\ \psi_N^- & 0 & 0 & 0 & 0 \end{pmatrix} \tag{40}$$

where

$$\psi_P^+ = \psi_{PR}\cos\theta + \psi_{PL}\sin\theta \tag{41}$$

$$\psi_P^- = \psi_{PR}\cos\theta - \psi_{PL}\sin\theta \tag{42}$$

$$\psi_N^+ = \psi_{NR}\cos\phi + \psi_{NL}\sin\phi \tag{43}$$

$$\psi_N^- = \psi_{NR}\cos\phi - \psi_{NL}\sin\phi \tag{44}$$

The same adiabatic transformation results in the adiabatic dipoles:

$$\mu_{\psi_N^+ \to \psi_P^+} = \mu_a \cos(\theta + \phi) - \mu_b \sin(\theta - \phi) \quad (45)$$

$$\mu_{\psi_N^+ \to \psi_P^-} = -\mu_b \cos(\theta - \phi) - \mu_a \sin(\theta + \phi) \quad (46)$$

$$\mu_{\psi_N^- \to \psi_P^+} = \mu_b \cos(\theta - \phi) - \mu_a \sin(\theta + \phi) \quad (47)$$

$$\mu_{\psi_N^- \to \psi_P^-} = -\mu_a \cos(\theta + \phi) - \mu_b \sin(\theta - \phi) \quad (48)$$

In our ESMV system, the two transitions in consideration are from ψ_P^+ to ψ_N^- (lower energy band) and from ψ_P^- to ψ_N^- (higher energy band).The transition dipole corresponding to the lower energy transition is $\mu_{\psi_N^- \to \psi_P^+}$. For each set of coupling orbitals, the pair of potential energies are equal at the origin, thus $V_{PL} - V_{PR} = V_{NL} - V_{NR} = 0$, $\tan 2\theta = \tan 2\phi = \infty$, and $\theta = \phi = 45°$. Therefore, $\mu_{\psi_N^- \to \psi_P^+} = \mu_b - \mu_a$ which is non-zero since the two diabatic dipoles are unequal, and this transition is dipole allowed. On the contrary, the higher energy transition has dipole $\mu_{\psi_N^- \to \psi_P^-} = 0$ and is dipole forbidden.

This conclusion is in agreement with the experimentally observed absorption spectrum and with selection rules derived from group theory.

3.5 SUMMARY

The absorption spectra of compounds **RuT** and **DHy**$^+$ show two absorption bands typical of excited state mixed valence. In both systems, the lower energy band is allowed and has strong intensity, while the higher energy band is forbidden and exists only as a weak shoulder. Analysis using group theory with **RuT** in the D_{2h} point group and **DHy**$^+$ in the C_{2h} point group leads to the

same selection rules as that observed in the absorption spectra. However, when utilizing the three state model generally used in past mixed valence studies, the results are in disagreement. This is due to the inherent assumption in this model that the ground state is symmetric. As both **RuT** and $\mathbf{DHy}^{+}$ have molecular orbitals that are asymmetric in the ground state, the simple three state model is not suitable here.

In our studies, we have developed two expanded models for the two systems that take into account the symmetry of the ground state. The ground state molecular orbitals are included in the adiabatic coupling and matrix transformation in the expanded model, thus allowing it to be part of the consideration of the dipole selection rules. Both models were successful in determining selection rules that correspond with those experimentally observed and which can be confirmed via group theory analysis. These models, though not ready to be generalized for all systems with asymmetric ground state and have to be constructed for each individual system, nevertheless demonstrates the importance of considering and including the symmetry of the ground state in the dipole matrices calculation in determining dipole selection rules.

3.6 REFERENCES

(1) Hush, N. S. *Prog. Inorg. Chem.* **1967**, *8*, 391.

(2) Day, P.; Hush, N. S.; Clark, R. J. H. *Phil. Trans. R. Soc. A* **2008**, *366*, 5.

(3) Brunschwig, B. S.; Creutz, C.; Sutin, N. *Chem. Soc. Rev.* **2002**, *31*, 168.

(4) Nelsen, S. F.; Weaver, M. N.; Luo, Y.; Lockard, J. V.; Zink, J. I. *Chem. Phys.* **2006**, *324*, 195.

(5) Lockard, J. V.; Zink, J. I.; Konradsson, A. E.; Weaver, M. N.; Nelsen, S. F. *J. Am. Chem. Soc.* **2003**, *125*, 13471.

(6) Lockard, J. V.; Zink, J. I.; Trieber II, D. A.; Konradsson, A. E.; Weaver, M. N.; Nelsen, S. F. *J. Phys. Chem. A* **2005**, *109*, 1205.

(7) Lockard, J. V.; Zink, J. I.; Luo, Y.; Weaver, M. N.; Konradsson, A. E.; Fowble, J. W.; Nelsen, S. F. *J. Am. Chem. Soc.* **2006**, *128*, 16524.

(8) Plummer, E. A.; Zink, J. I. *Inorg. Chem.* **2006**, *45*, 6556.

(9) Zwickel, A. M.; Creutz, C. *Inorg. Chem.* **1971**, *10*, 2395.

(10) Malouf, G.; Ford, P. C. *J. Am. Chem. Soc.* **1977**, *99*, 7213.

(11) Bento, M. L.; Tfouni, E. *Inorg. Chem.* **1988**, *27*, 3410.

(12) Ford, P. C.; Rudd, D. F. P.; Gaunder, R.; Taube, H. *J. Am. Chem. Soc.* **1968**, *90*, 1187.

(13) Frisch, M. J.; Trucks, G. W.; Schlegel, H. B.; Scuseria, G. E.; Robb, M. A.; Cheeseman, J. R.; Scalmani, G.; Barone, V.; Mennucci, B.; Petersson, G. A.; Nakatsuji, H.; Caricato, M.; Li, X.; Hratchian, H. P.; Izmaylov, A. F.; Bloino, J.; Zheng, G.; Sonnenb, D. J. Gaussian 09, 2009.

Chapter 4

Raman Spectroscopic Study of a Mixed Valence Cyclophane Dication

4.1 INTRODUCTION

Mixed valence occurs in molecules with two or more equal redox centers in different degrees of oxidation.[1,2] These redox centers can have electronic communication and charge can reside on either site resulting in mixed valence. Depending on the extent of the electronic communication, mixed valence can be classified using the Robin-Day classification[3] to be Class I, II or III. Class I mixed valence species have little to no electronic communication, and the charge is localized on one site or the other. Class III systems have strong electronic communication and the charge is delocalized across the sites. Class II systems are intermediate in the magnitude of coupling between the sites.

Electronic communication and coupling can be mediated through direct bonding or via a mediating molecular bridge (through-bond). Here, we investigate a cyclophane compound with a special type of through-space coupling, namely π-stacking between the rings.[4-7] The molecular structure of the compound doubly trimethylene-bridged tetraaza[5,5]-*p*-phenylene diamine paracyclophane dication (**Me3C**$^{2+}$) is shown in Scheme 4-1. The monomeric radical cation tetramethyl-*p*-phenylenediamine (**TMPD**$^{\cdot+}$) of this compound exhibits mixed valence, where the positive charge can reside on either of the two nitrogens. For the dimeric paracyclophane in this study, the diradical charge can reside on one of four nitrogen sites, with coupling mediated through the alkyl bridge, the phenylene bridge, and the proposed π-stacking communication. In resonance Raman spectroscopy, the normal modes that correspond to electronic density changes in an electronic transition are most enhanced, and resonance Raman is a tool often used to study mixed valence systems.[8-11] We therefore use resonance Raman spectroscopy to analyze the cyclophane compound to further understand its mixed valence.

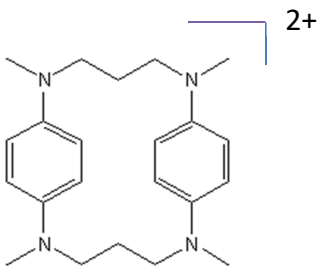

Scheme 4-1. Molecular structure of cyclophane compound **Me3C**$^{2+}$.

4.2 EXPERIMENTAL SECTION

4.2.1 Absorption Spectroscopy

Absorption spectra were taken of samples in dichloromethane solutions at room temperature. Spectra were obtained using a CARY 5000 UV-vis-nIR spectrophotometer.

4.2.2 Resonance Raman Spectroscopy

Samples were in the form of pressed pellets mixed with potassium nitrate as a standard. Raman spectra were collected with a triple monochromator equipped with a Princeton Instruments LN-CCD. Spectra were excited with multiple visible lines of a Coherent Argon ion gas laser (457 nm, 472 nm, 476 nm, 482 nm, 488 nm, 514 nm and 530 nm). Powers were kept at 20 mW or less with the pellet continuously spinning to minimize degradation.

4.2.3 DFT Calculations

Molecular orbitals were calculated in Gaussian 09[12] using the B3LYP/6-31g method and results imaged with GaussView 5. Calculated normal mode frequencies were also obtained, and experimental modes were assigned with the aid of Gaussian calculations.

4.3 RESULTS AND DISCUSSION

Absorption spectrum of **Me3C**$^{2+}$ in dichloromethane solution is shown in Figure 4-1. Two bands at 13900 cm^{-1} and 19300 cm^{-1} can be observed, and have been assigned as the transition from the highest occupied molecular orbital (HOMO) to the lowest unoccupied molecular orbital (LUMO), and HOMO-1 to LUMO, respectively.[5]

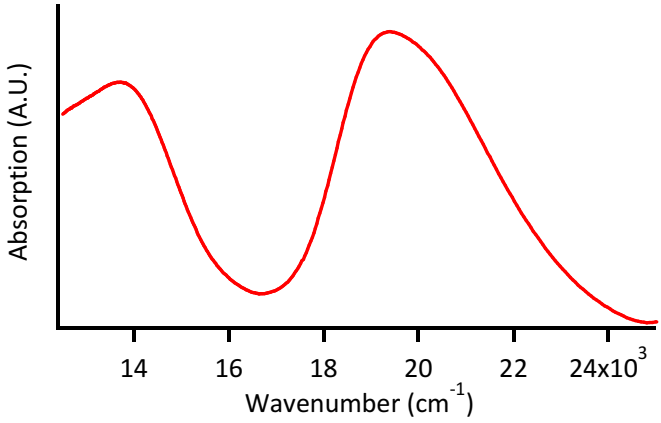

Figure 4-1. Absorption spectrum of **Me3C**$^{2+}$ in dichloromethane at room temperature.

A neighboring orbital model[13,14] can be constructed for this molecule in two steps. Shown in Figure 4-2 is the neighboring orbital model for a **TMPD** monomer, where the nitrogens are the charge bearing units and the coupling is mediated by the phenyl bridge. Two sets of molecular orbitals for the phenyl group are required to construct the appropriate MOs. The in-phase and out-of-phase nitrogen p orbitals coupled by the two sets of phenyl MOs produce four **TMPD** molecular orbitals, of which the three higher energy MOs are shown and are used to construct the neighboring orbital model for the full **Me3C**$^{2+}$ cyclophane molecule.

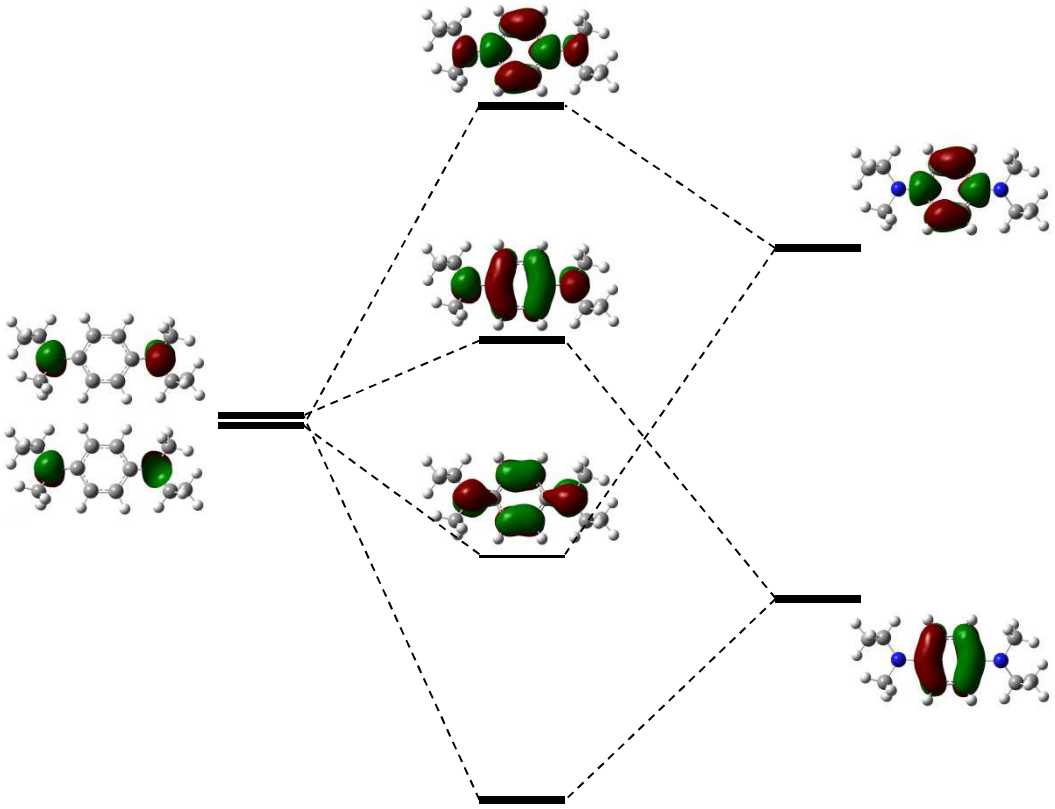

Figure 4-2. Neighboring orbital model for the **TMPD** monomer unit. In-phase and out-of-phase nitrogen orbitals are shown on the left, and two mediating phenyl bridge MOs are shown on the right.

The center two molecular orbitals closest in energy to the nitrogen orbitals have the greatest charge bearing unit character. In comparing these, it can be seen that the in-phase combination of the nitrogen p orbitals is lower in energy, indicating negative coupling.

The neighboring orbital model for **Me3C**$^{2+}$ is shown in Figure 4-3. Two **TMPD** monomers are allowed to couple, and form in-phase and out-of-phase combinations across the π-stacking interaction. The in-phase combinations give rise to the HOMO and LUMO+2, while the HOMO-1 and LUMO are out-of-phase across the mirror plane of the molecule.

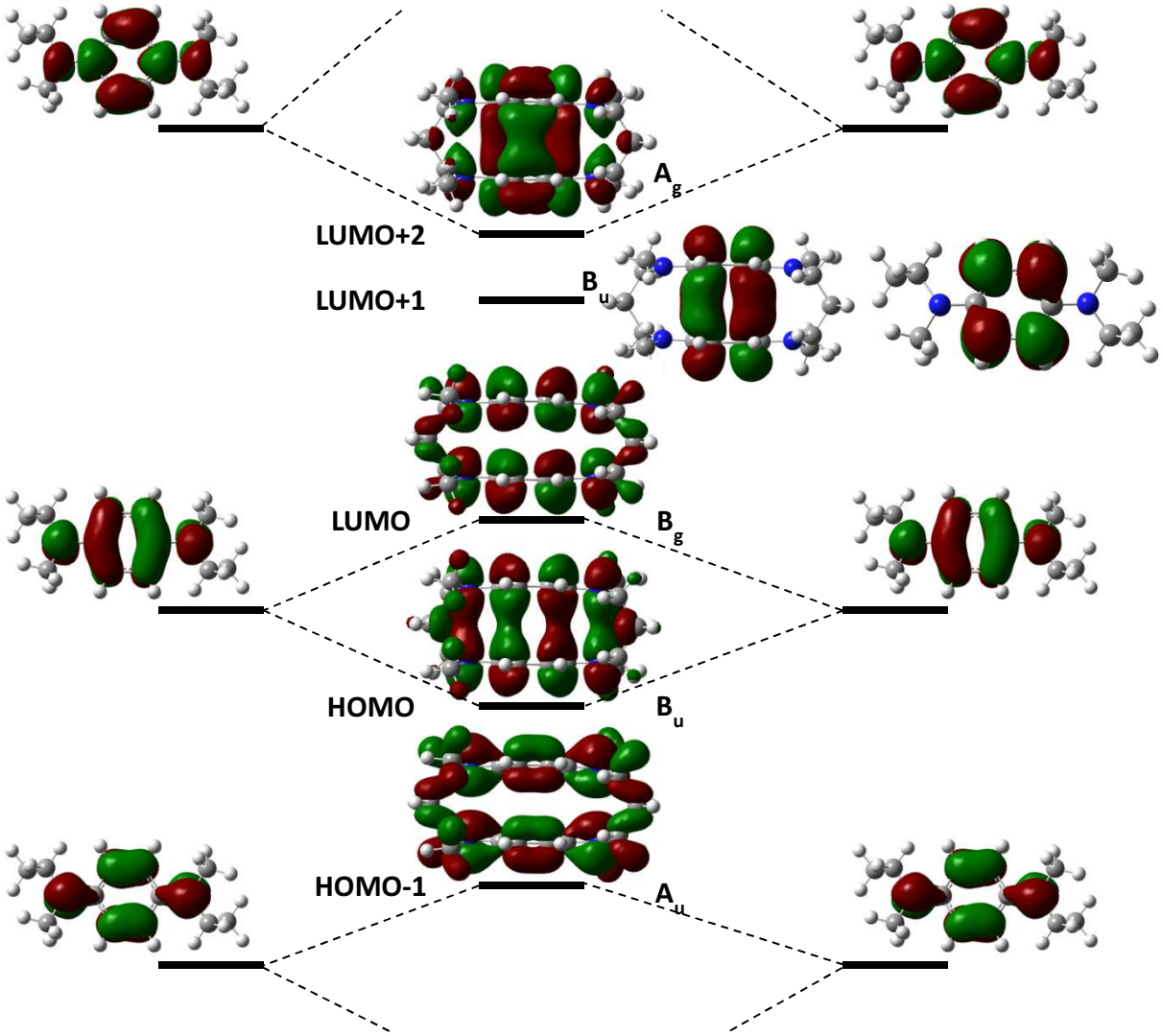

Figure 4-3. Neighboring orbital model for the bridged dimer cyclophane **Me3C**$^{2+}$. The top three **TMPD** monomer unit MOs are allowed to couple, forming the molecular orbitals shown in the center. Their irreducible representations are assigned under C_{2h} symmetry.

Comparison of the HOMO and LUMO show that the in-phase combination of the phenylenediamine MOs is lower in energy. This indicates that the coupling mediated through the π-stacking interaction is negative. This is a ground state mixed valence system, and the intense absorption band at 13900 cm^{-1} arises from the intervalence charge transfer between HOMO and LUMO.

Resonance Raman spectra were collected over several excitation wavelengths in resonance with the higher energy band, and the full Raman spectra at these excitations are shown in Figure 4-4. The most intense peaks belong to vibrational modes typical of phenyl rings in the 1000-1600 cm^{-1} region.

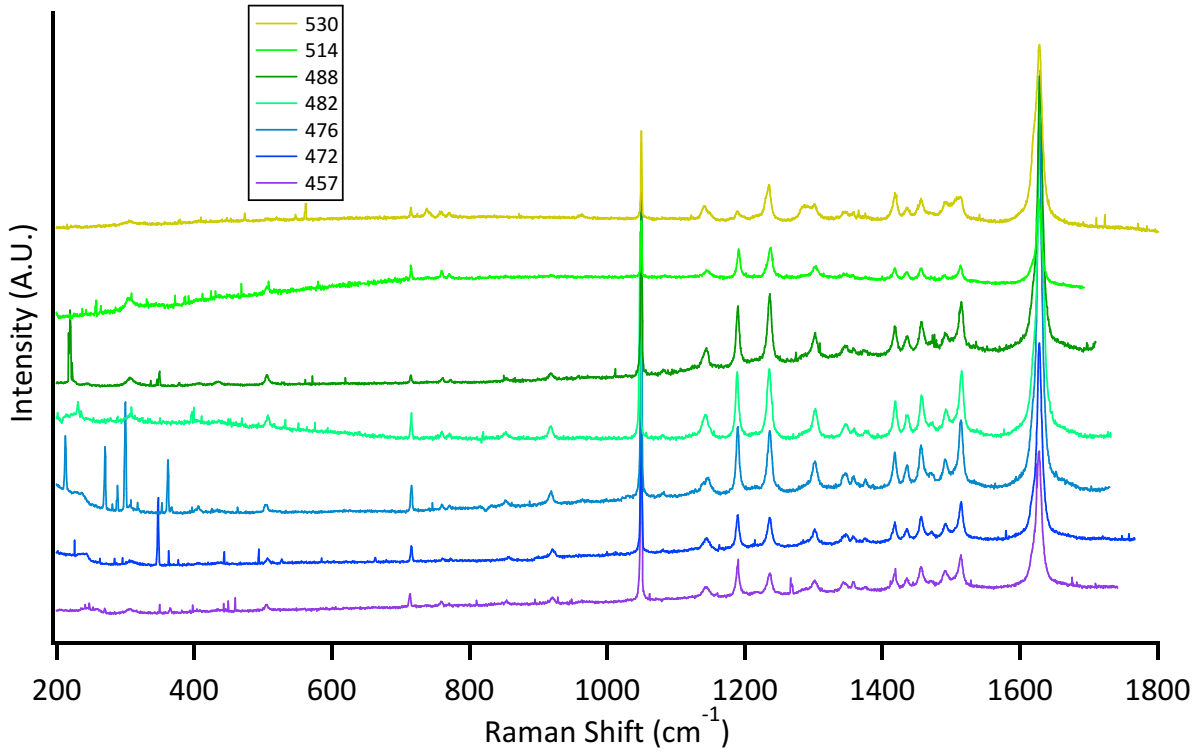

Figure 4-4. Resonance Raman spectra of solid **Me3C**$^{2+}$ excited at multiple wavelengths. Peaks at 715 cm^{-1} and 1050 cm^{-1} belong to the KNO_3 standard.

Peak intensities were integrated and normalized to the 1050 cm^{-1} KNO_3 standard peak. Presented in Table 4-1 are the peak intensities obtained from 457.9 nm excitation, along with the experimental frequencies, calculated frequencies, dimensionless distortions and mode assignments. Normal modes were assigned with the aid of Gaussian calculations and comparison to literature.[15] Dimensionless distortions were calculated from the relative intensities using Savin's formula.[16-18]

Exp. ω (cm^{-1})	Calc. ω (cm^{-1})	Relative intensity	Δ	Assignment
307	309	0.08	0.95	Bridge C-C-C bend, N-Ar-N bend
505	543	0.06	0.50	Out of plane ring butterfly
759	748	0.03	0.24	In plane ring elongation
852	846	0.05	0.28	In plane ring perpendicular elongation
921	929	0.08	0.32	In plane ring breathing
1144	1149	0.21	0.42	Ar-N out of plane wag, methyl wag
1190	1175	0.28	0.47	In plane ring breathing, Ar-N stretch
1236	1223	0.25	0.43	N-Ar-N in plane wag, methyl C-H wag
1302	1287	0.12	0.28	Ring C-H in plane wag
1345	1323	0.21	0.36	Ring elongation, bridge C-H wag
1358	1404	0.07	0.20	Ring alternate C-C stretch, in plane Ar-N wag
1418	1419	0.16	0.29	Bridge C-H wag
1436	1439	0.06	0.18	Ring C-H in plane wag, N-Ar-N stretch
1457	1472	0.20	0.32	Ring elongation, N-Ar-N stretch
1492	1499	0.16	0.28	Ring C-H in plane wag, methyl C-H wag
1514	1516	0.34	0.41	Ring C-C stretch, all C-H wag
1628	1681	1.89	0.89	Ring alternate C-C stretch, in plane Ar-N wag

Table 4-1. Experimental and calculated Raman frequencies, intensities, dimensionless distortions and mode assignments at 457.9 nm excitation. Intensities are relative to the 1050 cm^{-1} peak of standard KNO_3. Relative distortions calculated with Savin's formula.

The most intense peaks observed in the resonance Raman spectra pertain to normal modes that involve distortions in the phenyl ring or between the ring and the nitrogens. As the Raman spectra were collected in resonance with the higher energy band, this corresponds to a transition from the HOMO-1 to LUMO, where there are significant changes in the electron density across the phenylenediamine group. The bonding/antibonding characters over all C-C and N-C bonds change during this transition, which will enhance any vibrational modes that involve these bonds.

However, there is no change in electron density between the π rings, transitioning from out-of-phase to out-of-phase MO combinations. Resonance Raman excited in the region of this transition band will not have an enhanced peak corresponding to the normal mode of vibration

between the rings. Based on Gaussian DFT calculations, there exists a normal mode at the calculated frequency of 124 cm^{-1} that involves a change in distance between the phenyl rings ("inter-ring breathing"). But due to its low frequency, this peak is inherently low intensity, and the lack of resonance enhancement results in only an extremely weak peak observed in some of the spectra collected. This peak is too small to be integrated without a large uncertainty, and no analysis can be made using this peak.

To more fully understand the mixed valence coupling mediated through the inter-ring π-stacking, further investigation of the inter-ring normal mode needs to be made. A useful study would be to analyze the Raman spectra taken in resonance with the lower energy absorption band, as this corresponds to the HOMO to LUMO transition which involves a change in the electron density in between the rings. The inter-ring breathing mode should therefore be enhanced and can be more easily observed in the Raman spectra and analyzed.

4.4 SUMMARY

In this study, we have collected and assigned the absorption spectrum for the mixed valence compound **Me3C**$^{2+}$. This cyclophane compound contains four nitrogens that are charge bearing sites, and coupling between them can be mediated through the alkyl bridge, the phenylene bridge, or inter-ring π-π interaction. The two absorption bands correspond to an intervalence charge transfer band from the HOMO to LUMO and a HOMO-1 to LUMO transition. A neighboring orbital model was constructed to help understand the interactions of the charge bearing units and how they are coupled. Raman spectra were collected in resonance with the higher energy HOMO to LUMO band, providing distortion information of the vibrational normal modes. The most

intense modes observed correspond to vibrations that are enhanced by changes in electron density across the phenylenediamine units during the transition. The low frequency inter-ring breathing mode could not be clearly observed, and further investigation is required to better understand the coupling through π-stacking interactions.

4.5 REFERENCES

(1) Hush, N. S. *Prog. Inorg. Chem.* **1967**, *8*, 391.

(2) Day, P.; Hush, N. S.; Clark, R. J. H. *Phil. Trans. R. Soc. A* **2008**, *366*, 5.

(3) Robin, M. B.; Day, P. *Adv. Inorg. Chem. Radiochem.* **1968**, *10*, 247.

(4) Nelsen, S. F.; Li, G.; Schultz, K. P.; Tran, H. Q.; Guzei, I. A.; Evans, D. H. *J. Am. Chem. Soc.* **2008**, *130*, 11620.

(5) Jalilov, A. S.; Li, G.; Nelsen, S. F.; Guzei, I. A.; Wu, Q. *J. Am. Chem. Soc.* **2010**, *132*, 6176.

(6) Jalilov, A. S.; Nelsen, S. F.; Guzei, I. A.; Wu, Q. *Angew. Chem. Int. Ed.* **2011**, *50*, 6860.

(7) Casado, J.; Takimiya, K.; Otsubo, T.; Ramírez, F. J.; Quirante, J. J.; Ponce Ortiz, R.; González, S. R.; Moreno Oliva, M.; López Navarrete, J. T. *J. Am. Chem. Soc.* **2008**, *130*, 14028.

(8) Lee, S.-Y.; Heller, E. J. *J. Chem. Phys.* **1979**, *71*, 4777.

(9) Heather, R.; Metiu, H. *J. Chem. Phys.* **1989**, *90*, 6903.

(10) Tannor, D. J.; Heller, E. J. *J. Chem. Phys.* **1982**, *77*, 202.

(11) Heller, E. J.; Sundberg, R. L.; Tannor, D. J. *J. Phys. Chem.* **1982**, *86*, 1822.

(12) Frisch, M. J.; Trucks, G. W.; Schlegel, H. B.; Scuseria, G. E.; Robb, M. A.; Cheeseman, J. R.; Scalmani, G.; Barone, V.; Mennucci, B.; Petersson, G. A.; Nakatsuji, H.; Caricato, M.; Li, X.; Hratchian, H. P.; Izmaylov, A. F.; Bloino, J.; Zheng, G.; Sonnenb, D. J. Gaussian 09, 2009.

(13) Lockard, J. V.; Zink, J. I.; Trieber II, D. A.; Konradsson, A. E.; Weaver, M. N.; Nelsen, S. F. *J. Phys. Chem. A* **2005**, *109*, 1205.

(14) Nelsen, S. F.; Weaver, M. N.; Luo, Y.; Lockard, J. V.; Zink, J. I. *Chem. Phys.* **2006**, *324*, 195.

(15) Bailey, S. E.; Zink, J. I.; Nelsen, S. F. *J. Am. Chem. Soc.* **2003**, *125*, 5939.

(16) Zink, J. I.; Shin, K.-S. K. In *Advances in Photochemistry*; Wiley: New York; Vol. 16, pp. 119–214.

(17) Tang, J.; Albrecht, A. C. In *Raman Spectroscopy*; Szynanski, H., Ed.; Plenum Press: New York, 1970; Vol. 2, pp. 33–68.

(18) Warshel, A.; Dauber, P. *J. Chem. Phys.* **1977**, *66*, 5477.

Chapter 5

Time-Resolved Spectroscopy of Molecules Confined in Mesoporous Silica Nanoparticles

5.1 INTRODUCTION

In recent years, the study of mesoporous silica nanoparticles has attracted much attention due to their versatility in being modified and utilized as drug delivery vehicles. These nano-sized containers can be functionalized with a variety of nanomachines to be able to hold and release drugs on command, with different methods of activation including pH control,[1,2] light[3] and redox[4,5] activation. Much has been achieved for their application as drug delivery systems, but few studies have been done to investigate the microenvironment the drug or model dye resides in, in the mesopores of the particles.[6]

Previous work has been published by Min Xue et. al. investigating the microenvironment of a guest molecule encapsulated in the pore channels of pure silica nanoparticles and surface modified (positive and negative charge) silica nanoparticles.[7] In this study, we examine the physical environment of the guest molecule in azobenzene modified silica nanoparticles. This type of functionalized nanoparticle is one that has been developed in our group as an effective drug delivery system.[3,8,9] Azobenzene undergoes cis-trans isomerization under excitation at the wavelengths where both conformations absorb.[10] The continuous cis-trans isomerization produces a wagging motion that effectively acts as a nanoimpeller, expelling the guest molecules from within the pores. The probe molecules encapsulated within the mesopores should experience a change in its mobility and its environment due to the perturbation of the nanoimpeller wagging. The silica nanoparticles are also functionalized with a known stalk and cap system at the pore openings that only allows release under low pH.[11] In neutral conditions, this will prevent actual release of probe molecules when nanoimpellers are activated, allowing us to monitor the change in the microenvironment of the probe inside the pores. The capping system

also allows the probe molecules to be loaded and trapped in the mesopores, while those adsorbed on the outer surface can be removed with subsequent washing, thereby removing interference of probe molecules that are outside of the mesopores.

In our study, the probe molecule tris(bipyridine)ruthenium (II) hexafluorophosphate (RuBPy) (Scheme 5-1) was used to conduct time-resolved fluorescence anisotropy and rigidochromism studies. The former gives an understanding of the mobility of the probe molecule itself, while the latter reveals the rigidity of the microenvironment inside the pores surrounding the probe molecule.

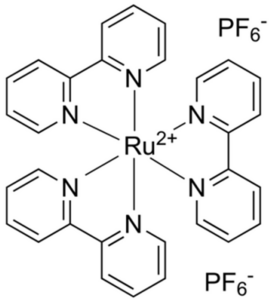

Scheme 5-1. Molecular structure of probe molecule tris(bipyridine)ruthenium (II) hexafluorophosphate

Fluorescence anisotropy occurs when a molecule is excited with a polarized beam of light. The fluorescence emitted by the molecule may be preferentially polarized in a certain direction depending on its orientation and its dipole moments, resulting in fluorescence anisotropy. However, this anisotropy will be eliminated as the molecule rotates from its original orientation. Therefore, by monitoring the time-resolved decay of the fluorescence anisotropy, the mobility of molecule can be understood.[12-15]

The rigidochromic effect, on the other hand, is a probe of the solvents surrounding the molecules. The energies of the ground and excited states depend on the how the dipole moments of the molecule and the surrounding solvent molecules are oriented. Depending on the rigidity of the solvent matrix, the orientation of the surrounding solvent dipoles with respect to the excited state dipole moment of the molecule will be different and will affect the energy of the excited state, thus resulting in a shift in emission energy according to the environment rigidity.[16-18]

Using a combination of these spectroscopic techniques, we can acquire a better understanding of the microenvironment inside the pores of mesoporous silica nanoparticles, and how it differs with the presence of activated azobenzene nanoimpellers. This provides good insight and fundamental understanding to the behavior of dye or drug molecules in mesoporous silica nanoparticle drug delivery systems.

5.2 EXPERIMENTAL SECTION

5.2.1 Synthesis of Mesoporous Silica Nanoparticles (MSNP)

The syntheses of MSNP and azobenzene modified MSNP were done by fellow lab mates Juyao Dong and Chia-Jung Yu according to known procedures.[3,11]

5.2.2 Choice of Probe Molecule

Several factors need to be taken into account when considering the choice of an appropriate probe for the time-resolved fluorescence anisotropy and rigidochromism studies. The most important of these, is choosing a probe molecule with a sufficiently long lifetime to allow observation of tumbling of the molecule or solvent reorganization. For low mobility, as we

expect for molecules confined within the mesopores, molecular tumbling will not have time to occur before emission if fluorescence lifetime is too short. A related factor is the symmetry of the molecule. To observe the overall tumbling of the molecule, an asymmetric system would be far more complex as its tumbling will not be isotropic. An asymmetric system could also have interaction of the probe with its surroundings that are asymmetric and complicate the observations. Therefore, a molecule that is roughly spherical (as opposed to rod shaped) would be most suitable.

In our studies, we are concerned with investigating the physical properties and environments of drugs loaded in our drug delivery systems in mesoporous silica nanoparticles. Therefore, choosing a probe molecule that is similar in size to dyes and drugs that are commonly used would be most appropriate. Lastly, the photo-stability of the probe molecule also needs to be high. Considering all of the above factors, the RuBPy compound[19,20] has been chosen as a probe molecule for our studies.

5.2.3 Probe Molecule Loading

RuBPy probe molecules were loaded into MSNPs by soaking 10 mg of nanovalve functionalized MSNP or impeller/nanovalve functionalized MSNP in 2 mL of 0.2 mM RuBPy aqueous solution. RuBPy probes were allowed to load for three days at room temperature with continuous mixing. Loaded samples were capped with 50 mg of α-cyclodextrin and left for a day. The loaded and capped nanoparticles were then centrifuged and washed with deionized water five times to remove excess and surface adsorbed probe molecules.

After thorough washing, samples in aqueous solution were placed in 2 mm glass culture tubes and purged with argon for 30 minutes. The nanoparticles were then centrifuged down and the supernatant removed under argon, leaving a wet pellet for spectroscopic studies.

5.2.4 Fluorescence Anisotropy Spectroscopic Methods

Fluorescence lifetime measurements were taken with a 0.3 m single monochromator (300 groove/mm grating) equipped with a Roper Scientific PI-MAX gated, intensified CCD. The excitation source used was a Quantel Brilliant Compact pulsed Nd:YAG laser equipped with an OPOTEK Optical Parametric Oscillator Magic Prism for conversion to continuous wavelength. In the studies with nanovalve modified MSNP, wavelength of 445 nm was used. In the studies with impeller/nanovalve modified MSNP, a wavelength of 498 nm was selected. This wavelength was chosen to allow absorption of the RuBPy molecules, but not of the azobenzene nanoimpellers and avoid activation of the wagging motion. A Newport Precision Linear Polarizer was placed in front of the laser beam to ensure the excitation beam polarity. A Glan-Thompson polarizer was placed in front of the monochromator to selectively measure parallel and perpendicular components of the fluorescence emission, while a polarization scrambler was also placed in front of the monochromator to avoid any spectroscopic polarization bias of the detection system. A Coherent CUBE 403 nm laser was used as pump beam for activating the nanoimpellers, and another Glan-Thompson polarizer was placed in front of this laser to ensure polarity in the same direction as the pulse laser. All laser powers were attenuated with neutral density filters to low intensities to minimize degradation of the sample. Spectroscopic measurements were performed on each sample for a maximum of five hours to avoid photo-degradation effects.

5.2.5 Rigidochromism Spectroscopic Methods

In the rigidochromism studies, RuBPy aqueous solution and RuBPy loaded nanoparticles were excited by a Coherent Ar ion gas laser at 496 nm, and the fluorescence spectra collected by a Princeton Instruments LN-CCD camera equipped with an Acton 2300i monochromator. A Coherent CUBE 403 nm laser was used as the pump beam for activating the nanoimpellers. All laser powers were set to minimum powers and attenuated with neutral density filters to low intensities to avoid degradation of the sample.

5.3 THEORIES AND PRINCIPLES

5.3.1 Time-Resolved Fluorescence Anisotropy

The fluorescence of a single molecule is polarized depending on its dipole moment in the excited state, whereas the probability of it absorbing polarized light is dependent on the angle between the ground state dipole moment and the electric field vector of the excitation light. Because of this dependency, for a sample of randomly oriented molecules, the fluorescence emission will be partially polarized, and fluorescence anisotropy will be observed. If the molecules are freely rotating on a timescale within its fluorescence lifetime, then the emission polarization will become randomized and the fluorescence anisotropy will decay over time. The decay rate correlates to the mobility of the molecule in its environment, and can therefore be an indicator of how the environment is affecting the molecule.

The polarization of the electric field vector of the excitation beam is therefore an important factor to consider. The electric field vector of a light wave is oscillating and is given by the equation

$$E = A \cdot \cos(kx - \omega t + \varphi) \tag{49}$$

where A is the amplitude of the vector. The intensity of this light wave is proportional to the square of the amplitude. Viewing along the axis of the direction of the light beam (z), the amplitude of the light wave can be projected onto the x and y axis, and decomposed into two orthogonal components, A_x and A_y (Figure 5-1).

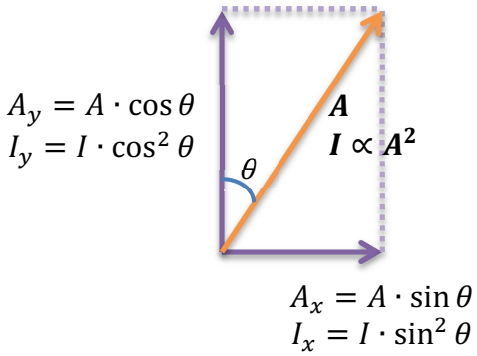

Figure 5-1. Depiction of intensity and amplitude of light projected onto x and y components.

The intensity of the light can also be expressed as a sum of the two components.

$$I = I_x + I_y = I \cdot \sin^2\theta + I \cdot \cos^2\theta \tag{50}$$

As earlier discussed, emission intensity of the fluorophores is partially polarized. Therefore, it can be decomposed into two components, a polarized component (I_p), and an unpolarized component (I_u), shown in Figure 5-2.

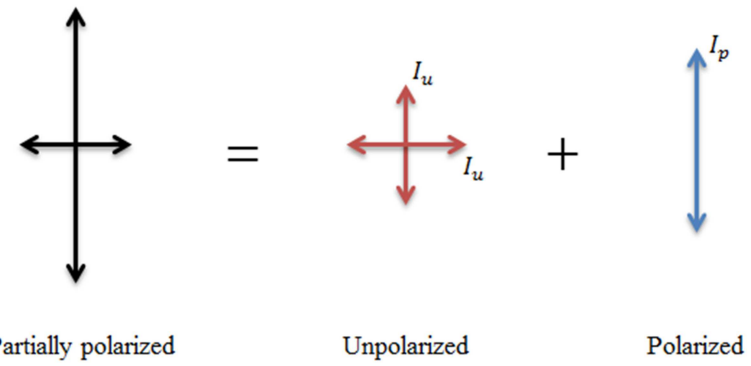

Figure 5-2. Depiction of the decomposition of a partially polarized light decomposed into polarized and non-polarized components.

The component of light parallel to the polarization is defined as the parallel direction ($I_{\parallel}$, shown here to be in the vertical direction), while the perpendicular direction refers to the direction orthogonal to both the parallel direction and the direction of travel ($I_{\perp}$, horizontal direction). The polarized and unpolarized components can be related to the parallel and perpendicular components with $I_{\parallel} = I_p + I_u$ and $I_{\perp} = I_u$. It can then be easily found that

$$\begin{cases} I_p = I_{\parallel} - I_{\perp} \\ I_u = I_{\perp} \end{cases} \tag{51}$$

However, emission is three dimensional so there is a second perpendicular component with the same intensity of $I_{\perp}$, giving a total emission intensity of $I_{total} = I_{\parallel} + 2I_{\perp}$. The ratio of the polarized component over the total emission intensity is defined as the fluorescence anisotropy *r*:

$$r = \frac{I_p}{I_{total}} = \frac{I_{\parallel} - I_{\perp}}{I_{\parallel} + 2I_{\perp}} \tag{52}$$

We will now consider the anisotropy that occurs due to the random orientation of the molecules. Consider a fluorophore oriented such that its emission dipole moment is at an angle θ from the vertically polarized excitation light, and an angle ϕ from the perpendicular direction (Figure 5-3).

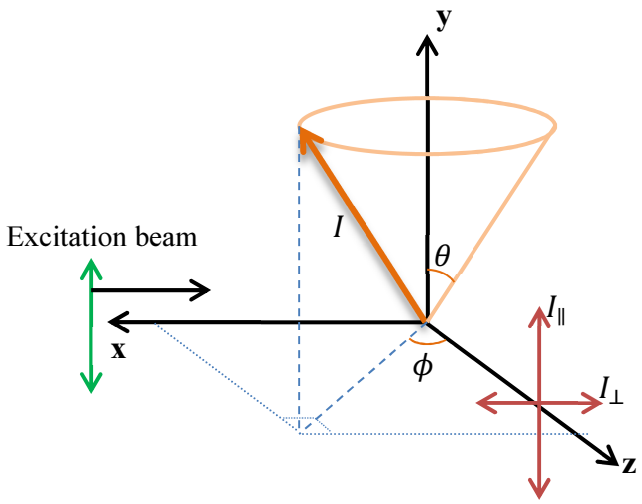

Figure 5-3. Emission dipole moment depicted in the coordinate system.

For an emission intensity of I, the intensities in the parallel and perpendicular directions are:

$$\begin{cases} I_{\parallel} = \cos^2\theta \cdot I \\ I_{\perp} = \sin^2\theta \cdot \sin^2\phi \cdot I \end{cases} \tag{53}$$

The excitation probability of a molecule of this orientation is proportional to the projection of the excitation beam in the direction of the molecule's dipole moment, which is $\cos^2\theta$. For the entire sample of randomly oriented molecules, the proportion of dipoles between the angles θ and $\theta + \mathrm{d}\theta$ is equal to the proportion of the surface area of that strip of sphere over the entire sphere:

$$\frac{\int_{\phi=0}^{2\pi}\int_{\theta}^{\theta+d\theta} r^2 sin\theta d\theta d\phi}{4\pi r^2} = \frac{2\pi r^2 \int sin\theta d\theta}{4\pi r^2} = \frac{1}{2}\int sin\theta d\theta \tag{54}$$

Therefore, the total probability of excitation, P_θ, is

$$P_\theta = \int \cos^2\theta \cdot sin\theta d\theta \tag{55}$$

Accounting for all the possible orientation of dipoles for the entire sample, the parallel and perpendicular intensities become

$$I_{\parallel} = cos^2\,\theta \cdot I_0 \cdot P_\theta = I_0 \int_0^{\pi} cos^4\,\theta sin\theta d\theta = \frac{2}{5} I_0 \tag{56}$$

$$I_{\perp} = sin^2\,\theta \cdot sin^2\,\varphi \cdot I_0 \cdot P_\theta = \frac{I_0 \int_0^{\pi} \int_0^{2\pi} cos^2\,\theta\, sin^3\,\theta\, sin^2\,\varphi\, d\varphi d\theta}{\int_0^{2\pi} d\varphi} = \frac{2}{15} I_0 \tag{57}$$

Therefore, the intrinsic anisotropy due to the random orientation of molecules and their absorption probabilities is

$$r_1 = \frac{I_{\parallel} - I_{\perp}}{I_{\parallel} + 2I_{\perp}} = \frac{2}{5} \tag{58}$$

However, this is under the assumption that the absorption transition dipole moment is in the same direction as the emission dipole moment In most cases the directions will be different. An angle of α between them will result in further intrinsic anisotropy. Mathematically, we can consider the absorption dipole moment to be our new frame of reference, and the emission dipole to be an angle α from it. Then the parallel and perpendicular intensities can be written as

$$\begin{cases} I_{\parallel} = \cos^2 \alpha \cdot I \\ I_{\perp} = \sin^2 \alpha \cdot \sin^2 \phi \cdot I \end{cases} \tag{59}$$

Averaging over all angles of ϕ,

$$\langle sin^2\,\varphi \rangle = \frac{\int_0^{2\pi} sin^2\,\varphi d\varphi}{\int_0^{2\pi} d\varphi} = \frac{1}{2} \tag{60}$$

Therefore,

$$I_{\perp} = \frac{1}{2} sin^2 \alpha \cdot I_0 \tag{61}$$

and the intrinsic anisotropy due to the angle between absorption and emission dipoles is

$$r_2 = \frac{I_{\parallel} - I_{\perp}}{I_{\parallel} + 2I_{\perp}} = \frac{cos^2 \alpha - \frac{1}{2} sin^2 \alpha}{cos^2 \alpha + sin^2 \alpha} = \frac{3\, cos^2 \alpha - 1}{2} \tag{62}$$

The total anisotropy can therefore be calculated to be

$$r_0 = r_1 \cdot r_2 = \frac{3\, cos^2 \alpha - 1}{5} \tag{63}$$

This fundamental anisotropy can range from -0.20 (at angle $\alpha = 90°$) to 0.40 (at angle $\alpha = 0°$).

When the molecules are freely rotating, the inherent anisotropy will decay over time. This decay can be fit with an exponential decay function, and its decay lifetime is defined as the rotational correlation lifetime τ_c.

$$r(t) = r_0 e^{-\frac{t}{\tau_c}} \tag{64}$$

The less mobile the molecules are, the longer it takes for the molecules to rotate away from their initial orientations, and the longer it takes for the inherent anisotropy to decay, resulting in a longer rotational correlation lifetime. The rotational correlation lifetime should not be confused with the inherent lifetime of emission intensities decay. These two lifetime values can provide information about the mobility of the molecule in its environment.

5.3.2 Rigidochromism

For a fluorophore molecule in a solvent, the solvent molecules are oriented such that their dipole moments align with the dipole moment of the fluorophore to achieve the best energy stabilization. When the fluorophore is excited, its dipole moment may change direction. If the

solvent molecules are sufficiently loose and free to move, they will reorient to align with the excited state dipole moment before the fluorophore emits, thereby lowering the energy of the excited state. If the solvent matrix is rigid, the solvent dipole moments cannot realign before fluorescence from the fluorophore occurs, and the excited state will be at a slightly higher energy (Figure 5-4).

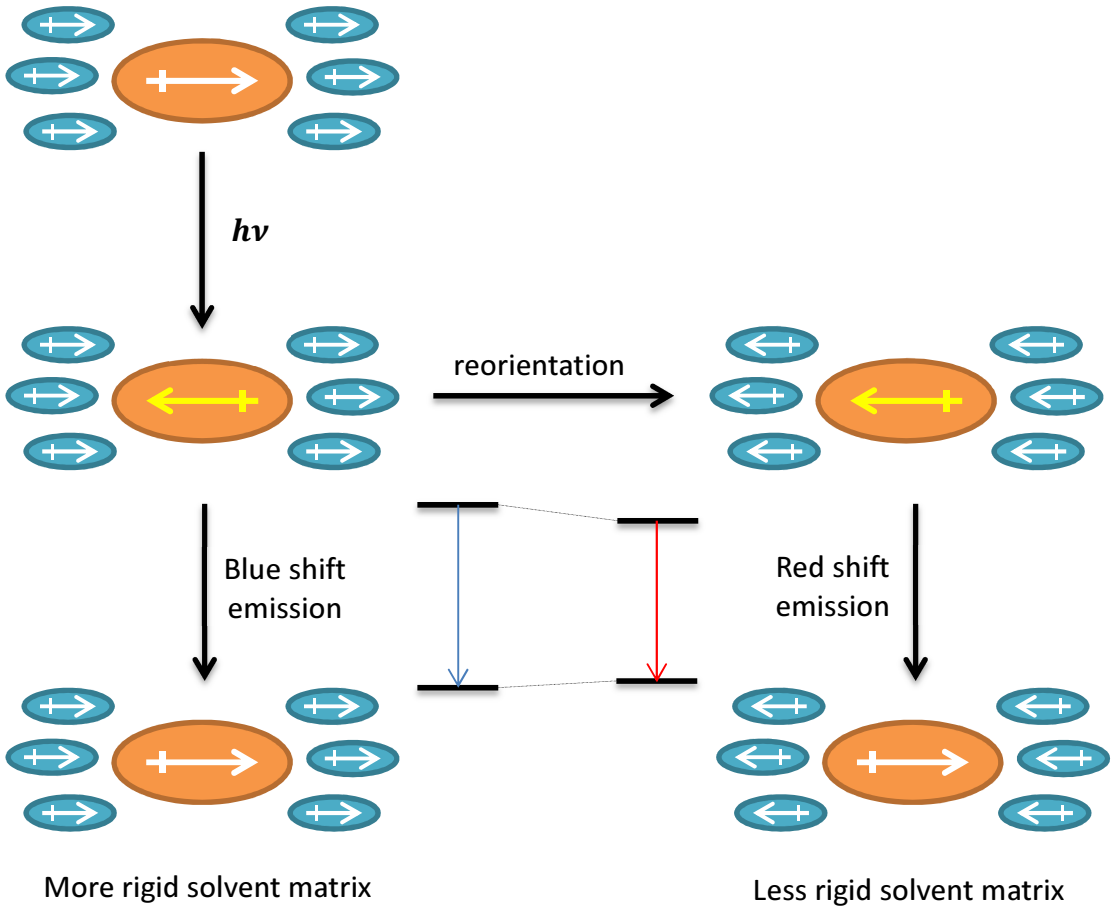

Figure 5-4. Depiction of the effect of solvent matrix rigidity on emission wavelength, resulting in the rigidochromic effect.

Therefore, by observing the shift of the emission maximum, the rigidity of the solvent matrix can be inferred. A blue shift indicates a higher energy excited state, therefore a more rigid environment, whereas a shift to longer wavelengths indicates a less rigid solvent matrix.

5.3.3 Transient Absorption

In this study, we investigate the effects activated nanoimpellers have on the mobility and therefore rotational correlation lifetime of RuBPy. The azobenzene nanoimpellers display cis-trans isomerization when excited at 403 nm, whereas the RuBPy probe is monitored at 498 nm. However, as 403 nm is within the absorption range of RuBPy, it is important to consider whether or not transient absorption of 498 nm will occur when the 403 nm pump is on. To do so, we will consider the proportion of molecules in the excited state due to the 403 nm pump.

There exists an equilibrium between the excited state and ground state when RuBPy is continuously excited by 403 nm, with a forward rate constant of *k*, and a reverse rate constant *k'*:

$$ground\ state \rightleftharpoons excited\ state \tag{65}$$

The rate of the forward reaction is equal to the rate of absorption:

$$R = \sigma \times \frac{I}{h\nu} \tag{66}$$

where I is the optical density (Wm^{-2}), $h\nu$ is the energy of the photon (J), σ is the cross section (m^2), and can be found from the equation for transmittance T:

$$T = e^{-N\sigma L} = e^{-A} \tag{67}$$

where N is the molecular density (m^{-3}), L is the path length (m), and A is the absorbance.

The excitation beam used in our experiments is about 2×10^{-4} W, with a beam size of about 3 mm^2, which translates to an intensity of $I = 66.7\ Js^{-1}m^{-2}$. The concentration of the RuBPy solution is $2.0 \times 10^{-7} molL^{-1} = 1.216 \times 10^{20} molecules\ m^{-3} = N$. The experimentally

measured absorption at 403 nm is 0.1807, therefore, the absorption cross section can be found to be

$$\sigma = \frac{A}{NL} = \frac{0.1807}{1.216 \times 10^{20} \times 10^{-2}} = 1.486 \times 10^{-19}\, m^2 \quad (68)$$

The forward rate constant can be calculated to be

$$k = R = \sigma \times \frac{I}{h\nu} = 1.486 \times 10^{-19} \times \frac{66.7}{6.626 \times 10^{-34} \times 7.44 \times 10^{14}} = 20.11\, s^{-1} \quad (69)$$

The rate constant for the reverse reaction is equal to the inverse of the emission lifetime:

$$k' = \frac{1}{0.8\, \mu s} = 1.25 \times 10^{6}\, s^{-1} \quad (70)$$

Therefore, the equilibrium ratio of the excited state versus ground state populations is

$$K = \frac{[excited\ state]}{[ground\ state]} = \frac{k}{k'} = \frac{20.11}{1.25 \times 10^{6}} = 1.61 \times 10^{-5} \quad (71)$$

It can be seen from these calculations that the proportion of the excited state over the ground state population is very small, and the likelihood of a molecule being in its excited state and undergoing excited state absorption at 498 nm is very low.

5.4 RESULTS

5.4.1 Time-Dependent Fluorescence Anisotropy Studies

As a control group, the time-dependent fluorescence anisotropy was monitored for RuBPy probe molecules confined in mesoporous silica nanoparticles but without the azobenzene nanoimpellers. Nanovalves were attached to the particles to contain the probe molecules inside

the pores, and to be able to remove probes that are adsorbed on the surface by washing without losing the probes. The nanovalve system chosen is a well-established pH sensitive valve capped with α-cyclodextrin. Spectra both with and without 403 nm pumped samples were monitored. The fluorescence lifetime τ_F for RuBPy excited at 498 nm without the 403 nm pump was measured to be 0.869 μs. The parallel and perpendicular fluorescence lifetimes observed were 0.806 μs and 0.815 μs respectively, with the rotational correlation lifetime τ_r calculated to be 0.84 μs. When the 403 nm pump is turned on, τ_F was 0.819 μs and the parallel and perpendicular lifetimes 0.787 μs and 0.812 μs, giving a τ_r of 0.84 μs (Figure 5-5). Results for lifetime measurements of RuBPy probe molecules in nanoparticles without nanoimpeller functionalization are summarized in Table 5-1.

	No 403 nm	With 403 nm
Fluorescence τ_F	0.869 μs	0.819 μs
Parallel τ	0.806 μs	0.787 μs
Perpendicular τ	0.815 μs	0.812 μs
Anisotropy τ_r	0.84 μs	0.84 μs

Table 5-1. Fluorescence lifetimes τ_F and rotational correlation lifetimes τ_r of RuBPy probe molecules loaded in silica nanoparticles with stalk and cap.

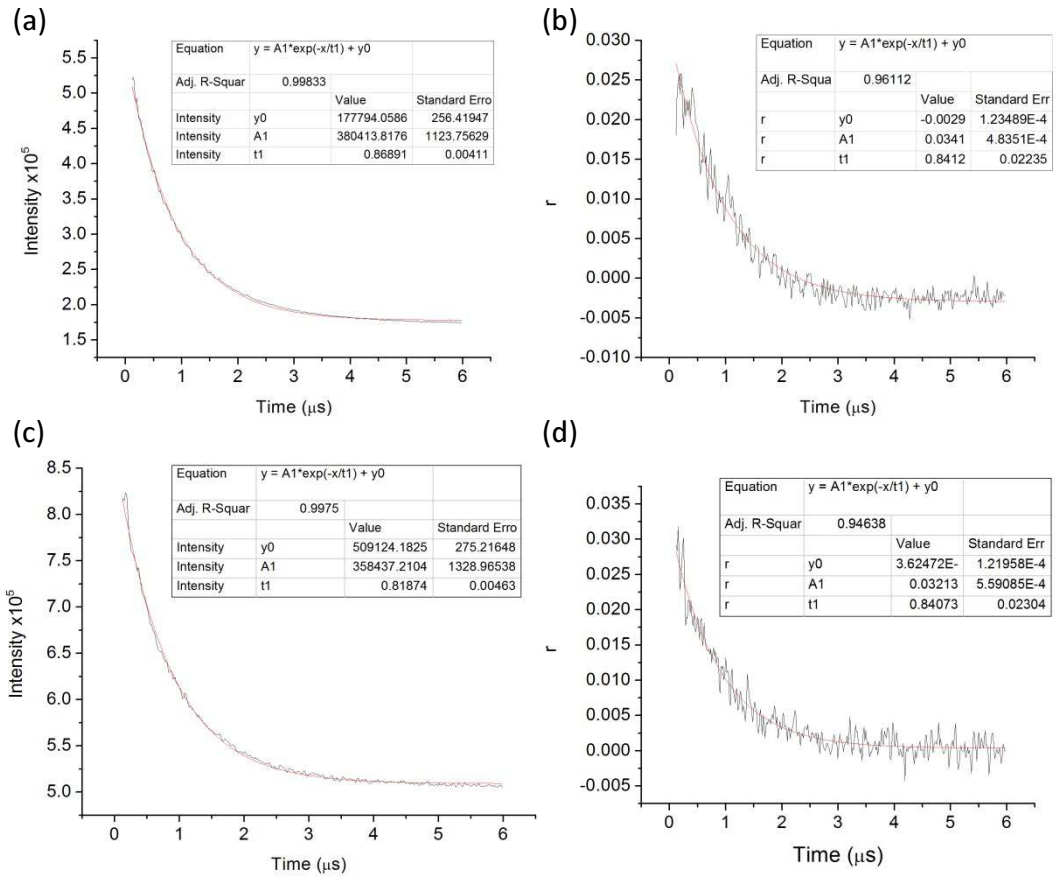

Figure 5-5. Spectroscopic studies on RuBPy loaded nanoparticles with stalk and cap. (a) Fluorescence intensity decay and (b) fluorescence anisotropy decay without 403 nm pump. (c) Fluorescence intensity decay and (d) fluorescence anisotropy decay with 403 nm pump.

Fluorescence anisotropy studies were then carried out on RuBPy loaded in nanoimpeller functionalized silica nanoparticles. Similarly, the nanoparticles were capped with cyclodextrin to prevent any loss of probe molecules when the nanoimpellers are activated. Any motion the nanoimpellers produce should not expel the probe molecules outside the confined environment. In the microenvironment without a 403 nm pump, azobenzene nanoimpellers are not excited and do not undergo cis-trans wagging motion. Under this condition, the fluorescence lifetime τ_F for RuBPY excited at 498 nm is measured with two trials on two batches of particles, synthesized and loaded separately. The first trial measured a fluorescence lifetime of 0.887 μs, while the

second gave 1.042 μs. For trial one, the parallel and perpendicular fluorescence lifetimes were measured to be 0.810 μs and 0.803 μs respectively, and a rotational correlation lifetime can be calculated to be 0.91 μs. For trial two, the two orientation lifetimes were 1.025 μs and 1.024 μs, giving a rotational correlation lifetime of 1.9 μs (Figure 5-6).

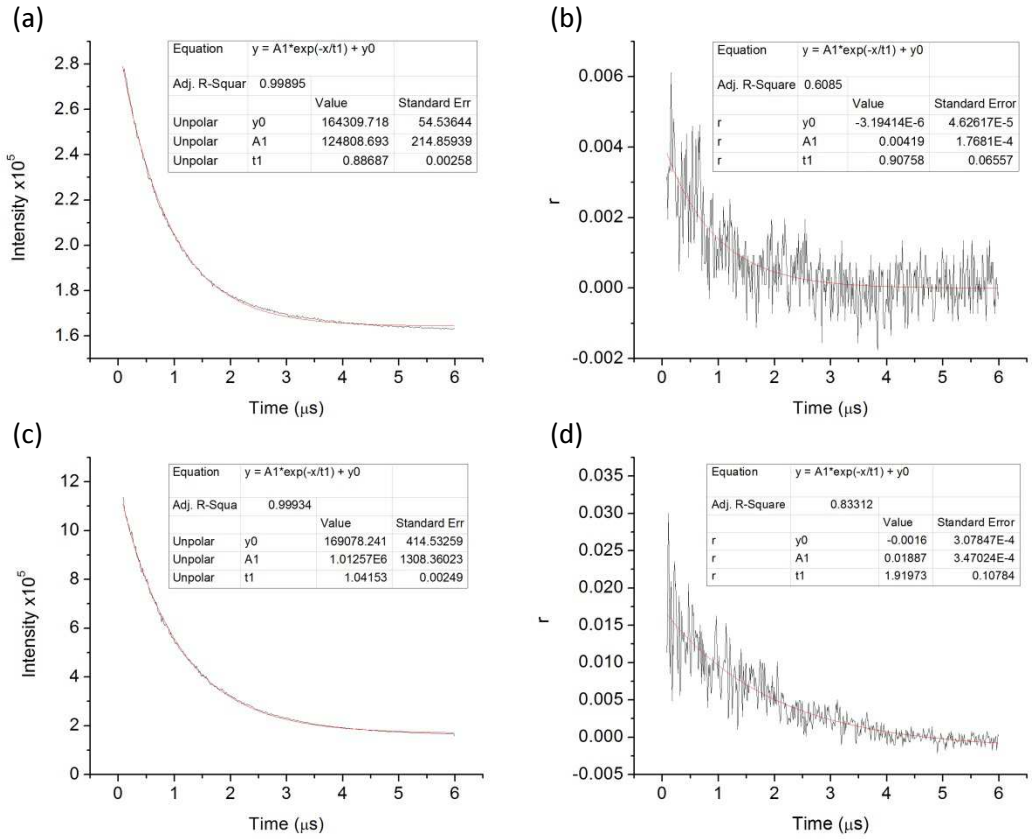

Figure 5-6. Spectroscopic studies on RuBPy loaded nanoimpeller functionalized nanoparticles. Nanoimpellers are not activated by 403 nm pump. (a) Fluorescence intensity decay and (b) fluorescence anisotropy decay for trial 1. (c) Fluorescence intensity decay and (d) fluorescence anisotropy decay for trial 2.

The studies were then performed on the same two sets of samples, but with the 403 nm pump on, thereby activating the cis-trans isomerization wagging motion of the azobenzene nanoimpellers. For trial 1, fluorescence lifetime was observed to be 0.797 μs, parallel and

perpendicular fluorescence lifetimes were 0.792 μs and 0.772 μs respectively, resulting in a rotational correlation lifetime of 0.99 μs. For trial 2, fluorescence lifetime was 1.081 μs, while the parallel and perpendicular lifetimes were 1.044 μs and 1.040 μs, giving a rotational correlation lifetime of 2.2 μs (Figure 5-7). These results are summarized in Table 5-2.

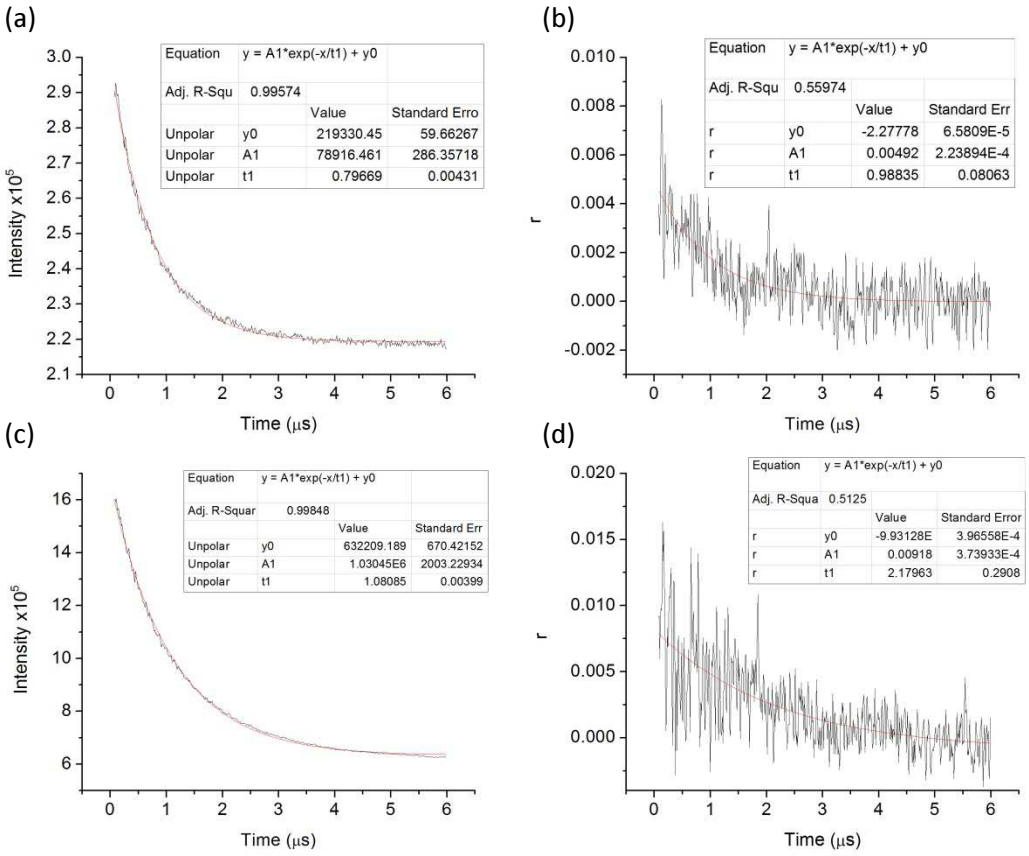

Figure 5-7. Spectroscopic studies on RuBPy loaded nanoimpeller functionalized nanoparticles. Nanoimpellers producing wagging motion with activation using 403 nm pump. (a) Fluorescence intensity decay and (b) fluorescence anisotropy decay for trial 1. (c) Fluorescence intensity decay and (d) fluorescence anisotropy decay for trial 2.

Impeller nanoparticles	Trial 1		Trial 2	
	No 403 nm	With 403 nm	No 403 nm	With 403 nm
Fluorescence τ_F	0.887 μs	0.797 μs	1.042 μs	1.081 μs
Parallel τ	0.810 μs	0.792 μs	1.025 μs	1.044 μs
Perpendicular τ	0.803 μs	0.772 μs	1.024 μs	1.040 μs
Anisotropy τ_r	0.91 μs	0.99 μs	1.9 μs	2.2 μs

Table 5-2. Fluorescence lifetimes τ_F and rotational correlation lifetimes τ_r of two trials of RuBPy probe molecules loaded in nanoimpeller functionalized silica nanoparticles. Azobenzene nanoimpellers are activated with 403 nm pump.

5.4.2 Rigidochromism Studies

Rigidochromism studies were performed on RuBPy probe molecules in three environments: in pure aqueous solution, loaded in silica nanoparticles and capped, and loaded in nanoimpeller functionalized silica nanoparticles and capped. Without the 403 nm pump, the peak maxima of the fluorescence emission bands are 610 nm, 595 nm and 600 nm, respectively (Figure 5-8).

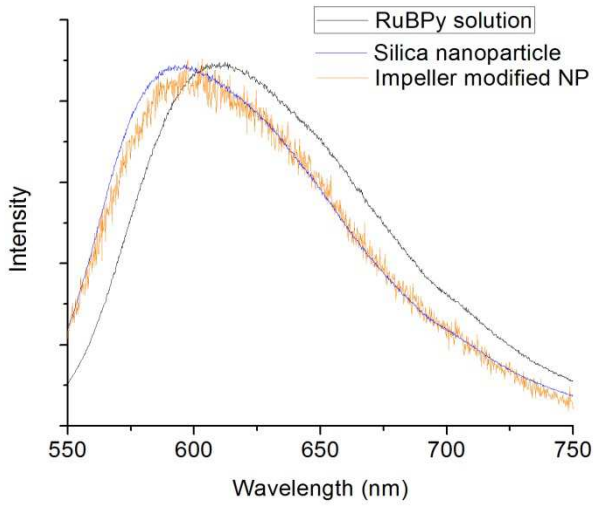

Figure 5-8. Emission spectra of RuBPy solution and RuBPy loaded samples of silica nanoparticles with and without nanoimpeller functionalization.

Fluorescence spectra were also acquired for the three environments but with a 403 nm pump laser. The peak maxima of pure RuBPy solution and loaded in pure silica nanoparticles are not affected by the 403 nm pump and do not change. For RuBPy loaded in nanoimpeller modified particles, the presence of a 403 nm pump resulted in a shift in peak maximum to 593 nm. Comparison of emission bands with and without 403 nm pump for all three environments are shown in Figure 5-9. Peak maxima wavelengths are summarized in Table 5-3.

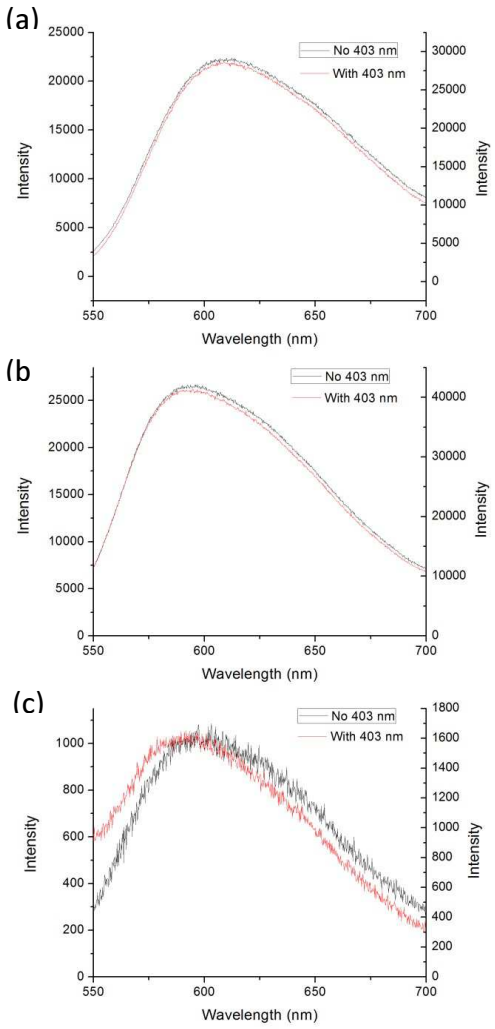

Figure 5-9. Emission spectra with and without 403 nm pump of (a) RuBPy aqueous solution, (b) RuBPy loaded silica nanoparticles without nanoimpeller functionalization and (c) RuBPy loaded nanoimpeller functionalized silica nanoparticles.

	Without 403 nm pump	With 403 nm pump
RuBPy solution	610 nm	610 nm
RuBPy in NP with no nanoimpeller	595 nm	595 nm
RuBPy in NP with nanoimpeller	600 nm	593 nm

Table 5-3. Fluorescence emission maxima for RuBPy molecules in different environments. Azobenzene nanoimpellers are activated with 403 nm pump.

5.5 DISCUSSION

5.5.1 Time-Dependent Fluorescence Anisotropy Studies

Fluorescence lifetime and rotational correlation lifetime of pure RuBPy molecules in an aqueous solution were measured in a previous study[7] and were found to be 0.49 μs and 0.025 μs, respectively. Comparison with measurements of RuBPy probe molecules entrapped in silica nanoparticles with stalk and cap system show that both τ_F and τ_r are much longer for confined RuBPy, indicative of their limited mobility in the restrained environment. The presence of the 403 nm pump has a minimal effect on the rotational correlation lifetime as it does not create any addition motion in the pores of particles without nanoimpellers.

For RuBPy probe molecules loaded in azobenzene functionalized nanoparticles, the fluorescence lifetime and rotational correlation lifetime is again longer than that of RuBPy in pure water solution, as they are in a confined environment. Lifetime results from the two trials are slightly different as they are measurements for different batches of nanoparticles synthesized and loaded. The degree of azobenzene functionalization may differ slightly between the two batches, as will the concentration of RuBPy molecules loaded. However, both batches display

the same trend in rotational correlation lifetime as the 403 nm pump is turned on, albeit to a different extent. With the nanoimpellers activated, both samples display an increase in the rotational correlation lifetime.

An increase in rotational correlation lifetime indicates a decrease in mobility, as a longer period of time is required for the fluorescence anisotropy to decay. This result is unexpected as we anticipated an increase in mobility due to the cis-trans isomerization wagging motion of the activated nanoimpellers, creating more motion in the confined probe molecules. One possible explanation is the effect of confining the molecules in the pores with the cyclodextrin cap. In previous studies with the nanoimpeller functionalized nanoparticles as a drug delivery system, the mesopores are not capped and cargo are allowed to freely move and are thereby expelled by the wagging motion of the nanoimpellers. In our system, the cap prevents escape of the RuBPy molecules even as the nanoimpellers are moving them. This could potentially create a build-up of RuBPy molecules in certain regions. The higher concentration of RuBPy molecules could create a more confined microenvironment and decrease the mobility of the molecules themselves, resulting in the longer rotational correlational lifetime observed. However, further investigation is required to confirm this possibility. Proposed experiments include removing the capping system and allowing the probe molecule to move freely with the activated nanoimpeller, and either collecting the spectra in a shorter amount of time or continuously removing the solvent containing the released molecules, in order to avoid observation of the fluorescence of probe molecules not confined in the mesopores.

5.5.2 Rigidochromism Studies

The emission maxima of RuBPy shifts to lower wavelength when going from a pure solution to within the silica mesopores. This shift reveals that the RuBPy are in a more rigid environment in the mesopores, which is as expected. There is also a slight difference between nanoparticles with and without nanoimpeller functionalization, but as these are differently synthesized particles, the size of the pores and the interaction of the RuBPy probe molecules with the pore walls and solvents are not directly comparable.

The rigidochromic results of interest are the effects the 403 nm pump creates. For pure solution and RuBPy confined in silica nanoparticles without azobenzenes, the presence of 403 nm has no effect in the emission maxima. This is to be expected, as without azobenzene nanoimpellers, there is no additional motion and 403 nm pump should not change the solvent environment rigidity. For RuBPy contained in nanoimpeller functionalized particles, the emission maximum shifts to lower wavelength when 403 nm pump activates the nanoimpellers. The rigidochromism results indicate that the solvent matrix becomes more rigid when the nanoimpellers are photoexcited, contrary to expectations. This result could be explained by the change in the dipole moment of the azobenzene unit. In its trans state, the symmetry results in no overall dipole moment, but in its cis configuration, the molecule is considerably more polar. Therefore, when the 403 nm pump shifts the population toward more cis isomers, there is an increase in the polarity of the probe molecule's environment. Because the nanoimpellers are tethered to the silica wall, they are likely to be too rigid to reorient according to the excited state dipole moment, and may thus be increasing the energy level of the excited state, causing a shift to higher energy in the emission. Further experiments are required to confirm this proposed explanation, including

activating the cis-trans isomerization in the UV so that we acquire a photostationary state of mostly cis configuration, and monitor the emission spectrum under this environment.

5.6 SUMMARY

In this study, we have investigated the microenvironment inside mesoporous silica nanoparticles, and how the microenvironment may be affected by the presence of azobenzene nanoimpellers and their wagging motion when cis-trans isomerization is activated. Spectroscopic techniques used include time-dependent fluorescence anisotropy studies which monitor the decay lifetime of the fluorescence anisotropy, which monitors the tumbling rate and mobility of the probe molecule, and rigidochromic studies which reveal the rigidity of the solvent matrix and surrounding environment. Probe molecules were confirmed to be confined within the mesopores with the use of a pH activated valve and cap system and multiple washings, removing the possibility of interference by fluorescence from molecules adsorbed on the outside surface. Results show that activating the nanoimpellers increases the rotational correlation lifetime, indicating a decrease in mobility, possibly due to a higher concentration of probe molecules as the nanoimpellers build up molecules in certain regions of the pores. However, further studies are required to confirm this explanation.

5.7 REFERENCES

(1) Tarn, D.; Xue, M.; Zink, J. I. *Inorg. Chem.* **2013**, *52*, 2044.

(2) Angelos, S.; Yang, Y.-W.; Patel, K.; Stoddart, J. F.; Zink, J. I. *Angew. Chem. Int. Ed.* **2008**, *47*, 2222.

(3) Angelos, S.; Choi, E.; Vogtle, F.; De Cola, L.; Zink, J. I. *J. Phys. Chem. C* **2007**, *111*, 6589.

(4) Hernandez, R.; Tseng, H.-R.; Wong, J. W.; Stoddart, J. F.; Zink, J. I. *J. Am. Chem. Soc.* **2004**, *126*, 3370.

(5) Nguyen, T. D.; Liu, Y.; Saha, S.; Leung, K. C.-F.; Stoddart, J. F.; Zink, J. I. *J. Am. Chem. Soc.* **2007**, *129*, 626.

(6) Dunn, B.; Zink, J. I. *Chem. Mater.* **1997**, *9*, 2280.

(7) Xue, M.; Zink, J. I. *J. Phys. Chem. Lett.* **2014**, *5*, 839.

(8) Choi, E.; Lu, J.; Tamanoi, F.; Zink, J. I. *A. Anorg. Allg. Chem.* **2014**, *640*, 588.

(9) Lu, J.; Choi, E.; Tamanoi, F.; Zink, J. I. *Small* **2008**, *4*, 421.

(10) Sierocki, P.; Maas, H.; Dragut, P.; Richardt, G.; Vogtle, F.; De Cola, L.; Brouwer, F. A. M.; Zink, J. I. *J. Phys. Chem. B* **2006**, *110*, 24390.

(11) Du, L.; Liao, S.; Khatib, H. A.; Stoddart, J. F.; Zink, J. I. *J. Am. Chem. Soc.* **2009**, *131*, 15136.

(12) Szabo, A. *J. Chem. Phys.* **1984**, *81*, 150.

(13) Frauchiger, L.; Shirota, H.; Uhrich, K. E.; Castner, E. W. *J. Phys. Chem. B* **2002**, *106*, 7463.

(14) Valeur, B. *Molecular Fluorescence: Principles and Applications*; Wiley-VCH, 2001.

(15) Lakowicz, J. R. *Principles of Fluorescence Spectroscopy*; Springer, 2006.

(16) McKiernan, J.; Pouxviel, J.-C.; Dunn, B.; Zink, J. I. *J. Phys. Chem.* **1989**, *93*, 2129.

(17) Itokazu, M. K.; Polo, A. S.; Iha, N. Y. M. *J. Photochem. Photobio. A Chem.* **2003**, *160*, 27.

(18) Rivera, E. J.; Barbosa, C.; Torres, R.; Rivera, H.; Fachini, E. R.; Green, T. W.; Connick, W. B.; Colon, J. L. *Inorg. Chem.* **2012**, *51*, 2777.

(19) Innocenzi, P.; Kozuka, H.; Yoko, T. *J. Phys. Chem. B* **1997**, *101*, 2285.

(20) Terpetschnig, E.; Szmacinski, H.; Malak, H.; Lakowicz, J. R. *Biophys. J.* **1995**, *68*, 342.